FFI RAPPORT

THEORETICAL AND EXPERIMENTAL INVESTIGATION OF STRAIN GRADIENTS FOR TRANSVERSAL SHEAR STRESS DETERMINATION IN GRP SANDWICH PANELS

HAUGLAND Svein Jarle

FFI/RAPPORT-2001/02156

FFIE/793/116

Approved
Kjeller 18 April 2001

Stian Løvold
Director of Research

THEORETICAL AND EXPERIMENTAL INVESTIGATION OF STRAIN GRADIENTS FOR TRANSVERSAL SHEAR STRESS DETERMINATION IN GRP SANDWICH PANELS

HAUGLAND Svein Jarle

FFI/RAPPORT-2001/02156

FORSVARETS FORSKNINGSINSTITUTT
Norwegian Defence Research Establishment
P O Box 25, NO-2027 Kjeller, Norway

FORSVARETS FORSKNINGSINSTITUTT (FFI)
Norwegian Defence Research Establishment

P O BOX 25
N0-2027 KJELLER, NORWAY

UNCLASSIFIED

SECURITY CLASSIFICATION OF THIS PAGE
(when data entered)

REPORT DOCUMENTATION PAGE

1) PUBL/REPORT NUMBER	2) SECURITY CLASSIFICATION	3) NUMBER OF PAGES
FFI/RAPPORT-2001/02156	UNCLASSIFIED	91
1a) PROJECT REFERENCE	2a) DECLASSIFICATION/DOWNGRADING SCHEDULE	
FFIE/793/116	-	

4) TITLE

THEORETICAL AND EXPERIMENTAL INVESTIGATION OF STRAIN GRADIENTS FOR TRANSVERSAL SHEAR STRESS DETERMINATION IN GRP SANDWICH PANELS

5) NAMES OF AUTHOR(S) IN FULL (surname first)

HAUGLAND Svein Jarle

6) DISTRIBUTION STATEMENT

Approved for public release. Distribution unlimited. (Offentlig tilgjengelig)

7) INDEXING TERMS

IN ENGLISH:	IN NORWEGIAN:
a) strain sensor	a) tøyningssensor
b) fibre reinforced composites	b) fiberforsterkede kompositter
c) sandwich plate	c) sandwich plate
d) strain gradients	d) tøyningsgradienter
e) shear stresses	e) skjærspenninger

THESAURUS REFERENCE:

8) ABSTRACT

This report describes a theoretical and experimental investigation for transversal shear stress determination in the core of a sandwich panel. The outlined method is based on strain gradient measurements on the surface of the faces. The method is applicable both to isotropic and anisotropic sandwich plates. Experiments have been carried out on a fully clamped, rectangular plate with a concentrated load in centre. Strain gauges have been cemented at areas where one expects the highest shear stresses to occur, ie two points located near the clamping. Two tests have been carried out, one with load 5000 N and one with load 10000 N. Gradients have been measured in both x-, y- and 45 degree direction, but it is shown that it is only necessary to measure the steepest gradient to obtain acceptable values. This, together with exploitation of symmetry, simplifies the instrumentation of the plate. Measured strains and calculated shear stresses are compared to corresponding values from a finite element model of the same plate problem. The values match quite well, but it is difficult to measure the steepest gradients. The analytical stress values are in general somewhat higher than the simulated values, but this can be caused by weaknesses in the finite element model. For future measurements optical Bragg gratings will be used and not strain gauges as in this report. This as an attempt to measure the steepest gradients more accurate. Optical Bragg gratings are also the foundation of the existing CHESS project at FFI

9) DATE	AUTHORIZED BY	POSITION
	This page only	
18 April 2001	Stian Løvold	Director of Research

ISBN-82-464-0509-8

UNCLASSIFIED

SECURITY CLASSIFICATION OF THIS PAGE
(when data entered)

CONTENTS

		Page
1	INTRODUCTION	7
2	SHEAR STRESS DISTRIBUTION FROM STRAIN GRADIENTS	8
2.1	Introduction	8
2.2	Assumptions	8
2.3	Sandwich beam	11
2.3.1	Rectangular cross section	12
2.4	Quasiisotropic sandwich plate	13
2.5	Anisotropic sandwich plate	16
2.6	Delamination and core fracture	17
2.7	Strain gradients	19
3	MEASUREMENT TECHNIQUES	20
3.1	Strain gauges	20
3.1.1	The Quarter Bridge	22
3.2	Fibre optic Bragg gratings	23
3.2.1	Strain sensor system with interferometric interrogation	23
3.2.2	Strain sensor system with scanning Fabry-Perot filter interrogation	24
4	SANDWICH PLATE GEOMETRY AND MECHANICAL PROPERTIES	24
4.1	Physical dimensions of the plate. Clamping	24
4.2	Laminate and core data for the test plate	26
5	SIMULATIONS AND EXPERIMENTS	26
5.1	Load case and Finite Element Model (FEM)	26
5.2	Instrumentation	28
5.2.1	Advantage of symmetry	28
5.3	Distances between measurement points for the strain gradient calculation	29
5.4	Quasi-static experiments	33
5.5	Dynamic experiments	39
5.6	Discussion of experiments	44
5.6.1	Quasi-static tests	44
5.6.2	Dynamic tests	45
5.6.3	Calculation of shear strains	45
5.7	Comparison of measured and simulated strains	45
6	CALCULATION OF SHEAR STRESSES IN CORE	47
6.1	Calculation of transversal core shear stress from experimental results	47
6.1.1	Load 5000 N	47
6.1.1.1	Point 1	47
6.1.1.2	Point 2	48
6.1.2	Load 10000 N	49

6.1.2.1 Point 1 50
6.1.2.2 Point 2 50
6.2 Calculation of von Mises stresses in the core 50
6.3 Comparison with simulated core shear stresses 51
7 DISCUSSION, CONCLUSION AND FURTHER WORK 52
7.1 Discussion and comparison of shear stress values 52
7.2 Limitations 53
7.3 Conclusion and further work 54
References 57

APPENDIX

A LIST OF SYMBOLS 60
B MATERIAL PROPERTIES FOR THE SANDWICH PLATE 61
C CONTOUR PLOTS FROM FEM SIMULATIONS 62
D XY-PLOTS OF STRAINS AND SHEAR STRESSES ALONG THE PLATE AXES 65
D.1 Stress and strain for load 5000 N 66
D.1.1 Plots along the *y*-axis of the plate (Point 1) 66
D.1.2 Plots along the *x*-axis of the plate (Point 2) 72
D.2 Stress and strain for load 10000 N 78
D.2.1 Plots along the *y*-axis of the plate (Point 1) 78
D.2.2 Plots along the *x*-axis of the plate (Point 2) 84
Distribution list 90

THEORETICAL AND EXPERIMENTAL INVESTIGATION OF STRAIN GRADIENTS FOR TRANSVERSAL SHEAR STRESS DETERMINATION IN GRP SANDWICH PANELS

1 INTRODUCTION

The work in this thesis has been done as an extension of the development project *Composite Hull Embedded Sensor System* (CHESS), which is a collaboration between FFI and Naval Research Laboratory in Washington D.C. The CHESS project has developed a sensor system based on fibre optic Bragg gratings for real-time monitoring and analysis of the load on the hull of a high speed Surface Effect Ship (SES). The hull is made of glass fibre reinforced composite material with a so-called sandwich structure and was built for the Royal Norwegian Navy by Kvaerner Mandal, located in Mandal, Norway.

An important aspect of hull monitoring is to detect phenomena that can result in damage. It is well known that damage in the core material due to large shear stresses can cause delamination of the composite material and catastrophic failure of large sections of the hull. It is therefore important to determine the shear stresses in the core of a sandwich material. It is difficult to measure these parameters directly. The shear stresses are however, as we will see later, closely related to the strain gradients at the surface. One can in principle calculate the shear stresses based on measurements of strain gradients. It would therefore be of great interest to include this technique in the hull monitoring system that is being developed in the CHESS project.

This thesis is a continuation of the work done by the author in the report (1). This work represents a thorough investigation of mechanical aspects of composite materials and serves as a theoretical background for the work to follow in this thesis. The two reports can be read separately, but they may very well be read together. The most important parts from (1), which are the foundation for the work to follow, will be included in this report. However for the complete theoretical background the reader is referred to (1). Furthermore, for the reader who is not so familiar with composite mechanics, (1) will serve as an introduction to the field.

The thesis (1) together with this thesis can be regarded as a step further from the work done in (3) and (11). In those works strain gradients were measured on a sandwich beam, having a strain gradient only along the beam axis. Now the problem is extended to a plate problem, with strain gradients in several directions. A plate will be the most typical construction element where the strain gradient measurement technique will be used in real life.

Chapter 2 is an extract from the most relevant content in (1). The mechanical background for the experimental strain gradient method is presented. Both a beam and a plate are considered. All mechanical expressions used in the later experiments are presented here. The thesis (1) only considers an isotropic sandwich plate. As we shall see later the plate we are going to use is not

fully isotropic. The strain gradient technique from (1) will therefore in chapter 2 be extended to anisotropic sandwich plates.

Chapter 3 presents the measurement techniques, which will be used in the experiments. To measure the strain gradients both strain gauges and fibre optic Bragg gratings can be used. In this work strain gauges have been used. Strain gauge measurement is a cheap and established technique and serves well for measurements in the laboratory. But in measurements outside the laboratory where problems with noise are much more dominating, we have to use fibre optic Bragg gratings. Another advantage of Bragg gratings is the lower noise floor compared to strain gauges. Therefore both techniques will be outlined in this chapter. The thesis is written from a mechanical point of view, so to speak. The emphasis of this report will therefore not be to explain all the details in the measurement and the rather advanced equipment. A short presentation will be given. The interested reader is referred to (3), for instance, and the references given in that report. This report serves mainly as a first investigation of the suitability of the method when it comes to practical measurements. One of the goals is to find out how many strain sensors (gauges or gratings) that are actually needed. When this is known, one can for future measurements use Bragg gratings.

The geometry, lay-up, mechanical properties and clamping of the sandwich plate are presented in Chapter 4. Chapter 5 contains the performed FEM-simulations and experiments, both static and dynamic. Furthermore the strain results from simulations and experiments are compared here. Chapter 6 contains the shear stresses in the core calculated from the strain gradient measurements. The calculated shear stresses are also compared to values from the FEM-model. In Chapter 7 the results are discussed and conclusions are drawn. Suggestions for further work are also given.

2 SHEAR STRESS DISTRIBUTION FROM STRAIN GRADIENTS

2.1 Introduction

This chapter contains the technique developed in (1) giving the connection between strain gradients on the surface and shear stresses within the material. It is these results from (1) which are the foundation of the work to follow. The technique will be shown both for a sandwich beam and a sandwich plate, but experiments will only be performed on the plate problem. As mentioned in Chapter 1 we have extended our method developed in (1) to also apply to anistropic sandwich plates.

2.2 Assumptions

The theory is based on Whitneys shear deformation theory. When considering a sandwich plate we have to make some assumptions due to this shear deformation theory. The theory is well described in (1) (page 27), but will be summarised here. Bellow is a numbered list with assumptions in Whitneys shear deformation theory.

1. The core material is much thicker than the two faces.

2. The stresses in the plane of the core, σ_1, σ_2 and σ_6, can be ignored.
3. The displacements u^c and v^c in the core are linear functions of z.
4. The faces are made of a given number of plies of orthotropic materials bound together. The orthotropic axes in the individual plies do not have to coincide with the global x- and y-axes for the plate.
5. The displacements u and v are uniform trough the thickness of the skins.
6. The transversal shear stresses σ_4 and σ_5 can be ignored in the faces.
7. The plate displacements are small compared to the plate thickness.
8. The strains in the plane, ε_1, ε_2 and ε_6 are small.
9. The displacement w is independent of the z coordinate. As usual in plate theory σ_3 and ε_3 are neglected.
10. Core and faces obey Hookes law.
11. Core and faces have constant thickness.
12. Temperature effects are ignored assuming that the plate and environment have equal and constant temperature.

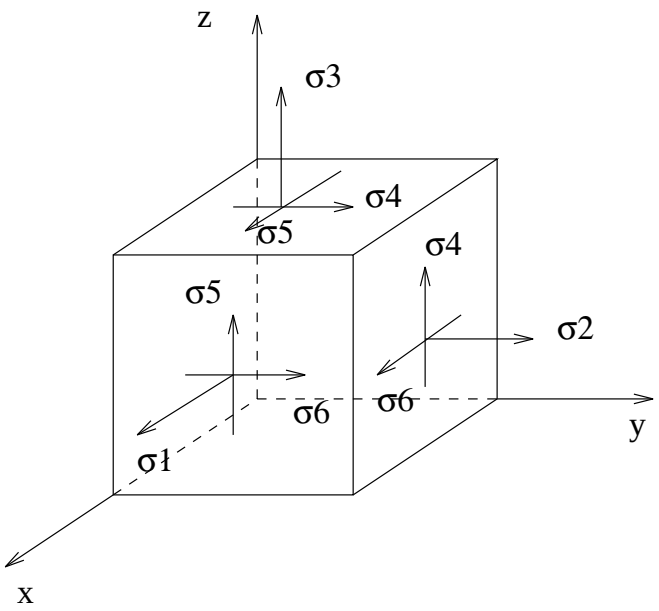

Figure 2.1 Stress components in a plate element.

Figure 2.1 shows all the stress components that act on an infinite small plate element. The strain components have identical directions. Look into the above list to see what components may vanish in faces and core.

Some of the assumptions in the list are self-explaining, or the result is obvious. Assumptions 2 and 6 however deserve some explanation, and a comment on what consequences they have for the stress distribution through the cross section of the sandwich plate. In figure 2.2 and 2.3 the normal stress distribution and shear stress distribution, respectively, are given across the cross section. Both the approximate and exact distributions are given. As we can see from the figures, the faces take all the normal stresses and the core takes the shear stresses. Because the faces are thin compared to the core, they can be regarded as membranes. From this follows the constant

normal stress distribution across the thickness. In the real case for the shear stress distribution the distribution is as it is because the shear stresses on the surface have to be zero, and we have breakpoints at the interface between faces and core.

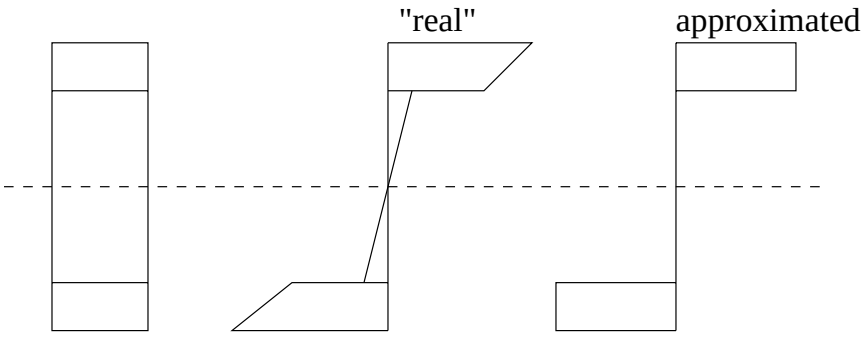

Figure 2.2 Normal stress distribution in a sandwich plate.

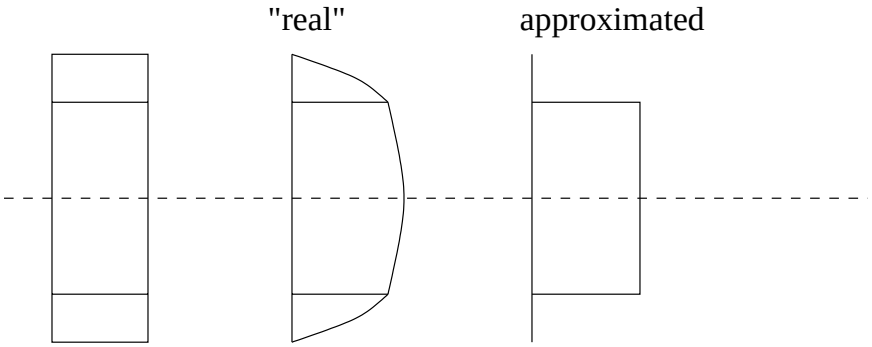

Figure 2.3 Shear stress distribution in a sandwich plate.

As in (1), simplified notation is used also here. The following statements are therefore valid, with reference to figure 2.1:

$$\sigma_1 = \sigma_x, \sigma_2 = \sigma_y, \sigma_3 = \sigma_z \tag{2.1}$$

$$\tau_4 = \sigma_4 = \tau_{yz}, \tau_5 = \sigma_5 = \tau_{xz}, \tau_6 = \sigma_6 = \tau_{xy} \tag{2.2}$$

$$\varepsilon_1 = \varepsilon_x, \varepsilon_2 = \varepsilon_y, \varepsilon_3 = \varepsilon_z, \tag{2.3}$$

$$2\varepsilon_4 = 2\varepsilon_{yz} = \gamma_{yz}, 2\varepsilon_5 = 2\varepsilon_{xz} = \gamma_{xz}, 2\varepsilon_6 = 2\varepsilon_{xy} = \gamma_{xy} \tag{2.4}$$

All of these forms will be used in this report.

2.3 Sandwich beam

The theory for sandwich beams are (as for classical beams) based on the Bernoulli deformation hypothesis [1] and the assumption that normal stresses on planes parallel to the beam can be neglected. The faces must be thin compared to the core thickness. The core is isotropic and linear elastic. The faces are assumed to be transversal isotropic, which means that isotropic theory can be used. No shear coupling in the plane would then appear, and Hookes law for isotropic materials can be used. To simplify the expressions, all dimensions are assumed to be constant along the beam length, see the geometry in figure 2.4. Both faces of the beam have equal thickness.

The bending stresses in the faces are given by

$$\sigma_f = \frac{E_f M(x)}{D} y \tag{2.5}$$

D is the flexural rigidity of a beam. D represents in our case the flexural rigidity of the cross sections of the faces and core measured around the z-axis (see figure 2.4). For a rectangular cross section, as in our case, D becomes

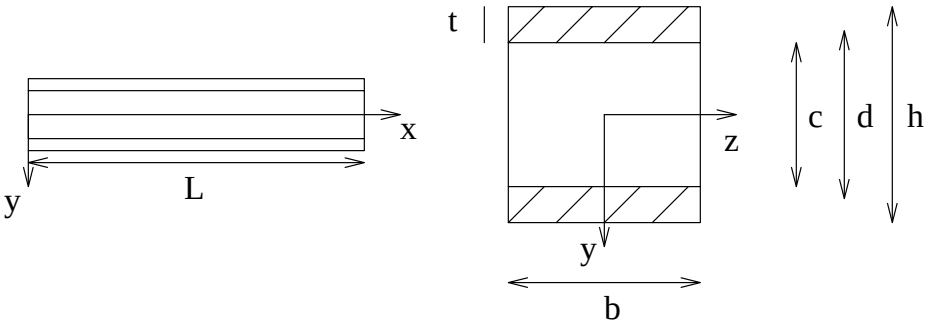

Figure 2.4. Dimensions for the sandwich beam.

$$D = \sum_{i=f,c} E_i I_i = E_f \frac{bt^3}{6} + E_f \frac{btd^2}{2} + E_c \frac{bc^3}{12} \tag{2.6}$$

E_f and E_c are the elasticity modulus (Young's modulus) for faces and core, respectively. I is the second moment of area. The value of E_f is dependent on the plies in the laminates, and the expression is

$$E_f = 2 \cdot \frac{4}{t^3} \sum_{i=1}^{n} E_{fi} (z_i - z_{i-1})^3 \tag{2.7}$$

[1] Cross sections perpendicular to the beam axis remain perpendicular after deformation.

z_i is the distance from the centre of the laminate, $z_0=0$, to the i'th lamina. (z_i-z_{i-1}) is thereby the thickness of each ply (lamina) in the laminate. t is the thickness of each face.

The connection between the strain on the surface along the beam length and the bending moment in a given position is obtained by setting $y=\pm h/2$ and introducing Hookes law $\sigma_f=E_f\varepsilon_f$ in equation 2.5:

$$M(x)=\frac{2D}{E_f h}E_f\varepsilon_f=\frac{2D}{h}\varepsilon_f \tag{2.8}$$

The connection between moment and shear force is given by:

$$V(x)=\frac{dM(x)}{dx} \tag{2.9}$$

From classical beam theory we get the connection between transversal shear and the shear force, and modified for a sandwich beam we have:

$$\tau_{xy}=\frac{V(x)}{Db}\sum_{i=f,c}S_iE_i \tag{2.10}$$

S_i is the first moment of area for each of the plies. D is the flexural rigidity for the whole cross section. By using the equations (2.8)-(2.10) the connection between strain gradients on the surface and the shear stress in the core can be established:

$$\tau_{xy}=\frac{2\sum_{i=f,c}S_iE_i}{hb}\frac{d\varepsilon_{fx}}{dx} \tag{2.11}$$

2.3.1 Rectangular cross section

For a rectangular cross section we get

$$\sum_{i=f,c}S_iE_i=b\left[\frac{E_f td}{2}+\frac{E_c}{2}\left(\frac{c^2}{4}-y^2\right)\right] \tag{2.12}$$

Equation (2.11) in the rectangular case becomes

$$\tau_{\mathrm{xy}}=\frac{2\left[\frac{E_f td}{2}+\frac{E_c}{2}\left(\frac{c^2}{4}-y^2\right)\right]}{h}\frac{d\varepsilon_{fx}}{dx} \tag{2.13}$$

which gives a parabolic distribution across the cross section. The maximum shear stress value is obtained by setting $y=0$ in the above expression:

$$\tau_{xy,max} = \frac{2\left[E_f \frac{td}{h} + E_c \frac{c^2}{4h}\right]}{h} \frac{d\varepsilon_{fx}}{dx} \tag{2.14}$$

The equation is only applicable for small deflections.

As shown in figure 2.3 it is assumed that the core alone takes all the shear stresses and that these are constant across the cross section. Assuming constant shear stresses we can write

$$\tau_{xy} = \frac{V(x)}{A_c} \tag{2.15}$$

where A_c is the cross section area of the core. By using equation (2.8) and (2.9) we obtain

$$\tau_{xy} = \frac{2D}{hA_c} \frac{d\varepsilon_x}{dx} \tag{2.16}$$

2.4 Quasiisotropic sandwich plate

This section contains the method giving the connection between strains at the surface and shear stresses within the material for isotropic sandwich plates. In (1) different types of material symmetries are treated, and one of these are transversal isotropy. For a sandwich plate this means that in the faces there exists a plane where the mechanical properties are the same in all principal directions. The method developed in (1) and given below only applies to isotropic faces and not in general to anisotropic faces. The report (1) explains more about the conditions for anisotropic and isotropic sandwich plates. In the next section the method will be extended to anisotropic sandwich plates where we have to deal with different plate stiffnesses in all principal directions.

Considering an equilibrium condition the shear forces can be expressed as

$$Q_x = \frac{\partial M_x}{\partial x} + \frac{\partial M_{yx}}{\partial y} \tag{2.17}$$

$$Q_y = \frac{\partial M_y}{\partial y} + \frac{\partial M_{yx}}{\partial x} \tag{2.18}$$

The moments are

$$M_x = D_x\left(\frac{1}{r_x} + v\frac{1}{r_y}\right) \tag{2.19}$$

$$M_y = D_y\left(\frac{1}{r_y} + v\frac{1}{r_x}\right) \tag{2.20}$$

$$M_{xy} = M_{yx} = D_{xy}\frac{1}{r_{xy}} \tag{2.21}$$

where r_x etc are the radii of curvature and $1/r_x$ etc are the curvatures. D_x, D_y and D_{xy} are the plate stiffnesses in the *x-, y-* and shear direction and *v* is Poisson's ratio. The strains in the plate can be expressed by the radii of curvature and can generally be written as

$$\varepsilon_j = \frac{z}{r_j} \tag{2.22}$$

where *z* is the direction of thickness (transversal direction). The surface strain, where $z=h/2$, becomes

$$\varepsilon_x = \frac{h}{2r_x} \tag{2.23}$$

$$\varepsilon_y = \frac{h}{2r_y} \tag{2.24}$$

$$\frac{1}{2}\gamma_{xy} = \varepsilon_{xy} = \frac{h}{2r_{xy}} \tag{2.25}$$

By finding the curvatures expressed by the strains from equation (2.23)-(2.25), the moments can be expressed by the strains:

$$M_x = D_x\left(\frac{2\varepsilon_x}{h} + v\frac{2\varepsilon_y}{h}\right) \tag{2.26}$$

$$M_y = D_y\left(\frac{2\varepsilon_y}{h} + v\frac{2\varepsilon_x}{h}\right) \tag{2.27}$$

$$M_{xy} = -M_{yx} = D_{xy}\frac{\gamma_{xy}}{h} \tag{2.28}$$

For an isotropic sandwich plate we have $D_x=D_y\neq D_{xy}$. The moment expressions are derived and inserted into equation (2.17) and (2.18) and we finally obtain:

$$Q_x = \frac{2}{h}\left[D_x \left[\frac{\partial \varepsilon_x}{\partial x} + v_f \frac{\partial \varepsilon_y}{\partial x} \right] - D_{xy} \frac{\partial \gamma_{xy}}{\partial y} \right] \tag{2.29}$$

$$Q_y = \frac{2}{h}\left[D_y \left[\frac{\partial \varepsilon_y}{\partial y} + v_f \frac{\partial \varepsilon_x}{\partial y} \right] - D_{xy} \frac{\partial \gamma_{xy}}{\partial x} \right] \tag{2.30}$$

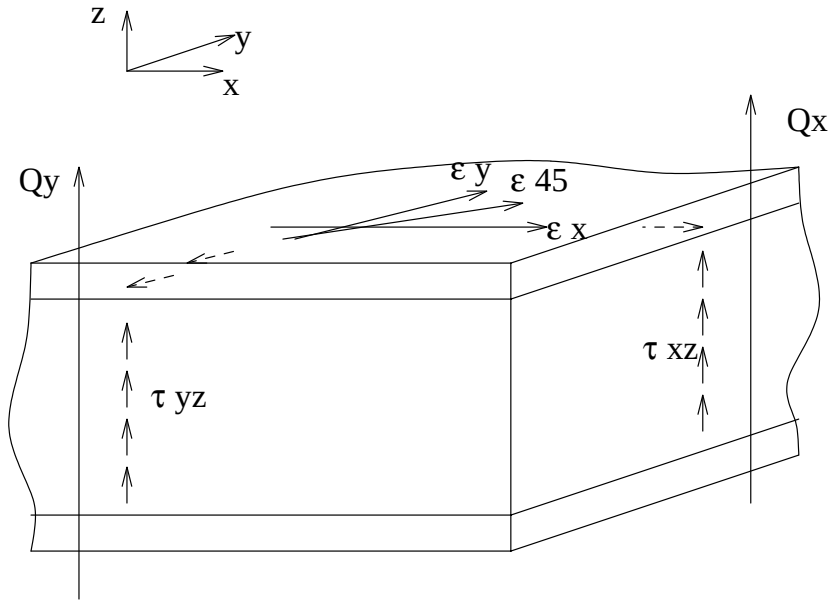

Figure 2.5 Strains, shear stresses and –forces in the sandwich plate.

The expressions for the plate stiffnesses are taken from (1). We have:

$$D_x = D_y = \frac{E\ h^3}{12(1-v^2)} - \frac{E\ c^3}{12(1-v^2)} + \frac{E\ c^3}{12(1-v^2)} \tag{2.31}$$

$$D_{xy} = \frac{E\ h^3}{48(1+v\ )} - \frac{E\ c^3}{48(1+v\ )} + \frac{E\ c^3}{48(1+v\ )} \tag{2.32}$$

Here E_f and v_f are Young's modulus and Poisson's ratio, respectively, for the faces and E_c and v_c are the corresponding values for the core. h is the total plate thickness, while c is the core thickness. As mentioned before we assume constant shear stress across the core thickness. The shear stresses are then given by

$$\tau_{xz} = \frac{Q_x}{c} \tag{2.33}$$

$$\tau_{yz} = \frac{Q_y}{c} \tag{2.34}$$

Q_x and Q_y are the shear forces from eq. (2.29) and (2.30), c is the core thickness, assuming that only the core feels the shear forces. Figure 2.5 shows how strains, shear forces and –stresses appear in the structure.

The stresses in the plane, σ_x, σ_y and τ_{xy}, are neglected in the core, see assumption 2 section 2.2. The values of σ_x and σ_y in the faces are obtained from Hookes law by use of equation (2.23) and (2.24), and we get

$$\sigma_x = \frac{E\ z}{1-\nu^2}\left(\frac{1}{r_x} + \nu\ \ \frac{1}{r}\right) = \frac{E}{1-\nu^2}\left(\frac{2\varepsilon_x}{h} + \nu\ \ \frac{2\varepsilon}{h}\right) \tag{2.35}$$

$$\sigma\ \ = \frac{E\ z}{1-\nu^2}\left(\frac{1}{r} + \nu\ \ \frac{1}{r_x}\right) = \frac{E}{1-\nu^2}\left(\frac{2\varepsilon}{h} + \nu\ \ \frac{2\varepsilon_x}{h}\right) \tag{2.36}$$

2.5 Anisotropic sandwich plate

We will now extend the method outlined in (1) and in section 2.4 to include anisotropic sandwich plates. As we shall see later, the plate used in experiments has an anisotropic lay-up. The method from (1) is therefore incomplete to use for this plate. As in (1) the underlying theory is taken from (2) and (10).

From an equilibrium consideration we get the shear forces expressed in the same way as for isotropic sandwich plates, equation (2.17) and (2.18). For *thin* laminates we can approximate the moments to:

$$M_x = D_x \frac{1}{r_x} + \nu_{xy} D_y \frac{1}{r_y} \tag{2.37}$$

$$M_y = D_y \frac{1}{r_y} + \nu_{yx} D_x \frac{1}{r_x} \tag{2.38}$$

$$M_{xy} = -M_{yx} = D_{xy} \frac{1}{r_{xy}} \tag{2.39}$$

We observe that we now have different plate stiffnesses and Poisson's ratios in the principal directions (x and y). Furthermore, the same relation between radii of curvature and strains is still valid, equation (2.22). We substitute equation (2.23)-(2.25) into the moment expressions above to obtain the moments expressed by the strains. Finally we insert these moments into the equations for the shear forces and obtain for anisotropic plates:

$$Q_x = \frac{2}{h}\left[D_x \frac{\partial \varepsilon_x}{\partial x} + \nu_{fxy} D_y \frac{\partial \varepsilon_y}{\partial x} - D_{xy} \frac{\partial \gamma_{xy}}{\partial y} \right] \tag{2.40}$$

$$Q_y = \frac{2}{h}\left[D_y \frac{\partial \varepsilon_y}{\partial y} + \nu_{fyx} D_x \frac{\partial \varepsilon_x}{\partial y} - D_{xy} \frac{\partial \gamma_{xy}}{\partial x} \right] \tag{2.41}$$

The new plate stiffnesses can be found by modifying the expressions for the isotropic plate stiffnesses. We remember that we now have different Young's moduli and Poisson's ratios in the *x*- and *y*-directions. Moreover, we have to use the shear modulus, G_{xy}, in the expression for D_{xy}, because there is no simple relation between the elasticity modulus, the shear modulus and Poisson's ratio for anisotropic materials. The expressions for the anisotropic plate stiffnesses becomes:

$$D_x = \frac{E_x h^3}{12(1-\nu_x^2)} - \frac{E_x c^3}{12(1-\nu_x^2)} + \frac{E_c c^3}{12(1-\nu_c^2)} \tag{2.42}$$

$$D = \frac{E h^3}{12(1-\nu_x^2)} - \frac{E c^3}{12(1-\nu_x^2)} + \frac{E_c c^3}{12(1-\nu_c^2)} \tag{2.43}$$

$$D_{xy} = \frac{G_{xy} h^3}{24} - \frac{G_{xy} c^3}{24} + \frac{E_c c^3}{48(1+\nu_c)} \tag{2.44}$$

The equations in section 2.4 for the shear stresses, eq. (2.33) and (2.34), are of course still valid.

2.6 Delamination and core fracture

It is natural to assume that when we want to prevent delamination and core fracture, we must in a way combine the two shear stresses found from equation (2.33) and (2.34). Since the core material is an isotropic material we can use the von Mises failure criterion to add the shear components. We then obtain the effective shear stress. Delamination occurs when the effective shear stress in the plane between face and core reaches a critical value. Core fracture occurs when the effective shear stress in the core material reaches a critical value.
The general von Mises failure criterion is taken from (12) and is given as

$$\sigma_j = \sqrt{\frac{1}{2}\left[(\sigma_x - \sigma_y)^2 + (\sigma_y - \sigma_z)^2 + (\sigma_z - \sigma_x)^2\right] + 3\tau_{xy}^2 + 3\tau_{yz}^2 + 3\tau_{zx}^2} \tag{2.45}$$

where σ_j is called effective stress, equivalent stress or von Mises stress. The other symbols are defined in figure 2.1. According to the list in section 2.2 all stress components except τ_{xz} and τ_{yz} vanish in the core. In our case (the core material) equation (2.45) then becomes

Delamination:

$$\sigma_j = \tau = \sqrt{3(\tau_{xz}^2 + \tau_{yz}^2)} \geq \tau_{delam.} \tag{2.46}$$

Core fracture:

$$\sigma_j = \tau = \sqrt{3(\tau_{xz}^2 + \tau_{yz}^2)} \geq \tau_{core,max} \tag{2.47}$$

Figure 2.6 shows how the stresses appear in the core material when fracture begins to develop. As we see the shear fracture is actually a tensile fracture. The theory predicts the maximum shear stress 45° on the maximum tensile stress, see (9) or (12). The 45°'s fracture line is also what we see in fracture tests of sandwich panels with transversal loading. The report (15) is an excellent example of this. Figure 2.7 is taken from (15) and shows a sample where the fracture starts in the core and propagates to the face-core interface at 45° angle relative to the core plane. The further propagation does not seem to be delamination, but rather debonding at and near the face-core interface. The bonding of the face and core is generally stronger than the core. The most important fracture criterion for the sandwich panel is therefore (2.47). Allthough we do not have delamination in the strictest meaning of the word since the further fracture happens in (the top of) the core, the consequences over a larger area will be the same: We will get a face uncoupled from the core acting like a free membrane.

.

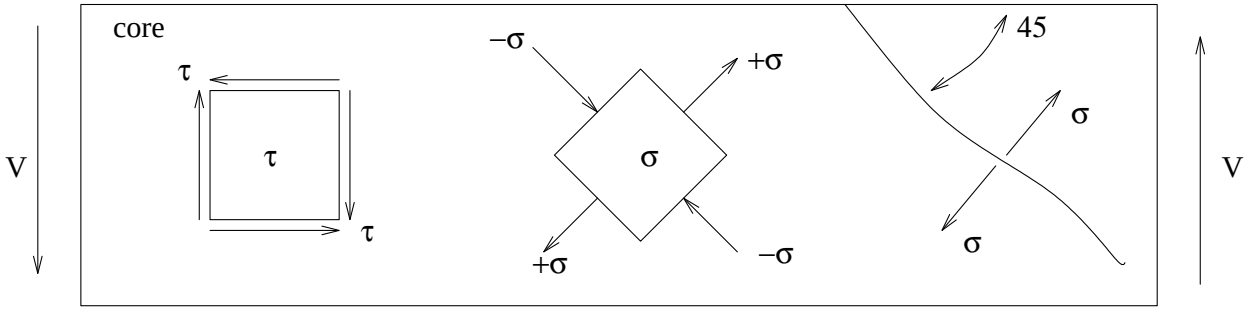

Figure 2.6. Model of shear fracture in the core.

Figure 2.7. Example of shear fracture in the core.

2.7 Strain gradients

The shear forces are now expressed by the strain gradients. It is these strain gradients that are measured by strain gauges or fibre optic Bragg gratings. The beam is the simplest case, because here we only have a gradient in one direction, the direction along the beam. The plate is more complicated, because we have strain gradients in three directions: *x-, y-* and shear direction. A gradient is measured with two gratings or gauges a little distance apart. In the beam case we only need one strain gauge in two points on the beam to get a shear stress value. The plate case however requires four points with three strain gauges in each point to get the shear stress values. This can be seen from the strain gradients in equation (2.29) and (2.30).
The strain gradients are generally obtained as:

$$\frac{\partial \varepsilon_x}{\partial x} = \frac{\varepsilon_{x2} - \varepsilon_{x1}}{\Delta x} \tag{2.48}$$

$$\frac{\partial \varepsilon_y}{\partial y} = \frac{\varepsilon_{y4} - \varepsilon_{y3}}{\Delta y} \tag{2.49}$$

$$\frac{\partial \varepsilon_y}{\partial x} = \frac{\varepsilon_{y2} - \varepsilon_{y1}}{\Delta x} \tag{2.50}$$

$$\frac{\partial \varepsilon_x}{\partial y} = \frac{\varepsilon_{x4} - \varepsilon_{x3}}{\Delta y} \tag{2.51}$$

$$\frac{\partial \gamma_y}{\partial x} = \frac{\gamma_{y\ 2} - \gamma_{y\ 1}}{\Delta x} \tag{2.52}$$

$$\frac{\partial \gamma_{xy}}{\partial y} = \frac{\gamma_{xy4} - \gamma_{xy3}}{\Delta y} \tag{2.53}$$

where index 1 and 2 indicate values when we go in *x*-direction and index 3 and 4 indicate values in *y*-direction.

As we will see later the problem will be further simplified when it comes to strain gradients when we take advantage of symmetries in our plate problem.

We cannot measure the shear strain γ_{xy} directly. The strain in a 45°'s angle to the *x*-axis is measured, and by help of an expression from strain analysis we can calculate γ_{xy} from the strains in the *x-*, *y-* and 45°'s directions. The expression is taken from (12) and given below.

$$\varepsilon(\varphi) = \frac{\varepsilon_x + \varepsilon_y}{2} + \frac{\varepsilon_x - \varepsilon_y}{2}\cos 2\varphi + \frac{1}{2}\gamma_{xy}\sin 2\varphi \tag{2.54}$$

φ is in our case 45°, resulting in $cos2\varphi = 0$ and $sin2\varphi = 1$. Ergo:

$$\varepsilon(45) = \frac{\varepsilon_x + \varepsilon_y}{2} + \frac{1}{2}\gamma_{xy} \tag{2.55}$$

Finally, solving for γ_{xy} we get:

$$\gamma_{xy} = 2\varepsilon(45) - \varepsilon_x - \varepsilon_y \tag{2.56}$$

3 MEASUREMENT TECHNIQUES

In this work strain gauges have been used to measure the strains at the surface of the plate. In the CHESS project fibre optic Bragg gratings are used to measure strain. Since the work to follow is done in the laboratory only, strain gauges have been chosen. Strain gauges are very sensitive to noise due to radiation from electrical equipment in the surroundings. This does not affect the optic gratings. Since we do not have the problem with heavy noise in the laboratory, the much cheaper strain gauges are chosen. Strain gauges have a higher measurement uncertainty than optical gratings have. However, when all forces and constraints are under control as they are here, and an estimate of the strain field already exists from a finite element model (explained later), the distances in the strain gradients can be chosen to reduce the uncertainty in the strain gauge measurement technique. It is however a fact that when the strain gradient becomes sufficient small, it cannot be detected by strain gauges. The same problem occurs when the gradient is very steep. Optical gratings have possibilities to measure smaller strain levels, and they can also be mounted much closer (on the same fibre) than strain gauges. Therefore, if the experimental method turns out to be successful, optical gratings will be used in future measurements.

Since the strain gradients can be measured in both of the above two techniques, the underlying theory of both will be briefly explained here. The interested reader is referred to (3) and (14), for instance, and the references given here for a more complete presentation.

3.1 Strain gauges

Measurements using strain gauges have developed to become a simple, usable and precise technique to measure both strain and vibrations. The main advantages are that the equipment is easy available and rather cheap. In addition, small amounts of education are needed. The technique is well established and accepted. Some disadvantages have already been mentioned: The strain gauges are sensitive to electric and magnetic fields, also, when measuring over large areas the amount of cables and equipment will be extensive.

The technique itself is based on the principle that a live cable will change its resistance when the length (or cross section) of the cable is changed. A strain gauge is a conductor with very small cross section cemented to the test object. The cross section of the strain gauge is changed when the object is loaded, ie strain is introduced. By use of the so-called Wheatstone bridge, see figure 3.1, we can increase the signal even from very small changes in resistance.

In the Wheatstone bridge the following important relation for the two “arms” is true:

$$\frac{R_1}{R_2} = \frac{R_4}{R_3} \tag{3.1}$$

In figure 3.1 the resistors can be regarded both as ordinary resistors or strain gauges. We have three different ways that the Wheatstone bridge can be used in: full bridge, half bridge or quarter bridge. The names full, half and quarter indicate that we have four, two or one active strain gauges in the circuit.

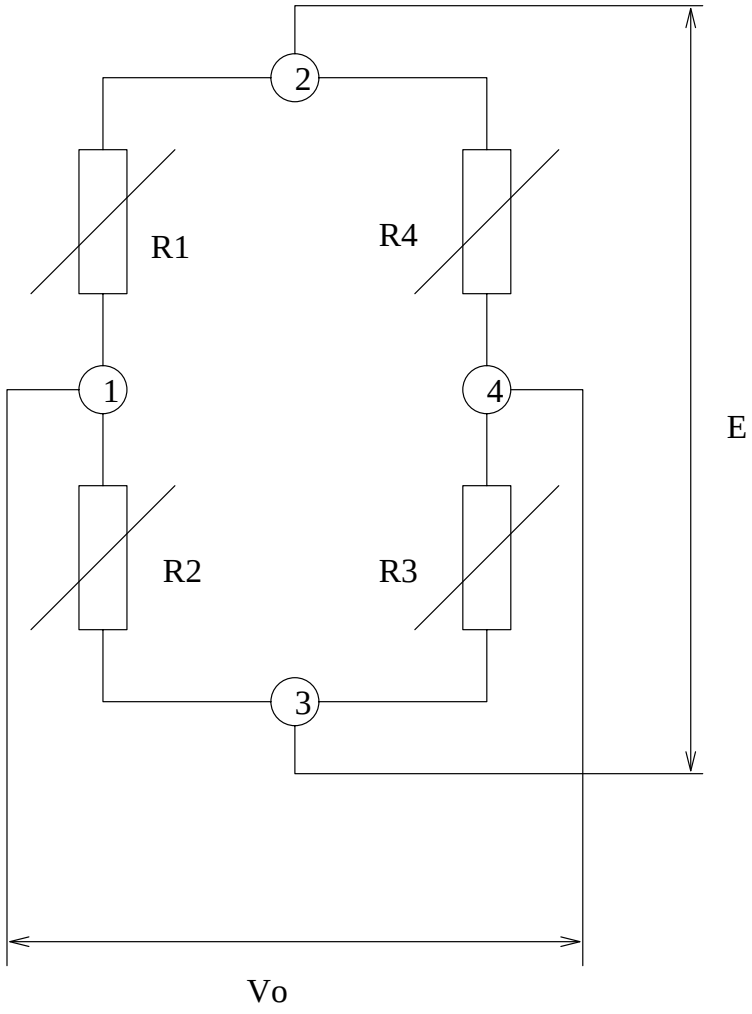

Figure 3.1. Representation of the Wheatstone bridge circuit.

The relation between strain and change in resistance is given by

$$\varepsilon = \frac{\partial R}{R}\frac{1}{k} \tag{3.2}$$

where R is resistance [Ω], ∂R is change in resistance and k is the gauge factor which is given by the manufacturer for each strain gauge. The relation between strain and the voltages E (excitation voltage) and V in the bridge is given by

$$\varepsilon = Const. \cdot \frac{V}{E} \tag{3.3}$$

The constant is dependent on what strain gauge (gauge factor) and bridge we choose.
To get a secure calibration and accurate tuning for practical measurements a special amplifier is used. In the amplifier it is possible to calibrate the output signal by giving the relation of voltage, V/E, a magnitude that is given for a known strain. This relation between V/E and strain is then used to calculate unknown strain levels from other output signals of V/E. When strain gauges are used to measure strain (gradients) on the surface, the amplifier converts the strain to electrical signals of varying voltage as output signals.

3.1.1 The Quarter Bridge

For the strain measurements in the experiments the bridge to use is the quarter bridge. Therefore this bridge will be briefly examined here. In the quarter bridge we only have one active strain gauge. Let R_1 in fig. 3.1 be the active strain gauge. When a change in resistance is introduced, the resistance becomes $R+\partial R$, while the other resistances remain unchanged (=R). For this configuration the measured voltage over the bridge becomes

$$V = \pm \frac{E \partial R}{4R} \tag{3.4}$$

By use of (3.2) and rearranging we get the relation between strain and voltage:

$$\varepsilon = \frac{4V}{Ek} \tag{3.5}$$

This important relationship shows that there is a direct connection between the applied strain and the voltage in the measuring link. If the excitation voltage E and the gauge factor k are known, it is only necessary to measure the out-of-balance voltage V to obtain the strain level.

When the strain levels become sufficiently small, temperature effects can play a great role in the overall strain value, i.e. the strain is not a result only of mechanical loading. This is compensated for in the Wheatstone bridge by insertion of a compensation resistor into one of the bridge arms. This resistor has a temperature characteristic calculated to compensate for the resistance change in the active gauge due to temperature variation. The simplest and most commonly employed method to obtain a compensation resistor with the desired characteristic, is to use a strain gauge with identical specification as the active gauge. The compensating gauge must be placed close to the active gauge, but not at the loaded object, so that it experiences the same temperature changes but not strain from mechanical loading.

For further details on strain gauge measurements, see (14).

3.2 Fibre optic Bragg gratings

The presentation here is based on (6) and (7). For further details see these reports. Two strain sensor systems will shortly be presented here: strain sensor system with interferometric interrogation and strain sensor system with scanning Fabry-Perot filter interrogation.

3.2.1 Strain sensor system with interferometric interrogation

The main principle in this technique is to convert a change in wavelength introduced by strain into a phase change. Light from a broadband source is sent trough an optic fibre with gratings inscribed in the fibre where we want to measure the strain. These gratings are cemented to the loaded object. Each grating is produced to have a unique wavelength. Light is reflected from each grating and sent through an interferometer in order to convert the wavelength changes induced by the strain into phase changes $\Delta\phi$ given by

$$\Delta\phi = -2\pi nd\frac{\Delta\lambda_b}{\lambda_b^2} = -2\pi nd\frac{1-p_e}{\lambda_b}\varepsilon \tag{3.6}$$

where n is the effective fibre index, d is the geometrical path imbalance, λ_b is the Bragg grating wavelength, $p_e = 0{,}22$ is the effective photoelastic constant and ε is the strain. Figure 3.2 gives an overview of the equipment needed for this technique. The channels from the interferometers are demultiplexed in the WDM filters, splitting the light into eight fibres, where each channel is detected and the phase retrived.

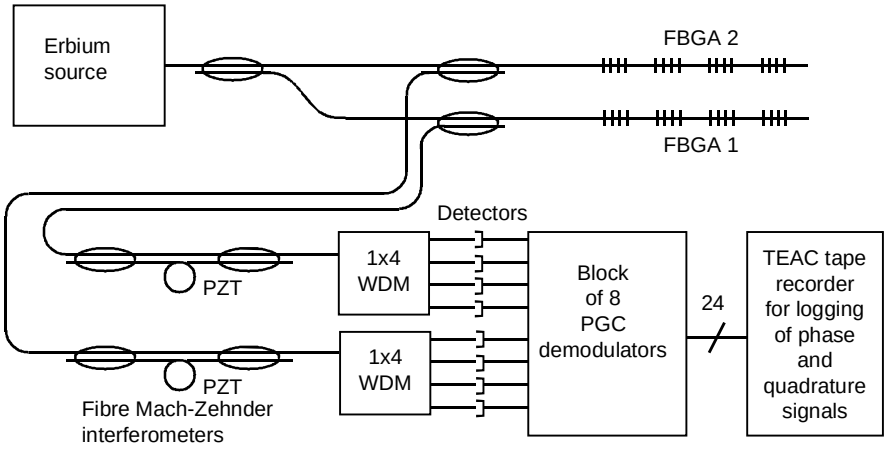

Figure 3.2. A Bragg grating sensor system with interferometric interrogation.

3.2.2 Strain sensor system with scanning Fabry-Perot filter interrogation

The second interrogation system is based on a scanning fibre optic Fabry-Perot filter. The configuration is shown in figure 3.3.

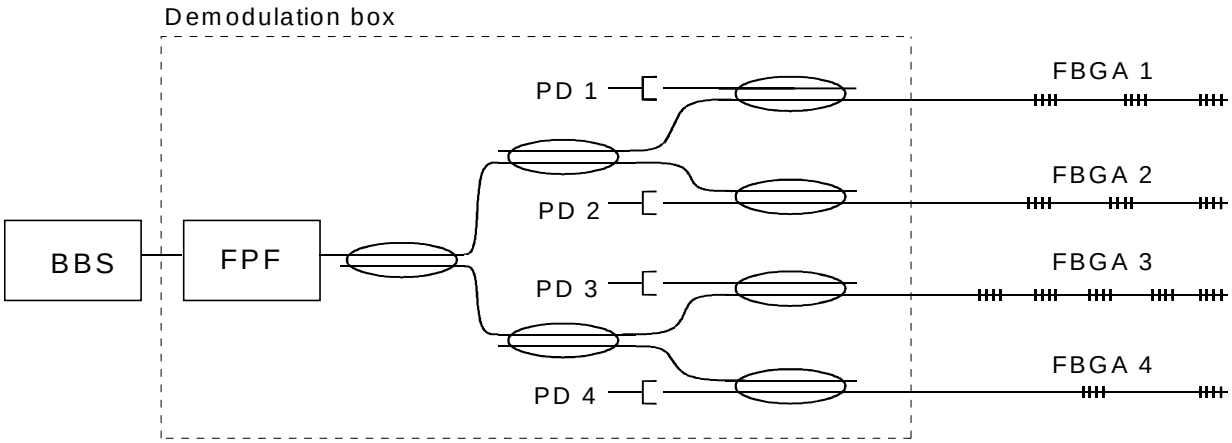

Figure 3.3. Optical configuration of the Fabry-Perot system.

The light source is an erbium broadband source (BBS). The input light is filtered by the Fabry-Perot filter (FPF) and sent to four Bragg grating arrays. (FBGA). The light returned from each array is detected at a separate photodiode (PD). The passband of the Fabry-Perot filter is scanned through the wavelengths of interest, and a peak is detected every time a grating reflection wavelength coincides with the passband. In addition to the optical components, the system consists of analogue electronics for detection and amplification of the light. The system also contains digital electronics for generation of signals for the Fabry-Perot filter, and for communication with a PC where strain values are calculated.

4 SANDWICH PLATE GEOMETRY AND MECHANICAL PROPERTIES

4.1 Physical dimensions of the plate. Clamping

The composite sandwich plate used in the tests in this report is the same plate used in the former drop experiments done by the CHESS project team at FFI and collaborators at NTNU and MARINTEK. The plate is fabricated by FiReCo a.s. Dimensions are as follows:

- Length, *a*: *1000 mm*
- Width, *b*: *600 mm*
- Core thickness, *c*: *25 mm*
- Plate thickness, *h*: *29 mm*
- Laminate thickness, *t*: *2 mm*

The core material is Divinycell H 200 and the laminates are built up by several layers of Glass Reinforced Polyester (GRP).

Figure 4.1. Dimensions in transversal direction

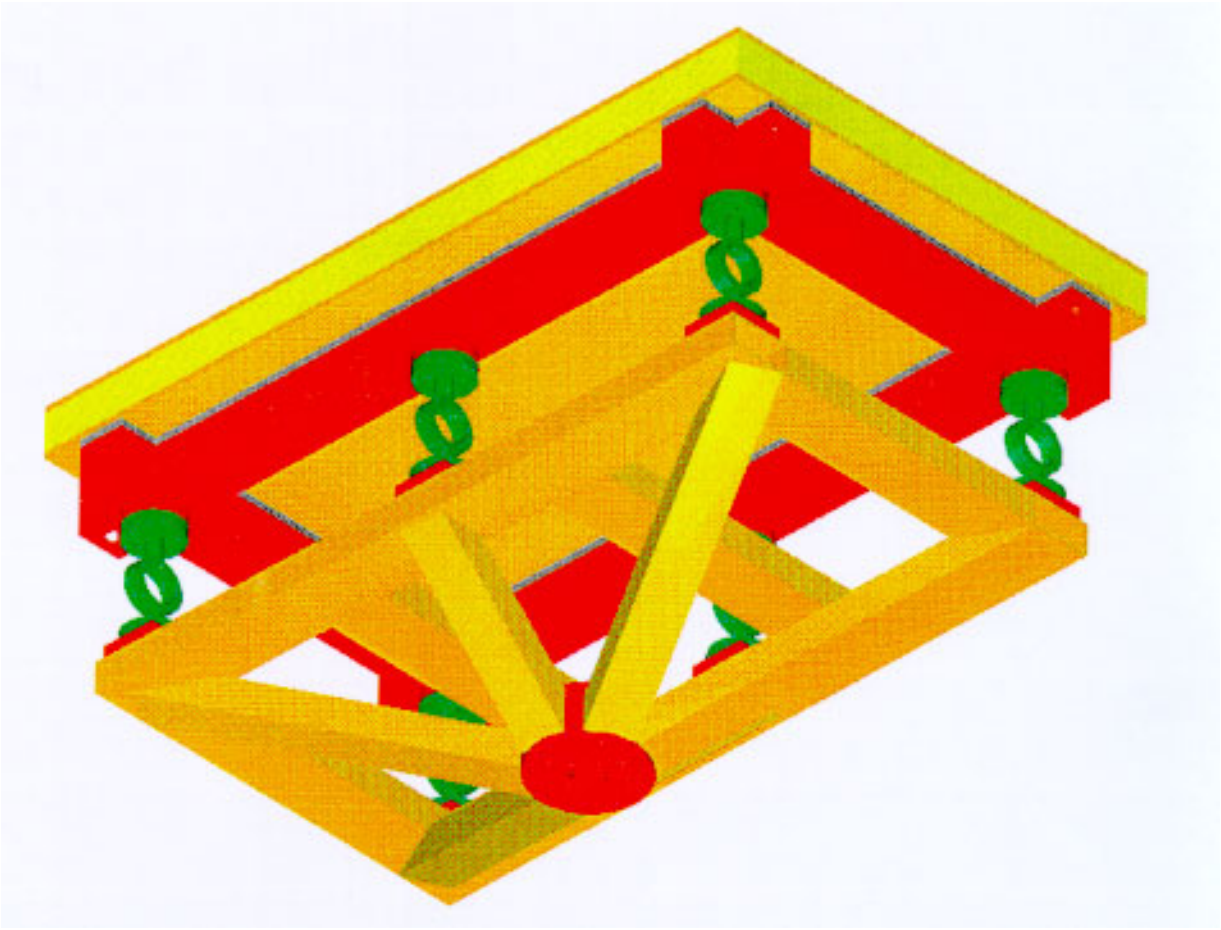

Figure 4.2. Composite sandwich test plate with attached framework and load cells for static or dynamic testing.

The aluminium frame that was firmly attached to the sandwich plate is used both as substitute for the bulkheads that would support such a panel in a ship, and to clamp the boundary as rigidly as possible. Rectangular areas limited by stiffeners as in a ship hull may be described mechanically as rectangular plates clamped along all four edges. The frame is shown in red

and grey in figure 4.2. The green contact points act like force transducers. The bottom (yellow) framework is used to mount the sandwich plate in the material test machine, and to transfer force during the experiment.

4.2 Laminate and core data for the test plate

The panel is built from a porous core with GRP laminates on either side. The core is a 25 mm H 200 plate with a weight of 210 kg/m^3. The laminates on both sides of the core are composed of a combination of two different glass fibre mats:

- 100 g/m^2 CSM M113-100-127-BS Vetrotex
- 2 x DBL 850 – E01 (425/199/199 – 0/45/-45) Devold AMT
- 100 g/m^2 CSM M113-100-127-BS Vetrotex
- Matrix: Synolite 0288 DSM

Table 4.1 gives the material properties of the multidirectional CSM mat (theoretical values), together with a unidirectional layer of the Devold mat. The zero-axis of the 0/45/-45 was oriented parallel to the shorter plate edge. As we see the stacking sequence of the laminate, $(0/45/-45/0/45/-45)_s$ (the two faces summed), gives an anisotropic lay-up, which means that we have to use the anisotropic formulas in section 2.5. If one of the zero-layers is replaced by a 90 degree layer, our laminate become (quasi)isotropic.

Material data	CSM*	Unidirectional**
E_x (MPa)	7500E6	28000E6
E_y (MPa)	7500E6	7500E6
E_z (MPa)	5000E6	7500E6
ν_{xy}	0.32	0.28
G_{xy} (MPa)	3000E6	2500E6
Density, ρ (kg/m^3)	1460	1650

Table 4.1 Material properties for CSM (theoretical) and unidirectional layer

** CSM/polyester, Weight% polyester = 35, Vol% polyester = 19*

*** UD-mat/polyester, Weight% polyester = 55, Vol% polyester = 35*

5 SIMULATIONS AND EXPERIMENTS

5.1 Load case and Finite Element Model (FEM)

The load case for the experiments is a concentrated force at the centre of the above mentioned sandwich plate, see figure 5.1. This is a rather simple load case and it is easy to obtain in the laboratory. The plate with attached framework is placed in a material test machine (MTS-810) and a steel cylinder generates the force at the centre, see figure 5.2. Applied force, time, strains at different locations and deflection in centre were recorded. The piston with the steel cylinder is hydraulically pressed down. The force and displacement are computer controlled. The displacement that is recorded is not the real deflection of the plate centre, but the displacement of the whole system (plate + frame). Therefore an analogue measuring clock was placed under the centre of the plate to measure the real deflection.

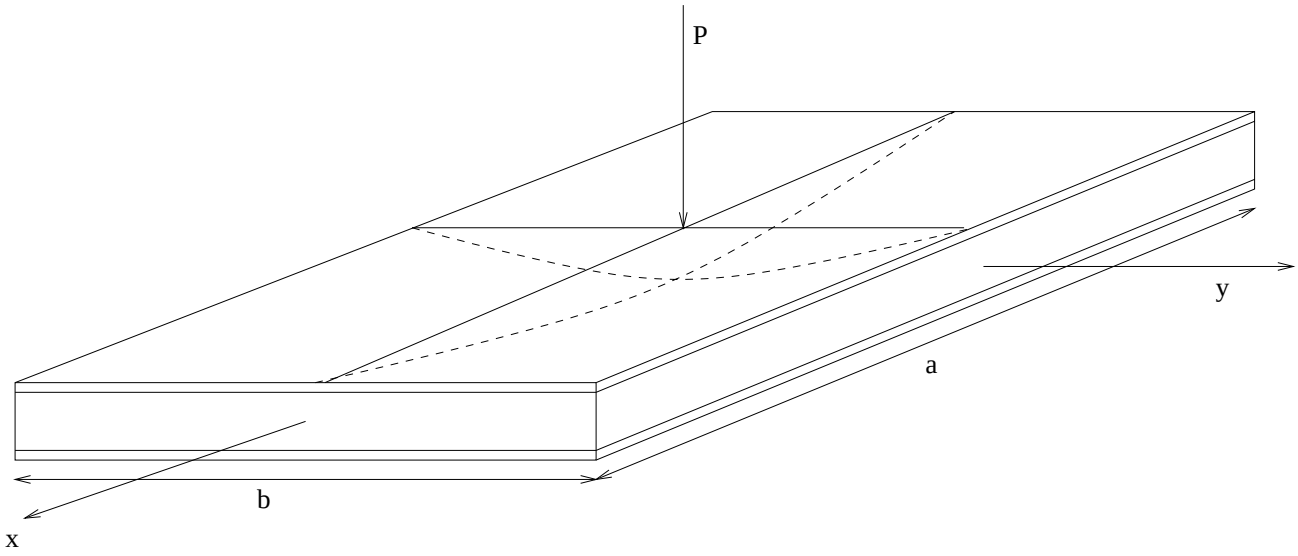

Figure 5.1. The load case: Rectangular sandwich plate with a concentrated load in centre.

Figure 5.2. The static test rig with sandwich plate and steel cylinder.

A Finite Element Model (FEM) of the same plate problem made in MSC/NASTRAN exists at FFI and has been used in earlier work in the CHESS program. In this report the model has been used for two purposes: Firstly, it has been used to simulate the experiments. The values of strains and shear stresses from the load case in the model will be compared to the same values obtained from the experiments. Some results from the simulations are shown in Appendix C and D. In this way we will try to verify the experimental method explained in chapter 2. Secondly, the model has been used to decide the distances that separate the strain gauges when calculating the strain gradients. This is explained further beneath.

5.2 Instrumentation

When we choose the points on the plate where we want to calculate the shear stresses, several considerations have to be made. The point load at the centre will for instance generate the greatest shear stresses where it acts on the plate. These shear stresses could be greater than the shear stresses along the clamped edges of the plate. To measure these stresses in the centre is of less importance for two reasons: On one hand the strain gradients here are so steep that it is practically impossible to measure the gradients accurately because the measuring points must be so close. On the other hand and more important, such a concentrated force is not recommended on a sandwich plate because it can generate large local deformations. The great shear stresses (and strains) that we experience here are not representative "outside the laboratory". The most relevant shear stresses act *along the clamping edges at the bottom side.* The points where we measure the strains to obtain the shear stresses in the experiment are therefore chosen here. From figure C.3 and C.4 in Appendix C we see that for the stress and strain shown there, the levels are highest on the *y*-axis. Furthermore, the greatest shear stresses along the clamping edges will act where the *x*- and *y*-axis in figure 5.1 meet the clamping. The condition is known as *cylindrical bending.* The curvature from the clamping is greatest here and therefore the strain gradients along the clamping also have their highest values at these four points.

5.2.1 Advantage of symmetry

In the general case we need 12 strain gauges to determine the shear stress values of τ_{xz} and τ_{yz}. This can be seen from equation (2.48)-(2.53) where we have six gradients that require two strain values each. In the general case we place our points off the *x*- or *y*-axis of the plate. In our case the points are on the axes, and we can take advantage of the symmetry in our problem. Figure 5.3 shows the two points on the axes close to the clamping. We realise that when the plate is statically deflected at the centre (or vibrates in first mode) the points on the *x*-axis have symmetry in the *y*-direction, and the points on the *y*-axis have symmetry in the *x*-direction. The gradients in these directions are therefore zero. This means that for each point we only have strain gradients in one direction, i e along the plate axis on which the point lies. The problem is therefore reduced from six strain gradients to three strain gradients for each of our points.

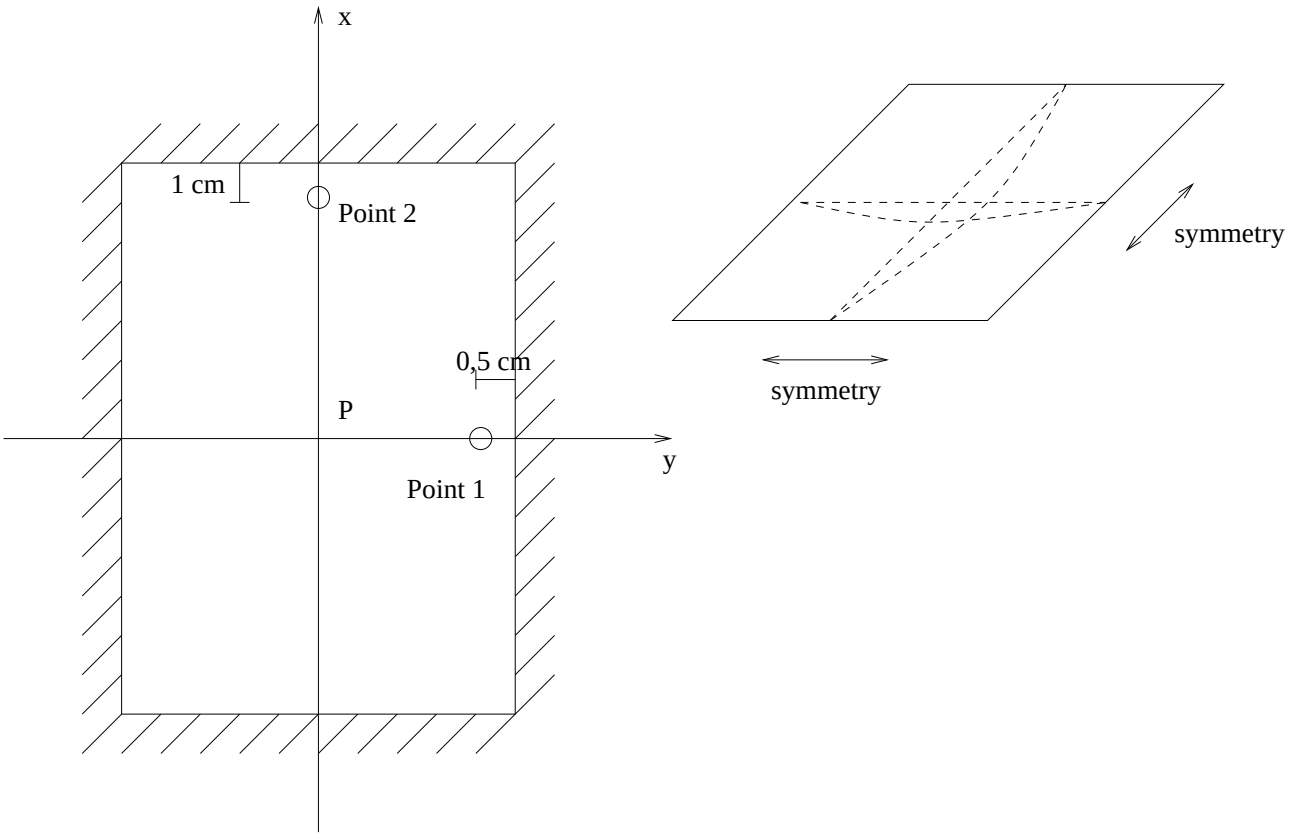

Figure 5.3. Chosen points on the plate axes close to the clamping edges on the bottom side.

5.3 Distances between measurement points for the strain gradient calculation

We still have to decide on the exact placement of the strain gauges, their separation when calculating the strain gradients for the two chosen points in figure 5.3. This is done with help of the simulated load case in the FEM model. In Appendix C some examples of contour plots of the strains and shear stresses are given for the outer CSM layer in the bottom face for a quarter plate. In Appendix D XY-plots are given for the strains needed in *x*-, *y*- and shear direction, but now only along the *x*- and *y*-axes for the same quarter panel, i.e. on the axes where our points are. These XY-plots show how the strain varies along the plate, or in other terms how the gradient changes. These plots are therefore useful when we choose our distances. Where the gradient is steep the distance must be short and where the gradient is gentle the distance between the gauges can be longer. As equation (2.48)-(2.53) show, we use a linear approximation for the gradients. The two points must therefore be in such a distance apart that the gradient between them is nearly linear. This is visualised in the plots in Appendix D, where the suitable distances are marked for each strain plot in order to obtain a linear gradient. Moreover Appendix D shows that the distances for the gradients in each point can be different depending on how steep the gradients in the *x-, y-* and 45°-direction are. This implies that the optimal points will not always be exactly in the middle of the two strain gauges that measure the gradients, but since the gradients are assumed to be linear, this is of secondary interest.

From Appendix D we have:

Point 1, *y*-axis:

$$\Delta y_x = 60mm \tag{5.1}$$

$$\Delta y_y = 10mm \tag{5.2}$$

$$\Delta y_{45} = 60mm \tag{5.3}$$

Point 2, *x*-axis:

$$\Delta x_x = 20mm \tag{5.4}$$

$$\Delta x_y = 85mm \tag{5.5}$$

$$\Delta x_{45} = 85mm \tag{5.6}$$

where the indexes *x, y* and *45* indicates the orientation of the strain gauges separated by the given distance. We observe that in equation (5.2) the distance is set to 10mm and not to 20mm as in figure D.1 and D.13 (Appendix D). The reason is, as we will see later, that we were unable to obtain agreement between model and experiments in this particular area close to the frame for point 1. On the background of later experiments a distance of 10mm was chosen, ie we use the closest strain gauge to the frame for point 1 in figure 5.4 b), ε_{ly}.

Figure 5.4 shows the instrumentation for each point, position and number for each strain gauge.

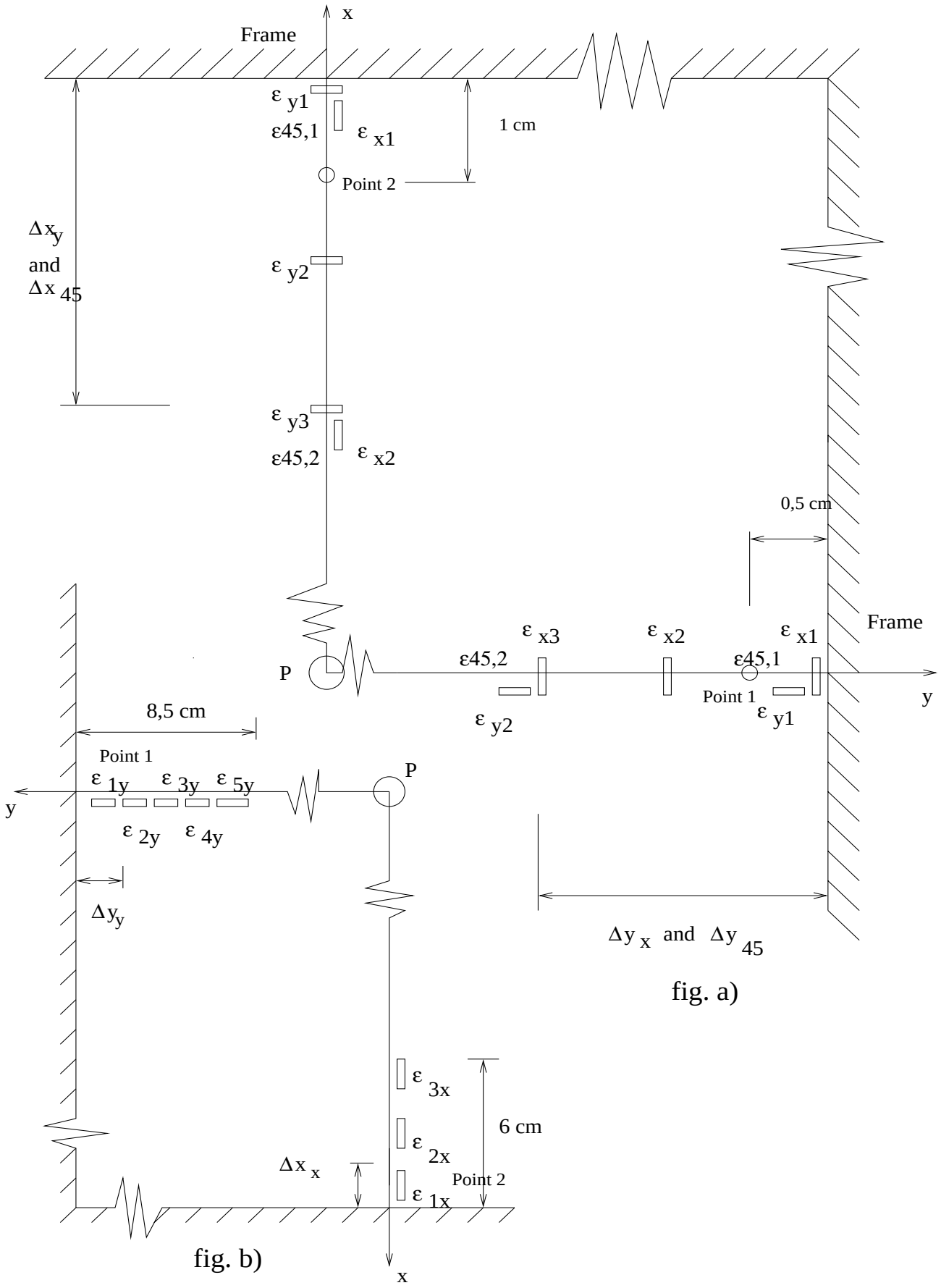

Figure 5.4 Positions and numbers of strain gauges for the two chosen points.

fig a): upper right hand quarter plate
fig b): lower left hand quarter plate

The XY-plots in Appendix D show that the strain is greatest in the *y*-direction for point 1 and in the *x*-direction for point 2. This is natural because the curvature is greatest here. The gradients are definitely also steepest in those directions. To check for agreement between experiments and simulations for these strains, several strain gauges are mounted with a short distance along the *y*-axis for point 1 and the *x*-axis for point 2, see figure 5.4 b). Figure 5.4 b) shows the opposite corner of the plate than figure 5.4 a). This means that the strain gauges in 5.4 b) are not at point 1 and 2, but as the plate is loaded in centre, the quarter plate in 5.4 a) and 5.4 b) experience the same strains. We can therefore use results from strain gauges in b) in the gradient calculations. The positions of the strain gauges in figure 5.4 b) are as follow: For point 1 starting from the frame: 10 mm, 20 mm, 40 mm, 60 mm and 80 mm. For point 2 starting from the frame: 20 mm, 30 mm and 55 mm. The photo in figure 5.5 shows the strain gauges in figure 5.4 a) for point 2 on the *x*-axis. All strain gauges used are TML, type FLA-6-11-1L, produced by Tokyo Sokki Kenkyujo Co. The gauge factor is 2.12, gauge resistance is 120 ohm and gauge length is 6 mm.

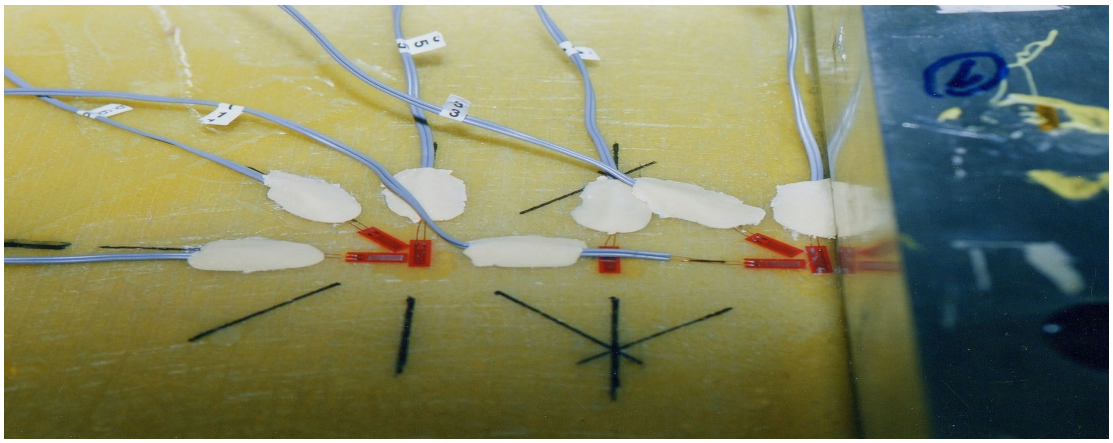

Figure 5.5. Strain gauges at point 2, figure 5.4 a).

The necessary strain gradients from equation (2.48)-(2.53) can now be expressed with reference to figure 5.4 as:

Point 1:

$$\frac{\partial \varepsilon_x}{\partial y} = \frac{\varepsilon_{x3} - \varepsilon_{x1}}{\Delta y_x} = \frac{\varepsilon_{x3} - \varepsilon_{x1}}{60mm} \tag{5.7}$$

$$\frac{\partial \varepsilon_y}{\partial y} = \frac{\varepsilon_{1y} - 0}{\Delta y_y} = \frac{\varepsilon_{1y}}{10mm} \tag{5.8}$$

$$\frac{\partial \gamma_{xy}}{\partial y} = \frac{\gamma_{(xy)2} - \gamma_{(xy)1}}{\Delta y_{45}} = \frac{\gamma_{(xy)2} - \gamma_{(xy)1}}{60mm} \tag{5.9}$$

The shear strain values in equation (5.9) are obtained from equation (2.56) and can be expressed as

$$\gamma_{(xy)1} = 2\varepsilon_{45,1} - (\varepsilon_{x1} + \varepsilon_{y1}) \tag{5.10}$$

$$\gamma_{(xy)2} = 2\varepsilon_{45,2} - (\varepsilon_{x3} + \varepsilon_{y2}) \tag{5.11}$$

Point 2:

$$\frac{\partial \varepsilon_x}{\partial x} = \frac{\varepsilon_{1x} - 0}{\Delta x_x} = \frac{\varepsilon_{1x}}{20mm} \tag{5.12}$$

$$\frac{\partial \varepsilon_y}{\partial x} = \frac{\varepsilon_{y3} - \varepsilon_{y1}}{\Delta x_y} = \frac{\varepsilon_{y3} - \varepsilon_{y1}}{85mm} \tag{5.13}$$

$$\frac{\partial \gamma_{xy}}{\partial x} = \frac{\gamma_{(xy)2} - \gamma_{(xy)1}}{\Delta x_{45}} = \frac{\gamma_{(xy)2} - \gamma_{(xy)1}}{85mm} \tag{5.14}$$

The shear strain values in equation (5.14) are again obtained from equation (2.56) and can be expressed as

$$\gamma_{(xy)1} = 2\varepsilon_{45,1} - (\varepsilon_{x1} + \varepsilon_{y1}) \tag{5.15}$$

$$\gamma_{(xy)2} = 2\varepsilon_{45,2} - (\varepsilon_{x2} + \varepsilon_{y3}) \tag{5.16}$$

In equation (5.8) and (5.12) the first strain value in the gradient is assumed to be zero. The distances here are so small that it is difficult to place a strain gauge and we know that the strain where the clamping ends is close to zero (fully clamped plate). Note also that ε_{ly} in equation (5.8) and ε_{lx} in equation (5.12) are from strain gauges in figure 5.4 b).

5.4 Quasi-static experiments

Two experiments of this type have been performed. One with load 5000 N in centre and another with load 10000 N. The panel was carefully loaded up to the decided forces as previous described. Because the amplifier only monitors six gauges at the same time, two measurements had to be done of the gauges for each point in figure 5.4 a). The first time we measure six of the gauges, and the second time we replace one of the six with the seventh remaining. In this way we also get an impression of the reproducibility of the strain values, which seems to be acceptable. For the strain gauges in figure 5.4 b) only one measurement for each point is necessary.

The test machine has no option to get a plot of microstrain versus force, but it is programmed to reach 5000 N after 800 seconds and 10000 N after 1600 seconds, which can be seen from the graphs. (The forces begin to increase from zero after about 60 seconds).

In this section the experimental results from the static testing are presented. They will be further discussed in section 5.6, together with dynamic test results presented in section 5.5. Figure 5.6 to 5.9 and table 5.1 to 5.4 show the results for the strain gauges in figure 5.4 a). Figure 5.10 to 5.13 and table 5.5 to 5.8 show the results from the strain gauges in figure 5.4b). The tables summarise the graphs. The measured strain values in the tables are rounded off to the nearest integer and given in με.

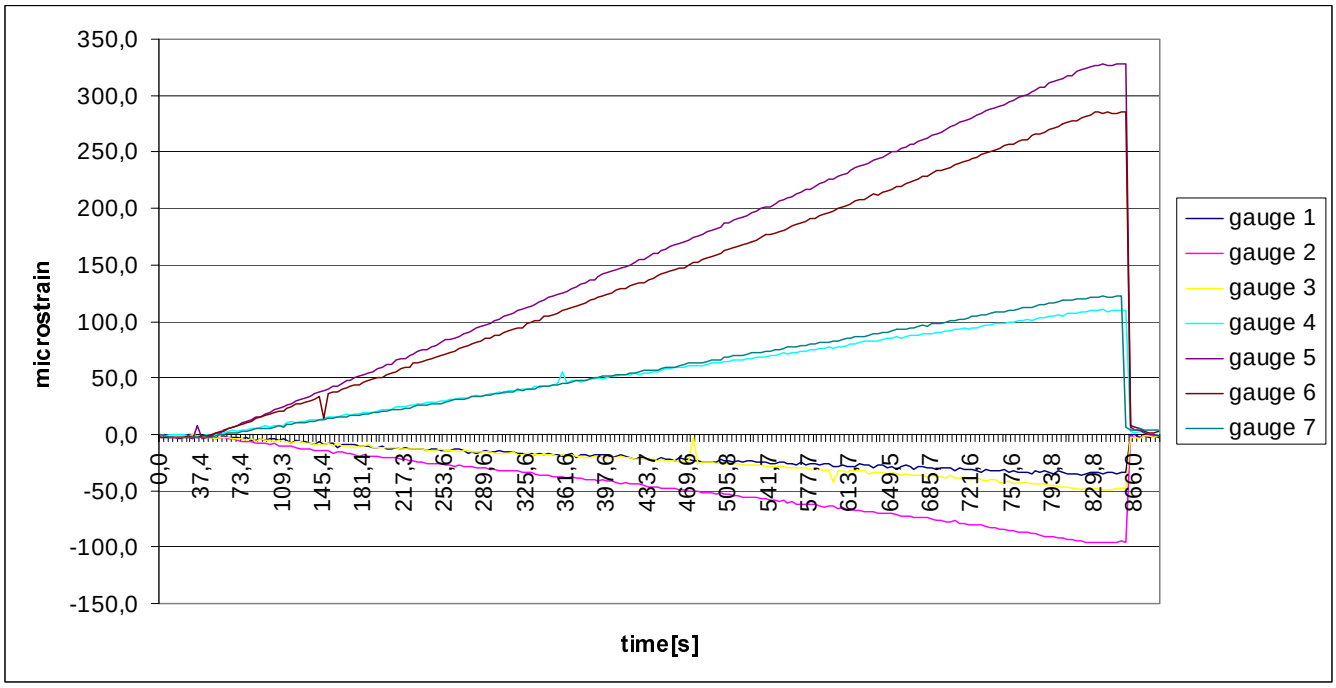

Figure 5.6 *Strain values at point 1 for the seven strain gauges, figure 5.4 a), with static lateral load up to 5000 N.*

1st run	1st run	1st run	1st run	1st run	1st run	**2nd run**	1st run
time(s)	gauge 1 ε_{x1}	gauge 2 ε_{y1}	gauge 3 $\varepsilon_{45,1}$	gauge 4 ε_{x2}	gauge 5 ε_{x3}	gauge 6 $\varepsilon_{45,2}$	gauge 7 ε_{y2}
853,8	**-33**	**-95**	**-48**	**110**	**328**	**286**	**122**

Table 5.1 *Maximum (or minimum) values at point 1, figure 5.4 a), with static lateral load 5000 N.*

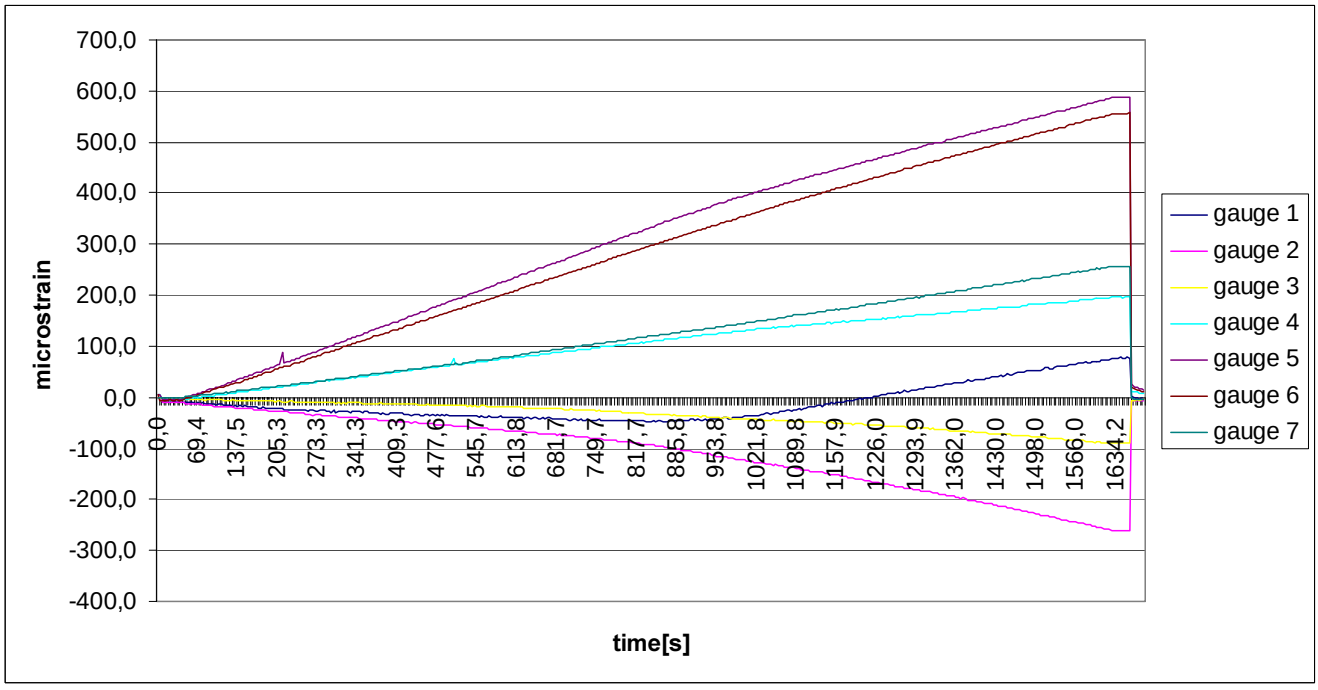

Figure 5.7 *Strain values at point 1 for the seven strain gauges, figure 5.4 a), with static latera1 load up to 10000 N.*

1st run	1st run	1st run	1st run	1st run	1st run	1st run	**2nd run**
time(s)	gauge 1 ε_{x1}	gauge 2 ε_{y1}	gauge 3 $\varepsilon_{45,1}$	gauge 4 ε_{x2}	gauge 5 ε_{x3}	gauge 6 $\varepsilon_{45,2}$	gauge 7 ε_{y2}
1658,1	**75**	**-261**	**-90**	**197**	**588**	**557**	**256**

Table 5.2 *Maximum (or minimum) values at point 1, figure 5.4 a), with static lateral load 10000 N.*

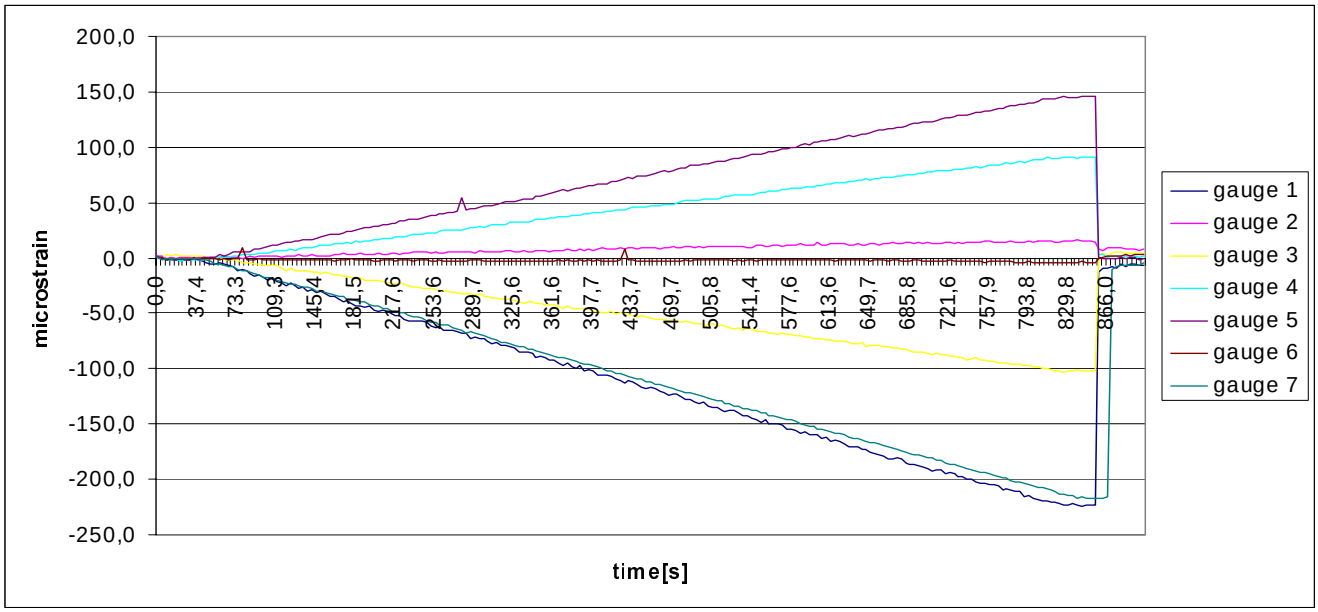

Figure 5.8 *Strain values at point 2 for the seven strain gauges, figure 5.4 a), at static lateral load up to 5000 N.*

1st run	1st run	1st run	1st run	1st run	1st run	1st run	**2nd run**
time(s)	gauge 1 ε_{x1}	gauge 2 ε_{y1}	gauge 3 $\varepsilon_{45,1}$	gauge 4 ε_{y2}	gauge 5 ε_{y3}	gauge 6 $\varepsilon_{45,2}$	gauge 7 ε_{x2}
849,8	**-223**	**15**	**-103**	**91**	**146**	**-5**	**-217**

Table 5.3 *Maximum (or minimum) values at point 2, figure 5.4 a), with static lateral load 5000 N.*

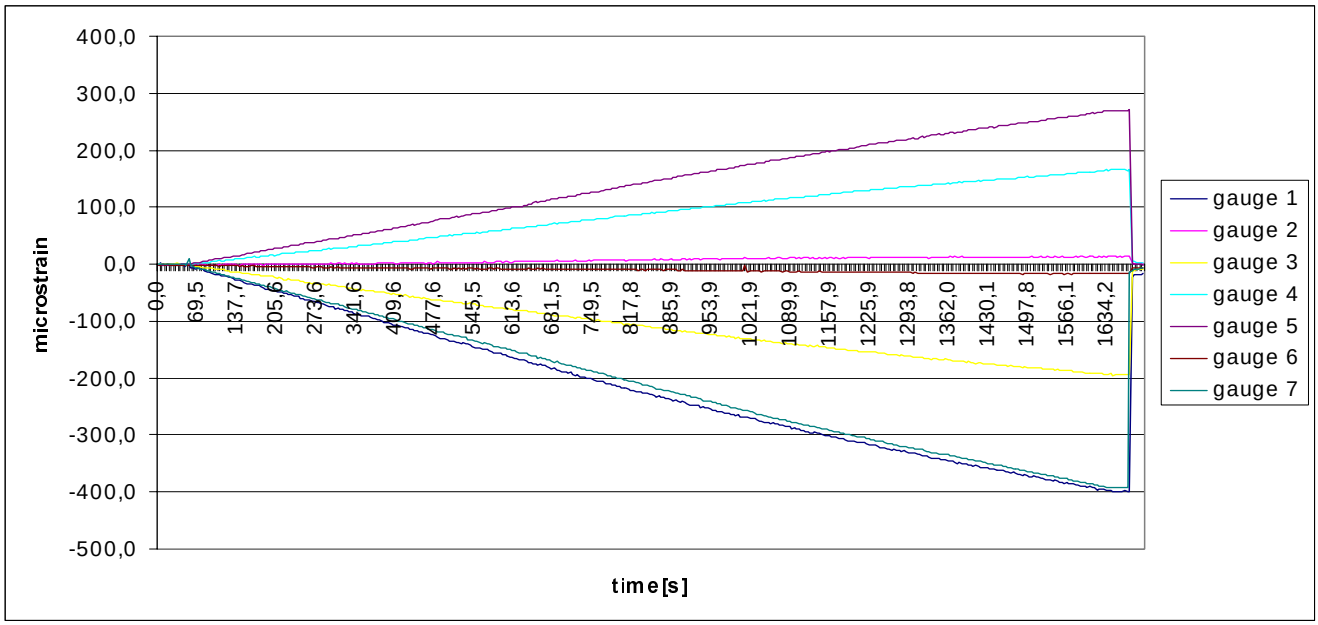

Figure 5.9 *Strain values at point 2 for the seven strain gauges, figure 5.4 a), at static lateral load up to 10000 N.*

1st run	1st run	1st run	1st run	1st run	1st run	1st run	**2nd run**
time(s)	gauge 1 ε_{x1}	gauge 2 ε_{y1}	gauge 3 $\varepsilon_{45,1}$	gauge 4 ε_{y2}	gauge 5 ε_{y3}	gauge 6 $\varepsilon_{45,2}$	gauge 7 ε_{x2}
1658,2	**-399**	**12**	**-194**	**166**	**270**	**-17**	**-392**

Table 5.4 *Maximum (or minimum) values at point 2, figure 5.4 a), with static lateral load 10000 N.*

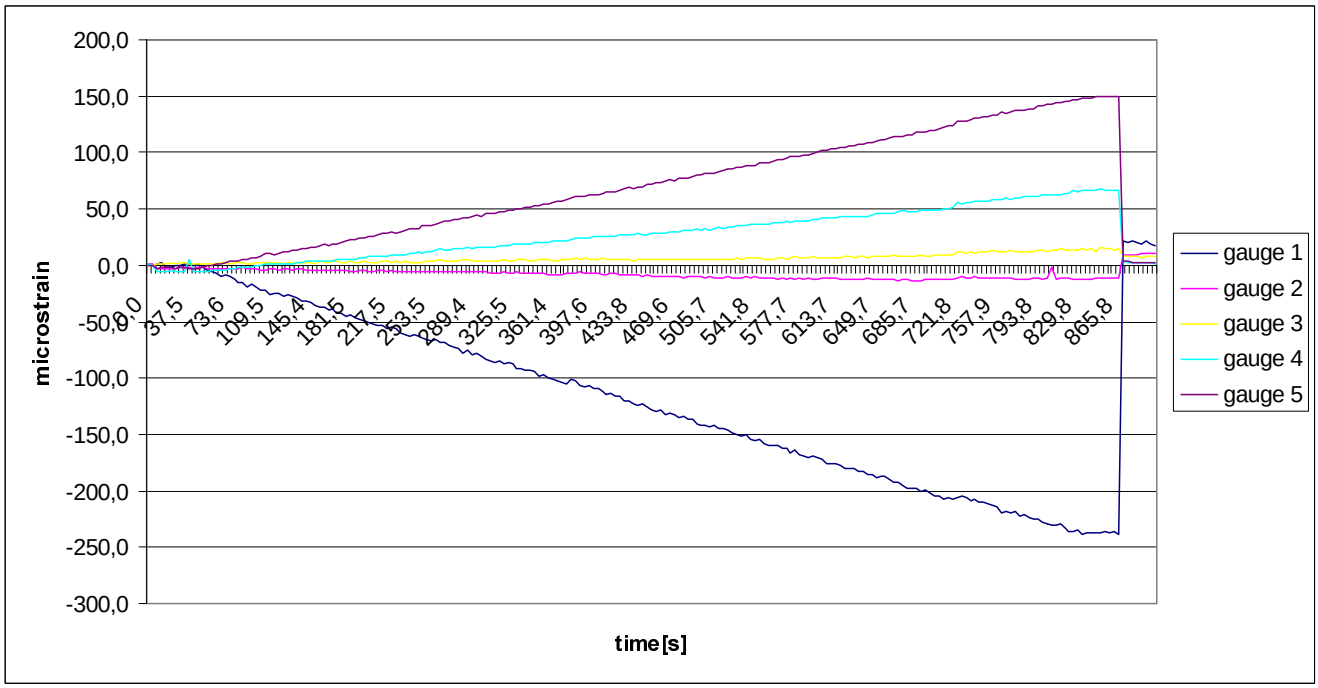

Figure 5.10 *Strain values at point 1 for the five strain gauges, figure 5.4 b), at static lateral load up to 5000 N.*

time(s)	gauge 1 ε_{1y}	gauge 2 ε_{2y}	gauge 3 ε_{3y}	gauge 4 ε_{4y}	gauge 5 ε_{5y}
865,8	**-239**	**-12**	**15**	**66**	**149**

Table 5.5 *Maximum (or minimum) values at point 1, figure 5.4 b), with static lateral load 5000 N.*

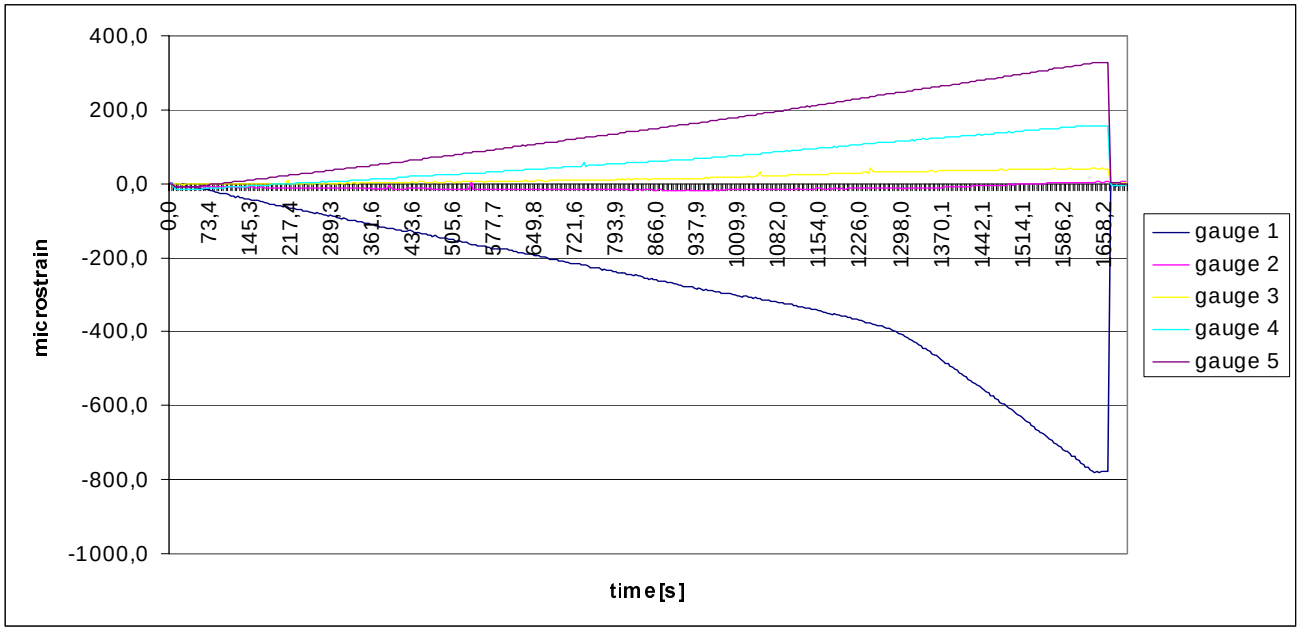

Figure 5.11 *Strain values at point 1 for the five strain gauges, figure 5.4 b), at static lateral load up to 10000 N.*

time(s)	gauge 1 ε_{1y}	gauge 2 ε_{2y}	gauge 3 ε_{3y}	gauge 4 ε_{4y}	gauge 5 ε_{5y}
1658,2	**-777**	**5**	**40**	**157**	**325**

Table 5.6 *Maximum (or minimum) values at point 1, figure 5.4 b), with static lateral load 10000 N.*

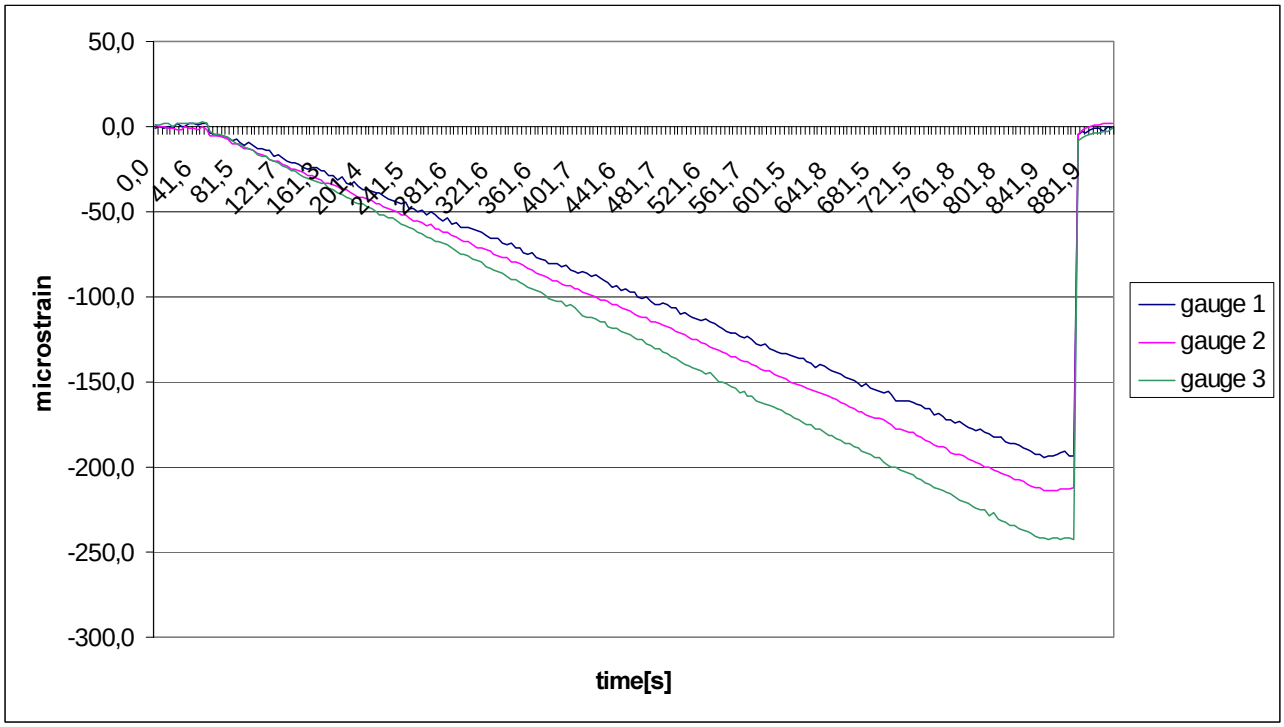

Figure 5.12 *Strain values at point 2 for the three strain gauges, figure 5.4 b), at static lateral load up to 5000 N.*

time(s)	gauge 1 ε_{1x}	gauge 2 ε_{2x}	gauge 3 ε_{3x}
865,5	**-194**	**-213**	**-242**

Table 5.7 *Maximum (or minimum) values at point 2, figure 5.4 b), with static lateral load 5000 N.*

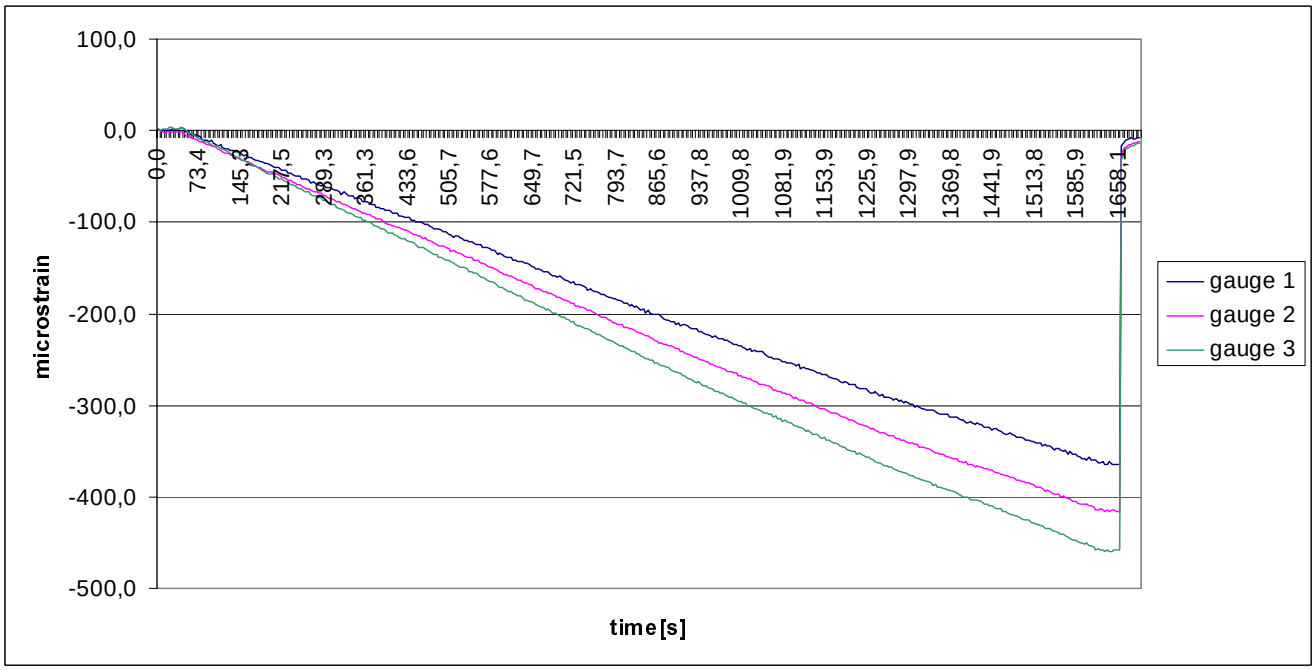

Figure 5.13 *Strain values at point 2 for the three strain gauges, figure 5.4 b), at static lateral load up to 10000 N.*

time(s)	gauge 1 ε_{1x}	gauge 2 ε_{2x}	gauge 3 ε_{3x}
1658,2	**-365**	**-415**	**-458**

Table 5.8 Maximum (or minimum) values at point 2, figure 5.4 b), with static lateral load 10000 N.

5.5 Dynamic experiments

Dynamic tests have been performed to see whether the strain gauges in figure 5.4 a) will give the same strains as in the static tests with identical load. The following figures 5.14-5.20 show the strain values at point 1 when a dynamic lateral load 5000 N with frequency 2 Hz acts in centre of the panel (identical to the static tests). Figure 5.21-5.27 show the same values for point 2. The tables show the maximum (or minimum) values. The results will be further discussed in section 5.6.

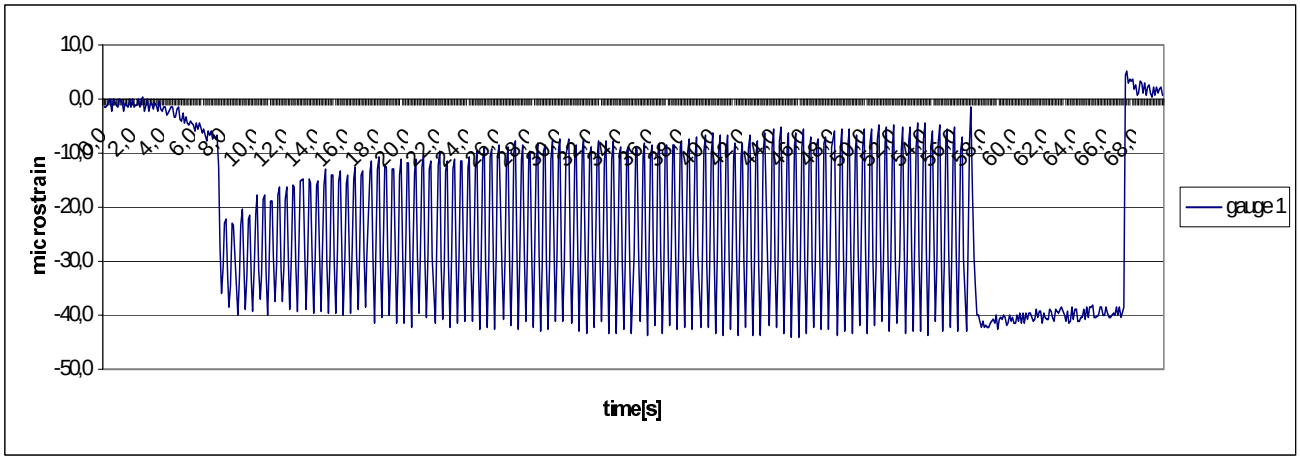

Figure 5.14 Strain gauge 1 at point 1 with dynamic lateral load 5000 N, 2 Hz.

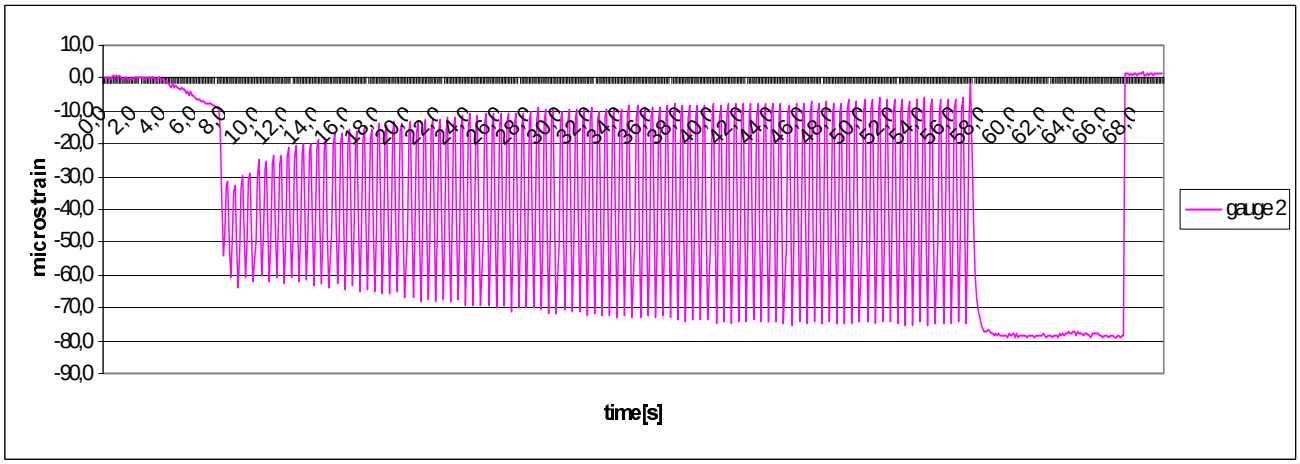

Figure 5.15 Strain gauge 2 at point 1 with dynamic lateral load 5000 N, 2 Hz.

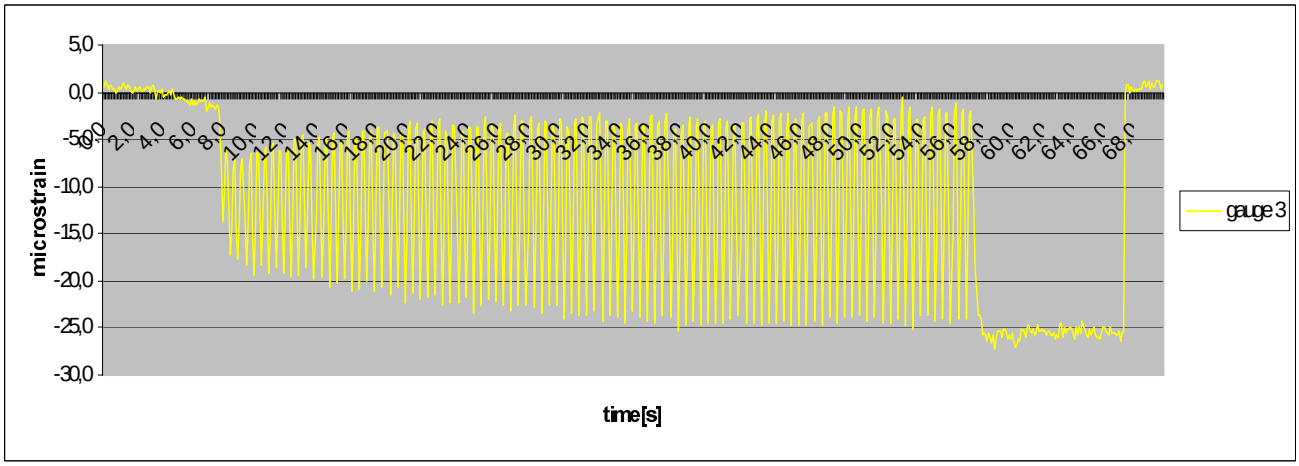

Figure 5.16 Strain gauge 3 at point 1 with dynamic lateral load 5000 N, 2 Hz.

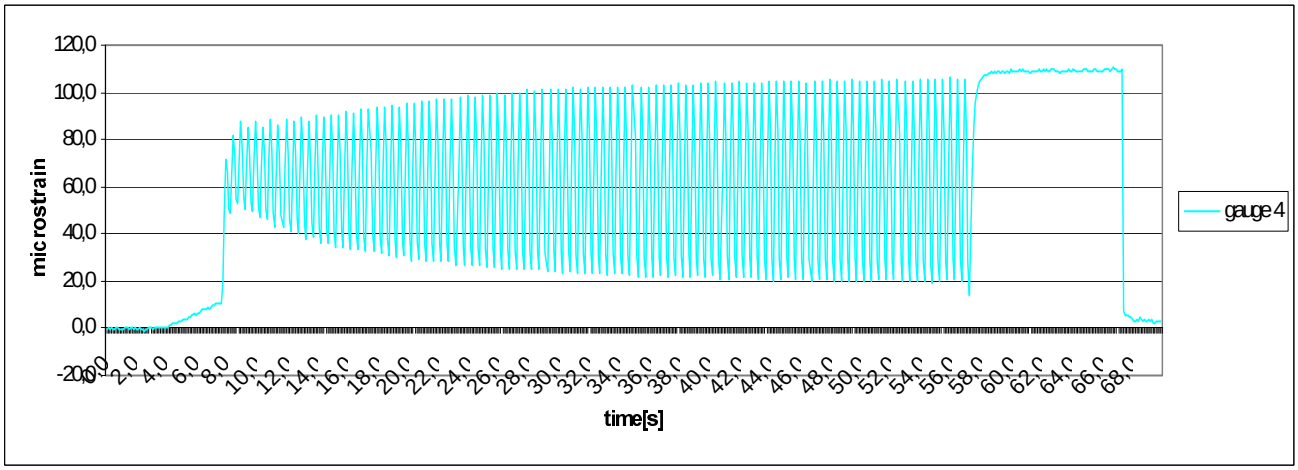

Figure 5.17 Strain gauge 4 at point 1 with dynamic lateral load 5000 N, 2 Hz.

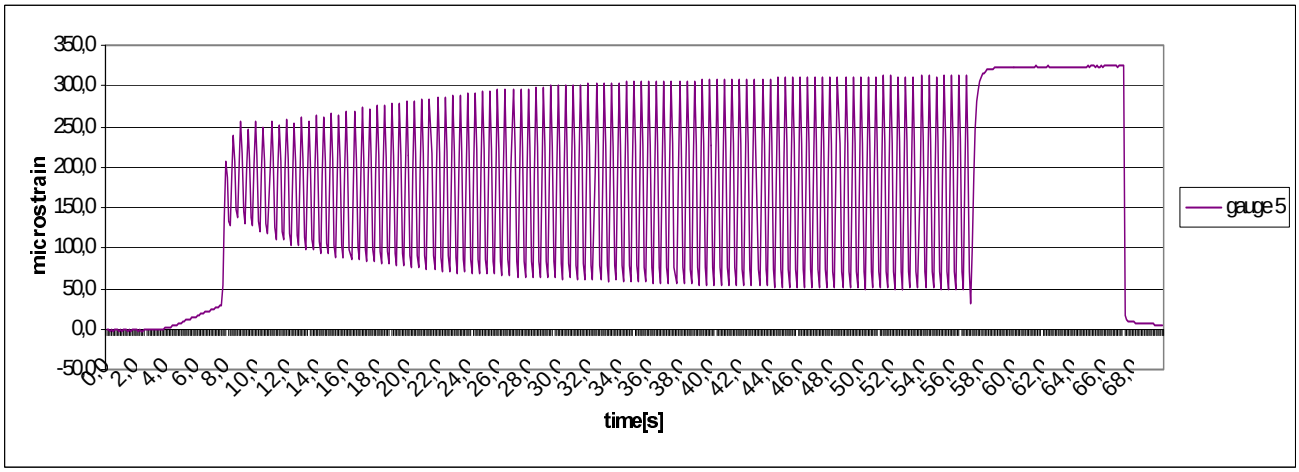

Figure 5.18 Strain gauge 5 at point 1 with dynamic lateral load 5000 N, 2 Hz.

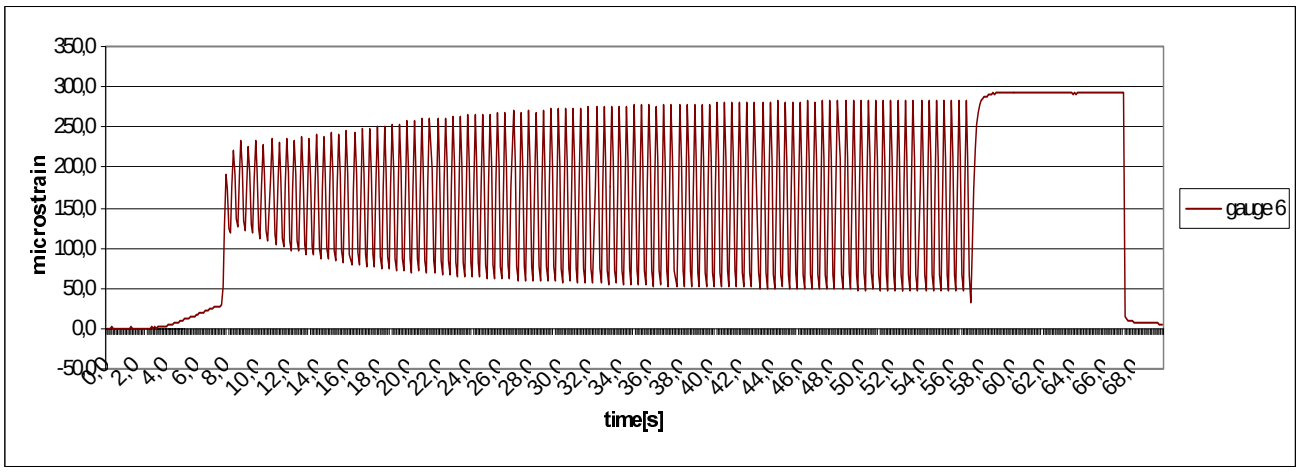

Figure 5.19 Strain gauge 6 at point 1 with dynamic lateral load 5000 N, 2 Hz.

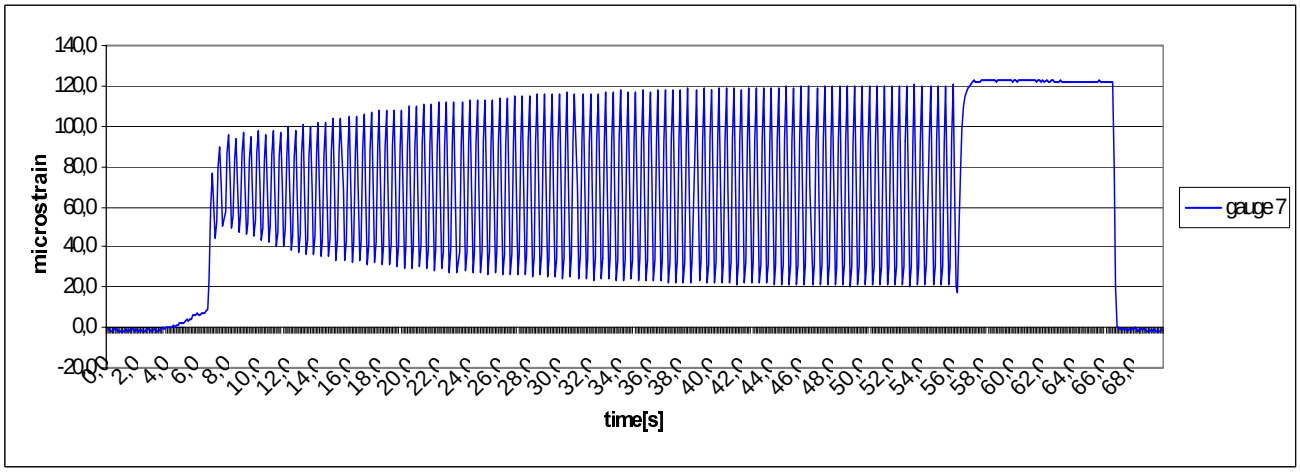

Figure 5.20 Strain gauge 7 at point 1 with dynamic lateral load 5000 N, 2 Hz.

1st run	1st run	1st run	1st run	1st run	1st run	1st run	**2nd run**
time(s)	gauge 1 ε_{x1}	gauge 2 ε_{y1}	gauge 3 $\varepsilon_{45,1}$	gauge 4 ε_{x2}	gauge 5 ε_{x3}	gauge 6 $\varepsilon_{45,2}$	gauge 7 ε_{y2}
66,5	**-40**	**-78**	**-26**	**110**	**325**	**293**	**122**

Table 5.9 Maximum (or minimum) values at point 1 with dynamic lateral load 5000 N, 2 Hz.

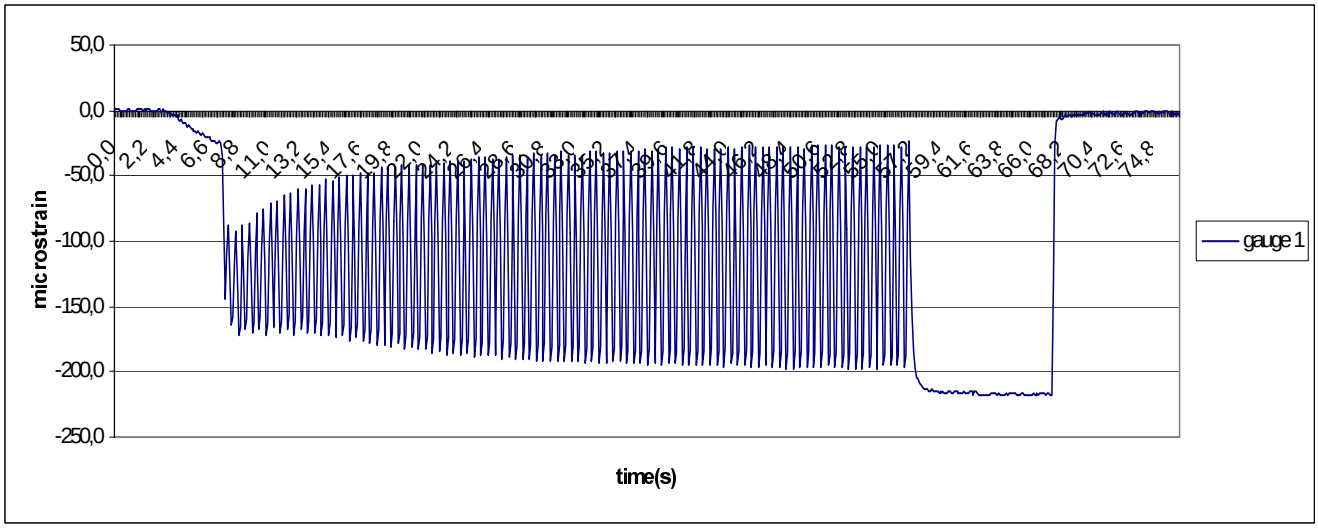

Figure 5.21 Strain gauge 1 at point 2 with dynamic lateral load 5000 N, 2 Hz.

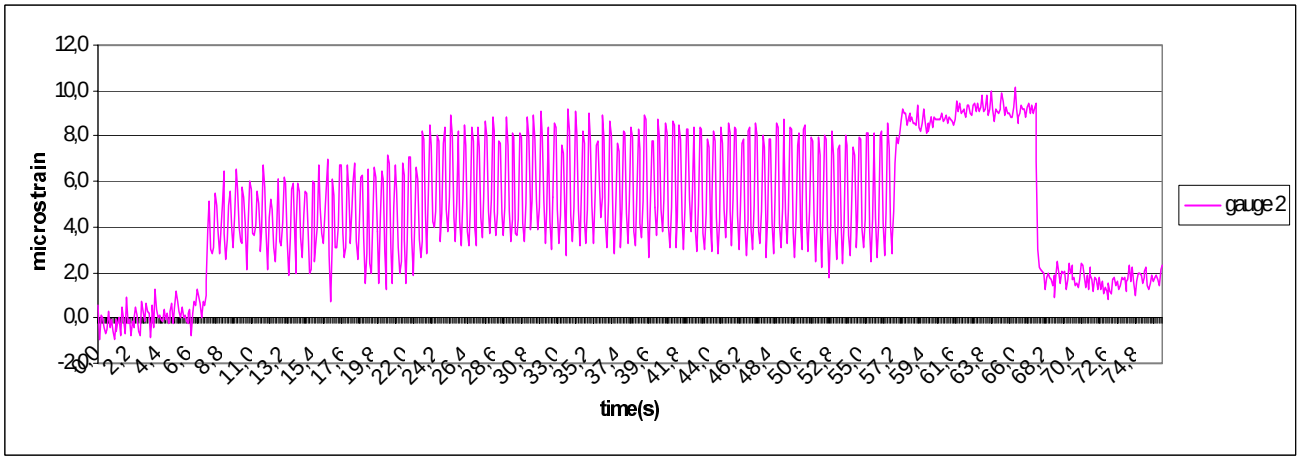

Figure 5.22 Strain gauge 2 at point 2 with dynamic lateral load 5000 N, 2 Hz.

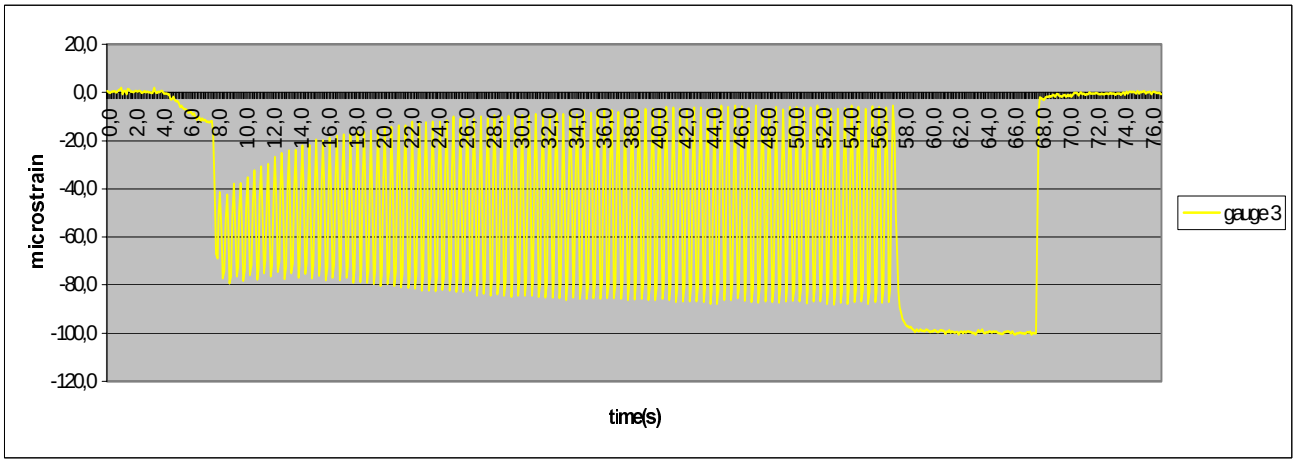

Figure 5.23 Strain gauge 3 at point 2 with dynamic lateral load 5000 N, 2 Hz.

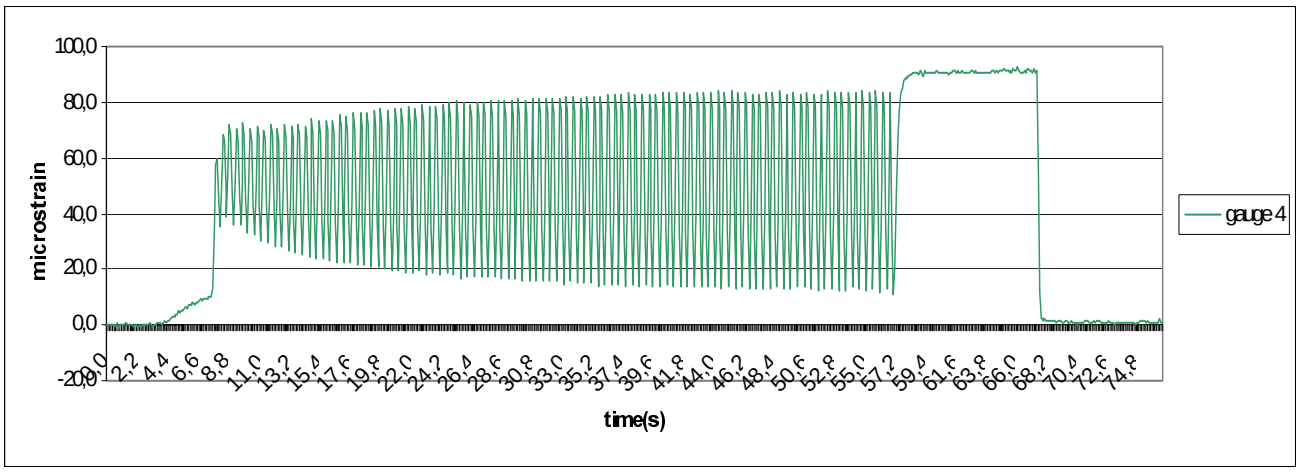

Figure 5.24 Strain gauge 4 at point 2 with dynamic lateral load 5000 N, 2 Hz.

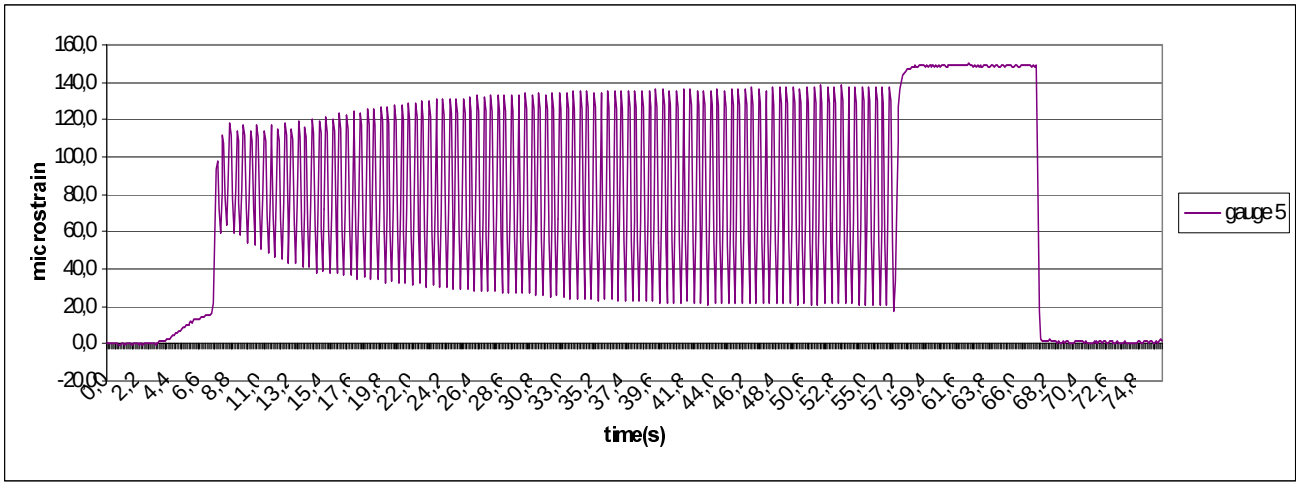

Figure 5.25 Strain gauge 5 at point 2 with dynamic lateral load 5000 N, 2 Hz.

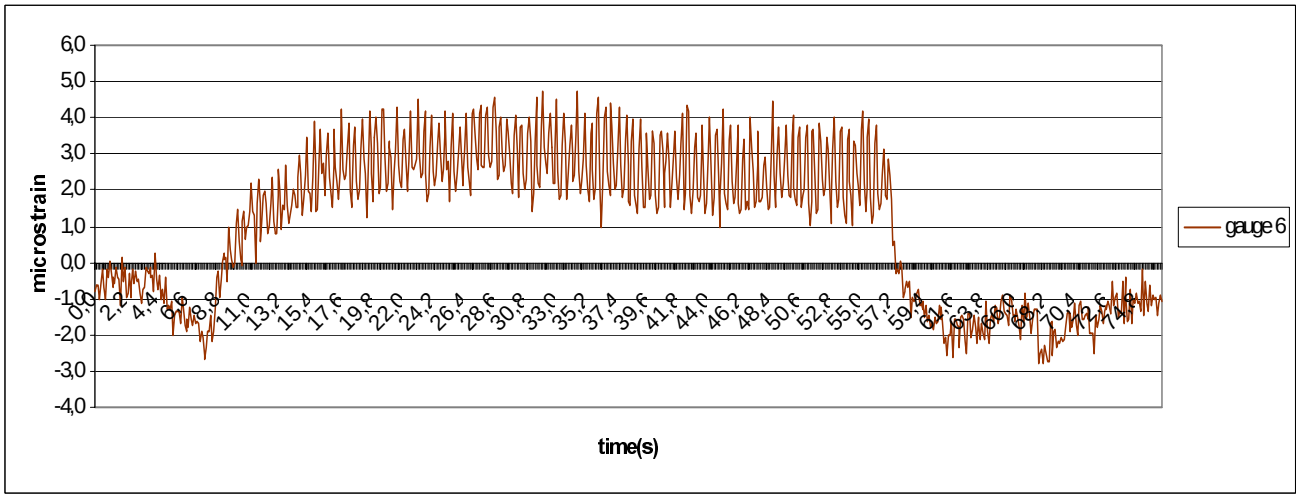

Figure 5.26 Strain gauge 6 at point 2 with dynamic lateral load 5000 N, 2 Hz.

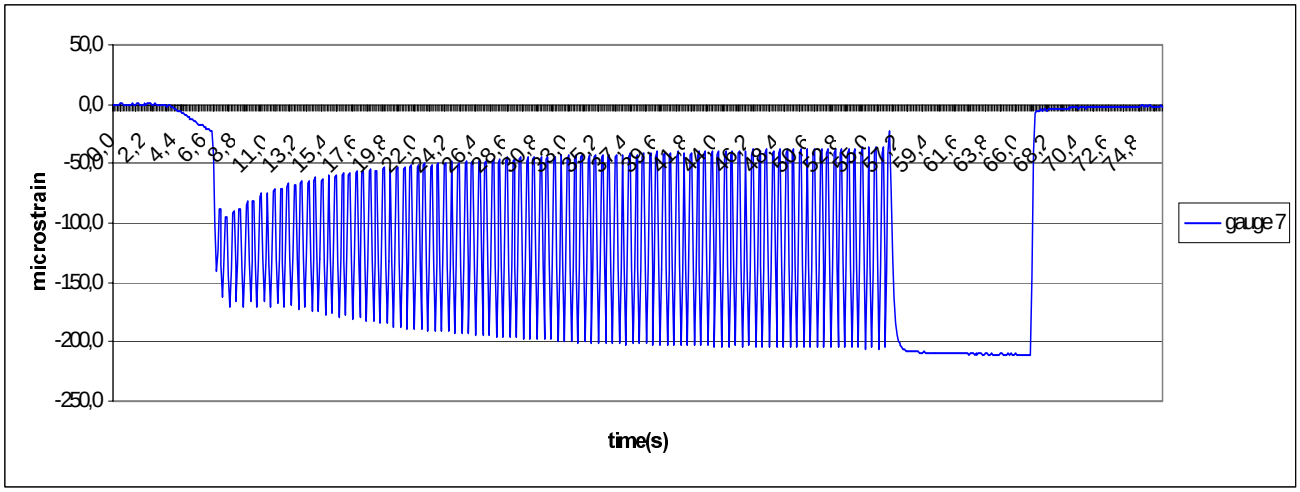

Figure 5.27 Strain gauge 7 at point 2 with dynamic lateral load 5000 N, 2 Hz.

1st run	1st run	1st run	1st run	1st run	1st run	1st run	**2nd run**
time(s)	gauge 1 ε_{x1}	gauge 2 ε_{y1}	gauge 3 $\varepsilon_{45,1}$	gauge 4 ε_{y2}	gauge 5 ε_{y3}	gauge 6 $\varepsilon_{45,2}$	gauge 7 ε_{x2}
66,5	**-218**	**9**	**-100**	**91**	**149**	**-2**	**-211**

Table 5.10 Maximum (or minimum) values at point 2 with dynamic lateral load 5000 N, 2 Hz.

5.6 Discussion of experiments

5.6.1 Quasi-static tests

Most of the experimental values seem reasonable. The strains increase as we come closer to the load area. However, the most interesting areas are close to the frame for both points, in the *y*-direction for point 1 and in the *x*-direction for point 2. As we can see from figure D.1 and D.13 (point 1) and figure D.8 and D.20 (point 2) in Appendix D, the strain in these directions varies most, and has indeed the steepest gradients. Especially for point 1 the strain gauges placed here have difficulties in measuring these strains. Point 2 has a greater distance to the load centre than point 1. The strain levels are therefore not so high and steep here and easier to measure. For point 1 the problem is critical for gauge 2 in table 5.1 and 5.2 and for gauge 1-3 in table 5.5 and 5.6. This will be further commented in section 5.7 where experimental and simulated values will be compared.

Close to the frame we would expect negative strain values. Because of the fully clamped plate edges, the curvature of the surface close to the frame has to shift from negative to positive, and so must the strain. This can be seen when we compare all the values in table 5.5 and 5.6. Another evidence of this is strain gauge 1 in figure 5.7. The strain is first negative and then becomes positive as the force increases. It is natural to believe that the “shift area” is pressed closer and closer to the frame when the force in centre increases, which explains the shift in sign for the strain gauge.

5.6.2 Dynamic tests

The dynamic test results are in good agreement with the static tests. Only strain gauges in figure 5.4 a) have been tested dynamically. All of them reach the same strain level as in the static tests. This is also as expected since the frequency is as low as it is (2 Hz). It is only when we reach the area of natural frequencies we can expect more serious deviations. Shear deformation and inertia problems can have great effect here. This is however outside the scope of this thesis, and is left as further work.

5.6.3 Calculation of shear strains

We will now use equation (5.10), (5.11), (5.15) and (5.16) to calculate shear strain values in the vicinity of point 1 and 2. These strains cannot be measured directly, we have to use the formula outlined in the end of section 2.7. The positions of the calculated shear strains are where the rosettes are placed in figure 5.4 a), which means that for each point we get two shear strain values. The values from equation (5.10), (5.11), (5.15) and (5.16) are given in table 5.11. For each point subscript 1 denotes the shear strain value closer to the frame and subscript 2 denotes the shear strain value at the greater distance from the frame.

Point 1	Point 1	Point 1	Point 1	Point 2	Point 2	Point 2	Point 2
5000 N	5000 N	10000 N	10000 N	5000 N	5000 N	10000 N	10000 N
eq (5.10)	eq (5.11)	eq (5.10)	eq (5.11)	eq (5.15)	eq (5.16)	eq (5.15)	eq (5.16)
$\gamma_{(xy)1}$	$\gamma_{(xy)2}$	$\gamma_{(xy)1}$	$\gamma_{(xy)2}$	$\gamma_{(xy)1}$	$\gamma_{(xy)2}$	$\gamma_{(xy)1}$	$\gamma_{(xy)2}$
32	**122**	**7**	**270**	**2**	**61**	**-2**	**89**

Table 5.11 Calculated shear strain values.

As we shall see in section 5.7 the shear strains should be close to zero. Taking into account errors in the measurement, values below 100 με are acceptable. The values 122 and 270 are therefore too high. One explanation for this is that the location for these measurements is so close to the steel cylinder that it influences the measurements more than first expected. The fact that we do not have the same problem for point 2 supports the explanation.

5.7 Comparison of measured and simulated strains

In this section tables will be given which compare the measured and simulated surface strains. All strain gauges (measured strains) in the tables are written with reference to figure 5.4, except the shear strain values, which were calculated in the above section. The simulated values are found from the graphs in Appendix D. Two simulations have been performed, one with load 5000 N and one with load 10000 N. In the FEM-model a steel ball and not a steel cylinder is pressed down at the centre of the plate. This gives a much greater deflection for the same force than using a steel cylinder. To overcome this problem we have measured the deflection of the plate centre in the performed tests. These deflections are used in the FEM-simulations rather than the forces to ensure the same deflection function. We believe that the more “distributed” load will not have significant effect on our measurements compared to a concentrated load because the areas of interest are close to the frame, and not close to the cylinder. The plate test with load 5000 N gave a deflection in centre of 1,80 mm and load 10000 N gave a deflection of 3,39 mm. Theses deflections are used in the FEM-simulations.

Table 5.12-5.15 show the comparisons (M – measured, S – simulated).

Point 1:

	ε_{1y}	ε_{y1}	ε_{2y}	ε_{3y}	ε_{4y}	ε_{y2}	ε_{5y}	ε_{x1}	ε_{x2}	ε_{x3}	$\gamma_{(xy)1}$	$\gamma_{(xy)2}$
M	***-239***	***-95***	***-12***	**15**	**66**	**122**	**149**	**-33**	**110**	**328**	**32**	***122***
S	***500***	***150***	***-800***	**50**	**50**	**50**	**180**	**50**	**100**	**325**	**0**	***0***

Table 5.12 Measured and simulated strains for point 1, 5000 N.

	ε_{1y}	ε_{y1}	ε_{2y}	ε_{3y}	ε_{4y}	ε_{y2}	ε_{5y}	ε_{x1}	ε_{x2}	ε_{x3}	$\gamma_{(xy)1}$	$\gamma_{(xy)2}$
M	***-777***	***-261***	***5***	**40**	**157**	**256**	**325**	**75**	**197**	**589**	**7**	***270***
S	***1050***	***230***	***-1500***	**100**	**150**	**170**	**450**	**120**	**220**	**630**	**0**	***0***

Table 5.13 Measured and simulated strains for point 1, 10000 N.

Point 2:

	ε_{1x}	ε_{x1}	ε_{2x}	ε_{3x}	ε_{x2}	ε_{y1}	ε_{y2}	ε_{y3}	$\gamma_{(xy)1}$	$\gamma_{(xy)2}$
M	**-194**	**-223**	**-213**	**-242**	**-217**	**15**	**91**	**146**	**2**	**61**
S	**-250**	**-250**	**-220**	**-210**	**-210**	**25**	**90**	**150**	**0**	**0**

Table 5.14 Measured and simulated strains for point 2, 5000 N.

	ε_{1x}	ε_{x1}	ε_{2x}	ε_{3x}	ε_{x2}	ε_{y1}	ε_{y2}	ε_{y3}	$\gamma_{(xy)1}$	$\gamma_{(xy)2}$
M	**-365**	**-399**	**-415**	**-458**	**-392**	**13**	**166**	**270**	**-2**	**89**
S	**-500**	**-500**	**-420**	**-400**	**-400**	**60**	**140**	**250**	**0**	**0**

Table 5.15 Measured and simulated strains for point 2, 10000 N.

What we see here is that the measured and simulated strains match quite well, except from the strain gauges placed closest to the clamping for point 1 (in italic in the tables). We have modified the FEM-model with a finer mesh in the area around the frame, see figure C.1 in Appendix C, but we have not succeeded in getting an agreement between model and measured values here. It seems from the tables like the shift area of the curvature is located closer to the frame in the experiments than in the model. Furthermore, the strain peaks are higher in the model, as we can see from figure D.1 and D.13 in Appendix D. The great positive peak from the model at the transition from frame to plate is impossible to measure. What we also see from the tables is that the simulated shear strains are (close to) zero. As mentioned in the section above some of the measured shear strains for point 1are therefore too high (also in italic in the tables). However, as we will see in the next chapter, the shear strains play a minor role in the calculations of the shear stresses in the core.

6 CALCULATION OF SHEAR STRESSES IN CORE

We are now ready to use the strain values found from the experiments and given in table 5.12-5.15 in our method for anisotropic plates from chapter 2, section 2.5. The sections to follow perform the necessary calculations for the two points. Also calculated are von Mises stresses from section 2.6. At the end all calculated shear stresses will be compared to the FEM simulations.

6.1 Calculation of transversal core shear stress from experimental results

As we saw in section 5.2.1 and 5.3 our choice of points to calculate the shear stresses results in a great deal of symmetry. Instead of six gradients we only have to deal with three along the *x*- and *y*-axes. For point 1 we have no gradients in the *x*-direction and for point 2 we have no gradients in the *y*-direction. This means that equation (2.40) and (2.41) for the shear forces will be simplified for our two points. We get:

Point 1:

$$Q_x = -\frac{2D_{xy}}{h}\frac{\partial \gamma_{xy}}{\partial y} \tag{6.1}$$

$$Q_y = \frac{2}{h}\left[D_y \frac{\partial \varepsilon_y}{\partial y} + \nu_{fyx} D_x \frac{\partial \varepsilon_x}{\partial y} \right] \tag{6.2}$$

Point 2:

$$Q_x = \frac{2}{h}\left[D_x \frac{\partial \varepsilon_x}{\partial x} + \nu_{fxy} D_y \frac{\partial \varepsilon_y}{\partial x} \right] \tag{6.3}$$

$$Q_y = -\frac{2D_{xy}}{h}\frac{\partial \gamma_{xy}}{\partial x} \tag{6.4}$$

The plate stiffnesses D_{ij} and Poisson's ratios ν_{fij} are given in Appendix B. h is the total plate thickness.

6.1.1 Load 5000 N

6.1.1.1 Point 1

The strain gradients for point 1 are calculated from equation (5.7)-(5.9). The necessary strain values from table 5.12 are inserted into the equations and we obtain:

$$\frac{\partial \varepsilon_x}{\partial y} = \frac{328+33}{60}\frac{\mu\varepsilon}{mm} = \underline{6{,}0\mu\varepsilon / mm} \tag{6.5}$$

$$\frac{\partial \varepsilon_y}{\partial y} = \frac{-239}{10}\frac{\mu\varepsilon}{mm} = \underline{-23{,}9\mu\varepsilon/mm} \tag{6.6}$$

$$\frac{\partial \gamma_{xy}}{\partial y} = \frac{122-32}{60}\frac{\mu\varepsilon}{mm} = \underline{1{,}5\mu\varepsilon/mm} \tag{6.7}$$

The gradients from the above three equations together with the plate stiffnesses and Poisson's ratios from Appendix B are inserted in equation (6.1) and (6.2) to obtain:

$$Q_x = \underline{-0{,}2N/mm} \tag{6.8}$$

$$Q_y = \underline{-20{,}2N/mm} \tag{6.9}$$

We finally obtain the shear stresses from equation (2.33) and (2.34):

$$\tau_{xz} = \frac{Q_x}{c} = -0{,}01N/mm^2 = \underline{\underline{-0{,}01MPa}} \tag{6.10}$$

$$\tau_{yz} = \frac{Q_y}{c} = \underline{\underline{-0{,}81MPa}} \tag{6.11}$$

where c is the core thickness.
If we look at the calculated gradients, equation (6.5)-(6.7), we see that the gradient for ε_y is much greater than the two other gradients. The error we do when neglecting the gradients for ε_x and γ_{xy} will therefore be small. The shear forces will after this simplification be expressed as:

$$Q = 0 \tag{6.12}$$

$$Q_y = \frac{2D_y}{h}\frac{\partial \varepsilon_y}{\partial y} \tag{6.13}$$

The new shear forces inserted into equation (2.33) and (2.34) yield:

$$\tau_z = 0 \tag{6.14}$$

$$\tau_{yz} = \underline{\underline{-0{,}87MPa}} \tag{6.15}$$

6.1.1.2 Point 2

The strain gradients for point 2 are calculated from equation (5.12)-(5.14). In the same way the necessary strain values, now from table 5.14, are inserted into the equations to obtain:

$$\frac{\partial \varepsilon_x}{\partial x} = \frac{-194}{20}\frac{\mu\varepsilon}{mm} = \underline{-9{,}7\mu\varepsilon/mm} \tag{6.16}$$

$$\frac{\partial \varepsilon_y}{\partial x} = \frac{146-15}{85}\frac{\mu\varepsilon}{mm} = \underline{1{,}5\mu\varepsilon / mm} \tag{6.17}$$

$$\frac{\partial \gamma_{xy}}{\partial x} = \frac{61-2}{85}\frac{\mu\varepsilon}{mm} = \underline{0{,}7\mu\varepsilon / mm} \tag{6.18}$$

The gradients from the above three equations together with the plate stiffnesses and Poisson's ratios from Appendix B are similarly used in equation (6.3) and (6.4) to obtain:

$$Q_x = \underline{-4{,}5N / mm} \tag{6.19}$$

$$Q_y = \underline{-0{,}1N / mm} \tag{6.20}$$

We finally obtain the shear stresses from equation (2.33) and (2.34):

$$\tau = \frac{Q}{c} = \underline{\underline{-0{,}18MPa}} \tag{6.21}$$

$$\tau_{yz} = \frac{Q_y}{c} = \underline{\underline{-0{,}004MPa}} \tag{6.22}$$

Furthermore we realise that for this point the gradient for ε_x is much greater than the other two. We therefore ignore the gradients for ε_y and γ_{xy}. The shear forces are now expressed as:

$$Q_x = \frac{2D_x}{h}\frac{\partial \varepsilon_x}{\partial x} \tag{6.23}$$

$$Q = 0 \tag{6.24}$$

The new shear forces inserted into equation (2.33) and (2.34) yield:

$$\tau_z = \underline{\underline{-0{,}20MPa}} \tag{6.25}$$

$$\tau_{yz} = 0 \tag{6.26}$$

6.1.2 Load 10000 N

The procedure is the same as in section 6.1.1. All the details will therefore not be shown here. Only the final results for the shear stresses will be given.

6.1.2.1 Point 1

Necessary values from table 5.13 are used to calculate the gradients in equation (5.7)-(5.9). The gradients are used in equation (6.1) and (6.2) and we obtain the shear forces. Finally we find the shear stresses to be:

$$\tau_z = \underline{\underline{-0{,}02 MPa}} \tag{6.27}$$

$$\tau_{yz} = \underline{\underline{-2{,}74 MPa}} \tag{6.28}$$

We do the same simplifications as in section 6.1.1.1 and obtain the new shear stresses as:

$$\tau_z = 0 \tag{6.29}$$

$$\tau_{yz} = \underline{\underline{-2{,}82 MPa}} \tag{6.30}$$

6.1.2.2 Point 2

The gradients, equation (5.12)-(5.14), are now calculated with values from table 5.15. Equation (6.3) and (6.4) give the shear forces and we obtain the shear stresses as:

$$\tau_z = \underline{\underline{-0{,}34 MPa}} \tag{6.31}$$

$$\tau_{yz} = \underline{\underline{-0{,}006 MPa}} \tag{6.32}$$

The same simplifications as in section 6.1.1.2 now give

$$\tau_z = \underline{\underline{-0{,}37 MPa}} \tag{6.33}$$

$$\tau_{yz} = 0 \tag{6.34}$$

6.2 Calculation of von Mises stresses in the core

In section 2.6 the fracture formula for the core based on the von Mises criterion was outlined. As we can see it only depends on the shear stresses calculated in section 6.1. The expression is repeated below.

$$\tau = \sqrt{3(\tau_{xz}^{\ 2} + \tau_{yz}^{\ 2})} \geq \tau_{core,max} \tag{6.35}$$

Our core material is H 200 from Divinycell. The maximum shear stress for this core material is 3,3 MPa (given from the manufacturer).

$$\tau_{H200,max} = 3{,}3 MPa \tag{6.36}$$

Table 6.1 shows the results when we use equation (6.35) on our shear stress values from section 6.1. Exact value means that all three gradients are used in the calculations. Simplified value means that only the steepest gradient is used.

	Point 1	Point 1	Point 2	Point 2
	5000 N	10000 N	5000 N	10000 N
exact	**1,40 MPa**	**4,74 MPa**	**0,31 MPa**	**0,59 MPa**
simplified	**1,51 MPa**	**4,88 MPa**	**0,34 MPa**	**0,64 MPa**

Table 6.1 Von Mises stresses in the core material.

As we can see the von Mises stress at point 1 for 10000 N is higher than the limit in equation (6.36). Possible reasons for this will be discussed in chapter 7, but we have seen no evidence of shear fracture in the core material. Still, fracture is difficult to detect when it is only present in the core. The only way to see if fracture has occurred, is to remove the faces (without damaging the core) and thereby destroy the plate. Table 6.1 will be further discussed in chapter 7.

6.3 Comparison with simulated core shear stresses

In this section tables will be given which compare the calculated and simulated core shear stresses, both τ_{xz}, τ_{yz} and von Mises. The results will be commented and discussed in chapter 7. For the calculated values in the tables, the numbers in parentheses represent the simplified values from section 6.1. Again, simulated values are found in Appendix D.

	Point 1	Point 1	Point 2	Point 2
	5000 N	10000 N	5000 N	10000 N
Calculated	**-0,01 (0)**	**-0,024 (0)**	**-0,18 (-0,20)**	**-0,34 (-0,37)**
Simulated	**0**	**0**	**-0,05**	**-0,10**

Table 6.2 Comparison of τ_{xz} (MPa).

	Point 1	Point 1	Point 2	Point 2
	5000 N	10000 N	5000 N	10000 N
Calculated	**-0,81 (-0,87)**	**-2,74 (-2,82)**	**-0,004 (0)**	**-0,006 (0)**
Simulated	**(-)0,60**	**(-)1,10**	**0**	**0**

Table 6.3 Comparison of τ_{yz} (MPa).

	Point 1	Point 1	Point 2	Point 2
	5000 N	10000 N	5000 N	10000 N
Calculated	**1,40 (1,51)**	**4,74 (4,88)**	**0,31 (0,34)**	**0,59 (0,64)**
Simulated	**1,0**	**1,90**	**0,08**	**0,15**

Table 6.4 Comparison of von Mises stresses (MPa).

The reason for the minus signs in parentheses for two of the simulated values in table 6.3 is the choice of local coordinate system in the elements in the FEM-model. It is chosen opposite

compared to our global choice, shown for instance in figure 5.3. This results in the two shear stresses being positive in the simulations, but according to our definition used in the experimental method, they have to be negative.

7 DISCUSSION, CONCLUSION AND FURTHER WORK

7.1 Discussion and comparison of shear stress values

As we can see from table 6.1 and 6.4 all von Mises stresses from the experimental method are below the allowed limit, equation (6.36), except the values for point 1, 10000 N. The direct reason for this is the high strain value ε_{1y} from figure 5.11 and table 5.6. The strain gauge is mounted as close to the frame as possible. As commented earlier when the load is as high as 10000 N the shift area for the curvature is pressed closer and closer to the frame for the fully clamped plate. The strain value will therefore become more and more negative. If we compare all strain values in table 5.6 there is reason to believe that this shift area is located right after ε_{1y}. Figure 5.11 shows that the next strain gauge, ε_{2y}, goes from negative values for low forces to a small positive value for the final 10000 N force. The location of the shift area is probably the reason for the high (negative) value for ε_{1y}. What is strange is that the strain does not progress linearly. After about 1300 s (ca. 7000 N) it increases faster than before. The reason for this can still be the shift area, but the sudden increase in strain can also be caused by a growing core separation. A core crack will make the local structure less stiff. However, what is most likely is that we have seen the effects of a very local first ply failure (FPF) in the face. First ply failure means that fracture occurs in the matrix that bonds the fibres together. The fibres will thereby take all the strain directly. First ply failure curves will typically have the shape shown in figure 5.11. We see a linear increase before and after the crack but with different slopes. If we now assume that first ply failure has not occurred we extrapolate the first part of the curve up to the final load and thereby get the same slope in the whole load interval. This is shown by the dashed line in figure 5.11. The new strain value now becomes -500 με. Redoing the calculations we find a shear stress value of 1,73 MPa (exact) and 1.81 MPa (simplified). The von Mises stress becomes 2,99 MPa (exact) and 3.14 MPa (simplified). We see that the stresses are now below the limit in equation (6.36), but the new calculated values for point 1, 10000 N, are still higher than the corresponding simulated values in table 6.3 and 6.4.

From table 6.2-6.4 we see that the calculated (experimental) stresses approximated to zero are in good agreement with the FEM-model. However, the other calculated shear stresses are in general somewhat higher than the simulated stresses. We must, however, be aware that our FEM-model has some important weaknesses. The plate is modelled with linear shell elements in the layers in the faces, QUAD4, and linear solid elements for the core, HEXA8. One has found that the composite module in NASTRAN does not calculate the stresses correctly in all cases. The staff at FiReCo a.s has concluded that, in fact, the stresses may be estimated *lower* than they really are according to analytical solutions of simple cases. If this is true for our plate we would expect the analytical values to be higher than the simulated values. As shown above this is also what we see.

We now calculate the fraction S/C (simulated/calculated stresses). In this way we quantify how much the simulated values are below the analytical. For point 1 at 10000 N we have ignored first ply failure and used the new values found in this section. Table 7.1 shows the results. All calculated values are exact values.

Point 1	Point 1	Point 1	Point 1	Point 2	Point 2	Point 2	Point 2
5000 N	10000 N	5000 N	10000 N	5000 N	10000 N	5000 N	10000 N
S/C τ_{yz}	S/C τ_{yz}	S/C Mises	S/C Mises	S/C τ_{xz}	S/C τ_{xz}	S/C Mises	S/C Mises
0,74 **26%**	**0,64** **36%**	**0,71** **29%**	**0,64** **36%**	**0,28** **72%**	**0,29** **71%**	**0,25** **75%**	**0,25** **75%**

Table 7.1 *Fractions: Simulated/Calculated stresses.*
Percentages: Show by how much the simulated values are below the analytical values.

We see that the differences between simulations and calculations are greater for point 2 than 1. This is perhaps logical because the strain levels are much smaller for point 2 than 1 and the stresses may therefore be harder to calculate accurately. On the other hand it is easier to measure the strains at point 2 where we do not have the steep gradients as in point 1. It benefits the method that it becomes more accurate for higher strain levels, ie the closer we come to the fracture toughness of the core. Furthermore, what can be concluded from table 7.1 and also 6.2-6.4 is that the fracture formula based on the von Mises criterion is a correct assumption. We see from table 7.1 that the fractions and percentages for von Mises match the corresponding shear stress fractions and percent numbers. Further, if we use equation (6.35) on the simulated values in table 6.2 and 6.3, we get the same answers as the simulated values in table 6.4.

7.2 Limitations

The strain gradient method outlined and tested in this report now handles both isotropic and anisotropic sandwich panels. The theory of the cases is explained in section 2.4 and 2.5. As we see the method is able to deal with changes in mechanical properties in faces as well as core. In this section the limitations of the method will be summarised. We must remember that the list in section 2.2 still underlays all theory and experiments. If we focus on what we may call "geometrical" assumptions (1, 4, 7 and 11) the method is only valid when:

- The core material is much thicker than the two faces.
- The faces are made from a given number of plies of orthotropic materials, which are bound together. The orthotropic axes in the individual plies do not have to coincide with the global *x*- and *y*-axes for the plate.
- The plate displacements are small compared to the plate thickness.
- Core and faces have constant thickness.

All these four assumptions are normally fulfilled for sandwich plates in common use, but there can exist plates with rather thick faces. The reason for the third point is that our theory is a first order theory – it requires small deformations.

The most important limitation for the method is different stacking and materials in the two faces. The faces can also have different thickness. This leads to different mechanical properties (Young's moduli and Poisson's ratios) for the two faces. One can in principle calculate the mechanical properties for each of the faces and from this calculate the plate stiffnesses. We then have to sum up face + core + face in our equations for the plate stiffnesses, and not what we have done before: 2×face + core. Another problem arises when we do not know exactly where the neutral axis in the plate is located. This has to be determined before we can calculate the plate stiffnesses. We cannot assume as we did when we had equal faces that it is located in the middle of the plate and thereby set $z=h/2$ in equation (2.22). When we had identical faces we had equal surface strain (with opposite signs) in the two faces. This is no longer the case, but expressions exist in the mechanics of materials, that allows the new location of the neutral axis to be determined. The case of different faces is obviously more complicated, and the practical difficulties may be too big for a solution to be found.

7.3 Conclusion and further work

This report demonstrates that the proposed method is valid also for practical measurements of the shear stresses in sandwich plates, with some practical limitations or weaknesses that will be summarised in this section. Alone or as a part of a larger hull monitoring system the method gives an estimate of the shear stress values in the core and a reason for closer investigation of the sandwich panel under consideration if measured values exceed allowable limits. It also seems that the method is more accurate for higher strain- and stress levels than for lower. The report serves mainly as a first investigation of the suitability of the method when it comes to practical measurements.

The comprehensive instrumentation of the plate shown in figure 5.4 is not necessary. In figure 5.4 the instrumentation is already simplified by use of symmetry arguments. As explained earlier, the shear stresses are greater on these axes where we can exploit symmetry in the x- and y-directions. Finite element analyses with a distributed pressure on the plate instead of a concentrated load have also been performed (not included in this report). They show the same shear stress distribution as the load case we have used here. The same advantage of symmetry and the same instrumentation can therefore also be used in the case of a distributed pressure. In addition to these symmetry simplifications we also have what we can call gradient simplifications. In section 6.1 shear stress values are calculated from all three measured gradients as well as from only the steepest (exact versus simplified values). We see that the difference are small and for most purposes acceptable. The author will therefore propose the very simple instrumentation shown in figure 7.1. By this instrumentation we only measure the steepest gradient for each of the points. If we want a more exact value we can also measure the perpendicular strains. These are still of minor importance both because they are multiplied with Poisson's ratio and because the gradient itself is smaller. The shear strains are so small that they need not be measure at all. The author concludes therefore that the instrumentation in figure 7.1 and equation (6.13) and (6.23) are accurate enough.

During this work the author has seen and experienced some practical weaknesses or challenges, mainly two, that will briefly be mentioned here. Firstly it is difficult to measure the steep strain gradients close to the frame accurate enough. It was in this area it was hardest to obtain accordance between measurements and model. An attempt to solve this problem is the

instrumentation in figure 7.1. By mounting strain gauges or Bragg gratings close to each other we can get an impression of the strain along the axes. Since the sensors require a certain distance to measure over, errors will always arise when the gradients become too steep over a short distance. However, the capability to measure steep gradients is much better for Bragg gratings. One can place them closer when they are on the same fibre, and they can be made shorter than strain gauges. Therefore Bragg gratings will be preferred for the instrumentation in figure 7.1 in future measurements.

The second weakness for the method is that first ply failure can occur, as explained in section 7.1. Fortunately the stress-strain curve for this type of incident is easy to recognise and a likely example is the curve of the first strain gauge in figure 5.11.

As stated in the beginning of this section this report serves mainly as a first investigation of the suitability of the method when it comes to practical measurements. At the very end of this report proposals for further work will therefore be given.

It would be interesting to test the method on more dynamic cases, where the frequencies reach the area for the resonance frequency of the plate. In real life, for instance a ship hull in sea, a great deal of the loads will have a dynamic nature. To test the method's suitability for these types of loads would be of great interest.

Secondly it would be of great value to fabricate a sandwich plate with a core fracture and see how shear stress distributions (and frequencies) change compared to a perfect plate. In this way we would gain knowledge on how strain gradients and shear stresses act in an already damage plate. For example, if we see that a gradient suddenly disappears over a distance we have reason to believe that the face acts like a free membrane uncoupled from the core in this area, and core fracture may have occurred. If we at the same time see that other strain sensors nearby the fracture area suddenly experience an increase in strain, it could mean that the shear forces have a smaller cross section to act on because of the fracture. It could also be interesting to run a destructive test on a perfect plate to see if we can create a shear fracture in the core, or if the plate is damaged in other ways before shear fracture occurs. Finally, an important test would be to measure on a naval ship with sandwich hull during operation to find the level of shear stress the wet deck experiences during heavy slamming in rough sea.

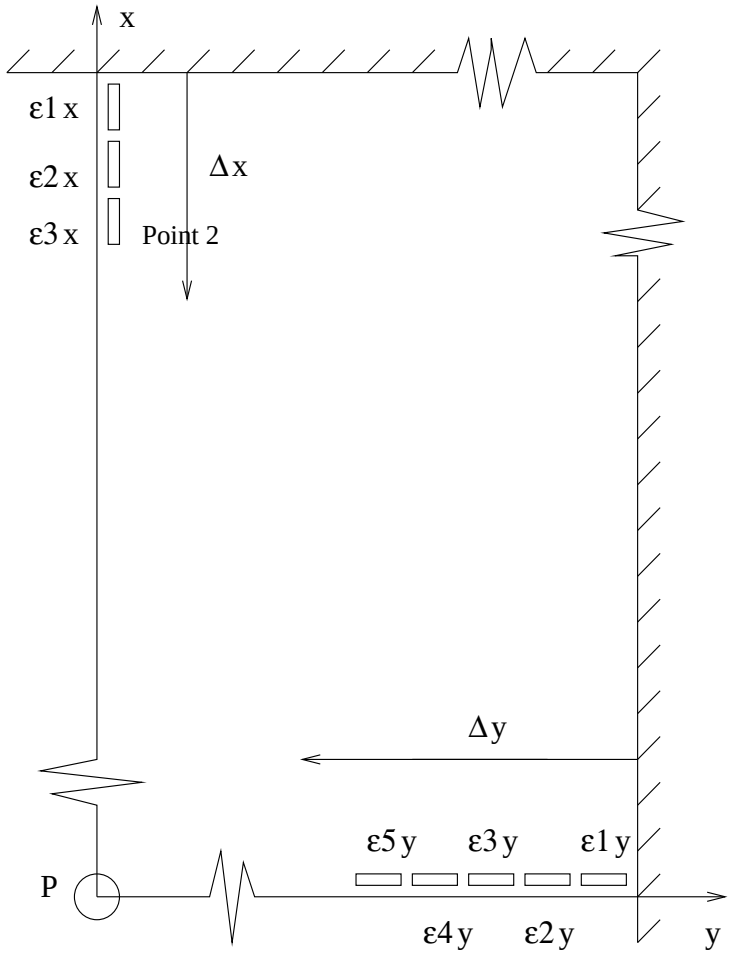

Figure 7.1 *Recommended number and position of strain gauges or Bragg gratings for shear stress determination.*

References

(1) Haugland S J (2000): *Theoretical Investigation of Strain Gradients for Transversal Shear Stress Determination in Fibre-Reinforced Sandwich-Panels,* (in Norwegian), Dept of Applied Mechanics, Norwegian University of Technology and Science (NTNU).

(2) Daniel I M, Ishai O (1994): *Engineering Mechanics of Composites Materials*, 1. ed, Oxford University Press, Oxford.

(3) Severinsen E (2000): *Strain Gradient Measurement Techniques for Sandwich Structures Using Fibre Optic Bragg Gratings*, FFI/Notat-2000/01046. Approved for public release. Distribution unlimited.

(4) Jensen A E et al (1999): *Design and Modelling of Sandwich Plate for Drop Test*, FFI/RAPPORT-99/04777. Approved for public release. Distribution unlimited.

(5) Pran K et al (1998): *Preliminary Static and Dynamic Tests on Sandwich Plate*, FFI/RAPPORT-98/02007. Approved for public release. Distribution unlimited.

(6) Pran K et al (1998): *Results of an Initial Sea-Test for the Composite Hull Embedded Sensor System (CHESS),* FFI/RAPPORT-98/05213. Approved for public release. Distribution unlimited.

(7) Pran K et al (1999): *Field Test with a Fibre Optic Sensor System on a Mine Counter-Measure Vessel*, FFI/RAPPORT-99/05425. Approved for public release. Distribution unlimited.

(8) Pran K et al (2000): *A Summary of Project 711 "Fiberoptisk Skrogovervåkning" (CHESS),* FFI/RAPPORT-2000/01298. Approved for public release. Distribution unlimited.

(9) Irgens F (1997): *Kontinuumsmekanikk, kompendium*, Dept of Applied Mechanics, NTNU.

(10) Timoshenko S P, Woinowsky-Krieger S (1959): *Theory of Plates and Shells*, 2. ed, McGraw-Hill.

(11) Jensen A E (1997): *Determination of Transversal Shear Stress from Strain Gradient Measurements on a GRP Sandwich Beam*, Institute note, Dept of Applied Mechanics, NTNU.

(12) Irgens F (1992): *Formelsamling Mekanikk*, Tapir Forlag, Trondheim.

(13) Leissa A W (1969): *Vibration of Plates*, NASA SP-160, NASA, Washington D.C.

(14) Vaughan J (1975): *Application of B K Equipment to Strain Measurements*, Bruel and Kjær.

(15) Davies P (1996): Test report EUCLID RTP3.8, IFREMER, *FRP Sandwich Panels under Static Pressure.* TD-12341-9602 Rev. 2.

(16) Hayman B, Wiese M, Skeie G (1999): Test report EUCLID RTP 3.8, Det Norske

Veritas, *FRP Sandwich Panels with Static Loading - a computational study*, 98-2016 TD-12441-9802.

(17) Høyning B (1998): Test report EUCLID RTP 3.8, FiReCo, *FEM-analysis of static pressure loaded FRP Sandwich Panels - comparison with tests*, TD-12441 Rev 0.

(18) Mitusch P (1997): Test report EUCLID RTP 3.8, FFI, *Analysis of Sandwich Panels with Stastic Pressure Loading*, TD-12441-9701 Rev 0.

APPENDIX

A LIST OF SYMBOLS

A_c	core cross section area
a, b	length of plate in x- and y-direction, respectively
b	beam width
c	core thickness
D	flexural rigidity
D_{ij}	plate stiffnesses
d	average thickness; geometrical path imbalance
E	Young's modulus (=Elasticity modulus); excitation voltage
E_c	Young's modulus, core
E_f	Young's modulus, faces
f	frequency
G	shear modulus
h	plate thickness
I	moment of inertia, second moment of area
i, j, k	indices, possible values 1, 2, 3
k	gauge factor
L, l	length
M	moment
n	effective fibre refractive index
P	concentrated load
p_e	effective photoelastic constant
Q_α	shear forces (plate)
$R, \partial R$	resistance; change in resistance
$r_{ij}, 1/r_{ij}$	radii of curvature, curvatures
S	first moment of inertia
t	face thickness; time
u, v, w	displacement in x-, y- and z-direction
V	shear force (beam); bridge voltage
α, β	indices, possible values 1, 2
$\Delta\phi$	phase change
δ	deflection of plate centre
ε	(normal)strains
γ	shear strains
φ	angle of rotation
$\lambda_b, \Delta\lambda_b$	Bragg grating wavelength; change in Bragg grating wavelength
ν	Poisson's ratio
ν_c	Poisson's ratio, core
ν_f	Poisson's ratio, faces
ρ	density
σ	(normal)stresses
σ_j	von Mises stress, effective stress, equivalent stress

τ	shear stresses
c	superscript denoting a value related to the core
s	subscript denoting that a laminate has a symmetric lay-up

B MATERIAL PROPERTIES FOR THE SANDWICH PLATE

In this appendix Young's moduli, Poisson's ratios and plate stiffnesses for the experimental method from section 2.5 will be calculated in detail. The expressions are given in equation (2.42)-(2.44) and will be repeated here:

$$D_x = \frac{E_{fx}h^3}{12(1-v_{fxy}^2)} - \frac{E_{fx}c^3}{12(1-v_{fxy}^2)} + \frac{E_c c^3}{12(1-v_c^2)} \tag{B.1}$$

$$D_y = \frac{E_{fy}h^3}{12(1-v_{fyx}^2)} - \frac{E_{fy}c^3}{12(1-v_{fyx}^2)} + \frac{E_c c^3}{12(1-v_c^2)} \tag{B.2}$$

$$D_{xy} = \frac{G_{fxy}h^3}{24} - \frac{G_{fxy}c^3}{24} + \frac{E_c c^3}{48(1+v_c)} \tag{B.3}$$

We have the following values for our plate:

Plate thickness: h = 29 mm
Core thickness: c = 25 mm
Face thickness: t = 2 mm

Young's modulus, core: E_c = 0,22 GPa
Poisson's ratio, core: ν_c = 0,33

E_c and ν_c are taken from (17) and can also be obtained from the supplier.

To obtain the material constants for the faces in equation (B.1)-(B.3) the program LAMPROG.xls designed by Nils Petter Vedvik, Dept of Machine Design and Materials Technology at NTNU, has been used. For each layer in the two faces we give orientation, thickness and material properties along and transverse of the fibre direction. The material properties are taken from table 4.1. The output from the program is the global material properties in x- and y-direction that we need in equation (B.1)-(B.3). In the calculations the two faces are treated as one laminate, but the changes in the output values are insignificant if we only consider one face. We obtain:

Young's moduli, faces: E_{fx} = 8,75 GPa
E_{fy} = 13,36 GPa
Shear modulus, faces: G_{fxy} = 5,50 GPa
Poisson's ratios, faces: ν_{fxy} = 0,32
ν_{fyx} = 0,49

We are now ready to calculate the plate stiffnesses. We insert the above values in the expressions and get:

$$D_x = \left[\frac{(8{,}75 \cdot 10^3)29^3}{12(1-0{,}32^2)} - \frac{(8{,}75 \cdot 10^3)25^3}{12(1-0{,}32^2)} + \frac{(0{,}22 \cdot 10^3)25^3}{12(1-0{,}33^2)} \right] \frac{N \cdot mm^3}{mm^2} = \underline{7{,}44 \cdot 10^6 \, Nmm} \tag{B.4}$$

$$D_y = \left[\frac{(13{,}36 \cdot 10^3)29^3}{12(1-0{,}49^2)} - \frac{(13{,}36 \cdot 10^3)25^3}{12(1-0{,}49^2)} + \frac{(0{,}22 \cdot 10^3)25^3}{12(1-0{,}33^2)} \right] \frac{N \cdot mm^3}{mm^2} = \underline{13{,}16 \cdot 10^6 \, Nmm} \tag{B.5}$$

$$D_{xy} = \left[\frac{(5{,}5 \cdot 10^3)29^3}{24} - \frac{(5{,}5 \cdot 10^3)25^3}{24} + \frac{(0{,}22 \cdot 10^3)25^3}{48(1+0{,}33)} \right] \frac{N \cdot mm^3}{mm^2} = \underline{2{,}06 \cdot 10^6 \, Nmm} \tag{B.6}$$

These values are used in the calculations in chapter 6.

C CONTOUR PLOTS FROM FEM SIMULATIONS

This appendix gives a few examples of the contour plots from the FEM-model of the plate. The load case is the fully clamped plate with a concentrated load in centre. The plots are not used in further calculations because they are too inaccurate. They are still included in the report to visualise some strain- and shear stress distributions. The plots are only for the case 5000 N. The first two figures show the element mesh for the plate. The mesh is finest at the clamping where the strain gradients are steepest.

In figure C.3 the plot shows the strain in the global *y*-direction. The figure says strain in *x*-direction, but the reason is that the local coordinate system for the elements in the FEM-model is defined different than our global coordinate system, shown for instance in figure 5.3.

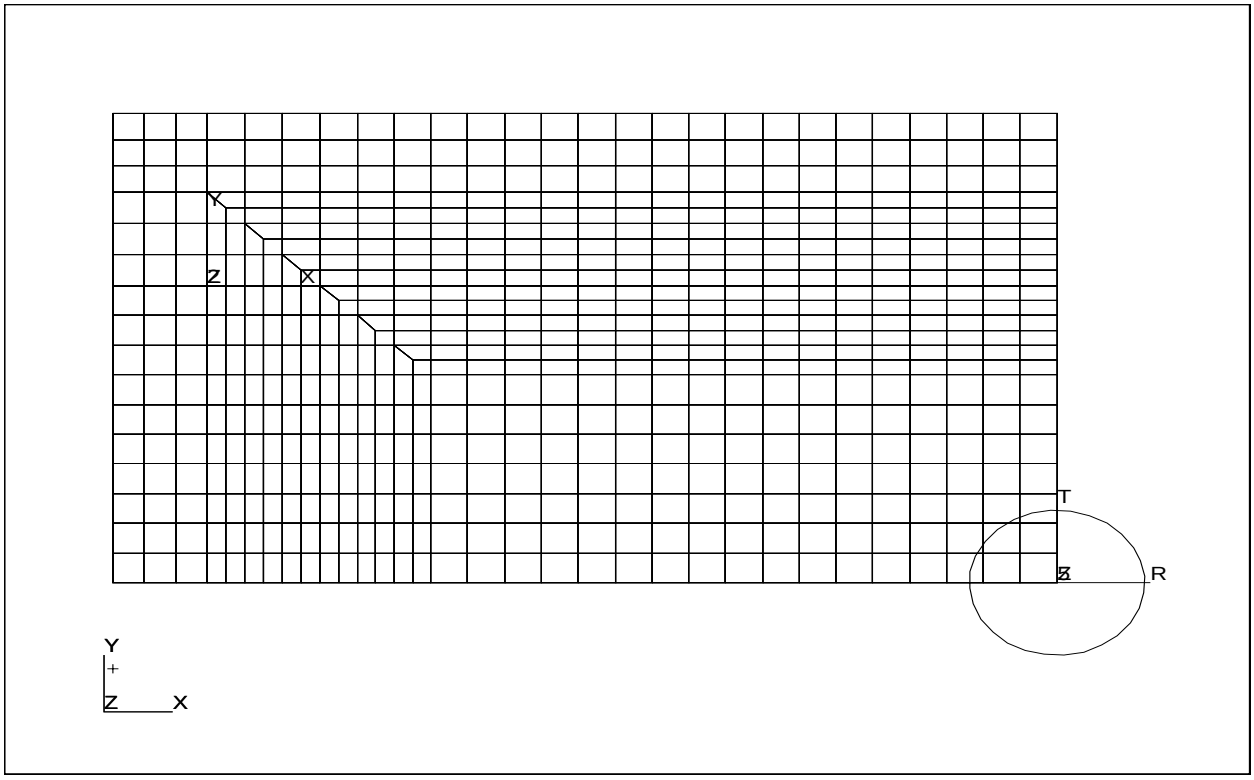

Figure C.1 Element mesh of the quarter plate.

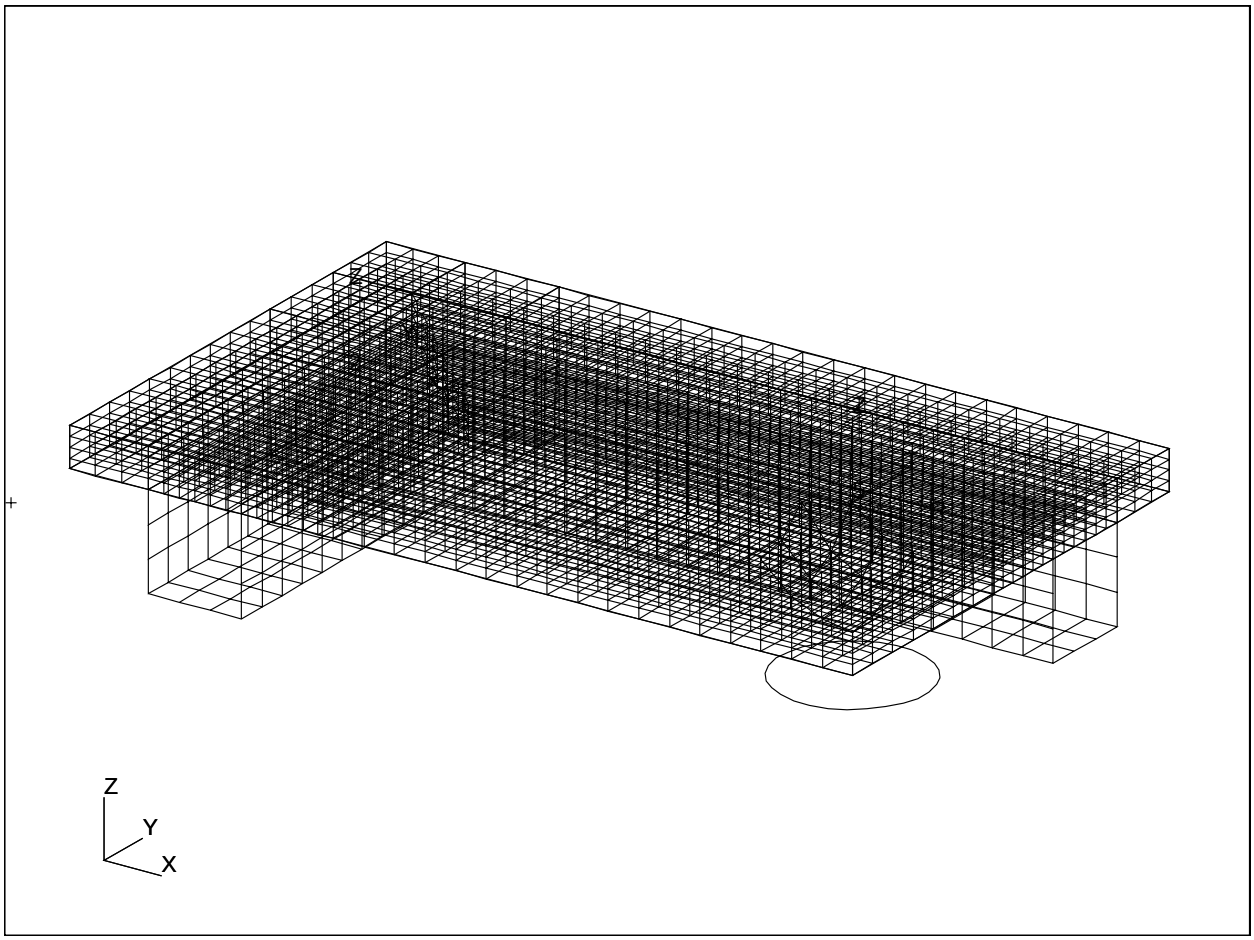

Figure C.2 Element mesh of the quarter sandwich plate and frame.

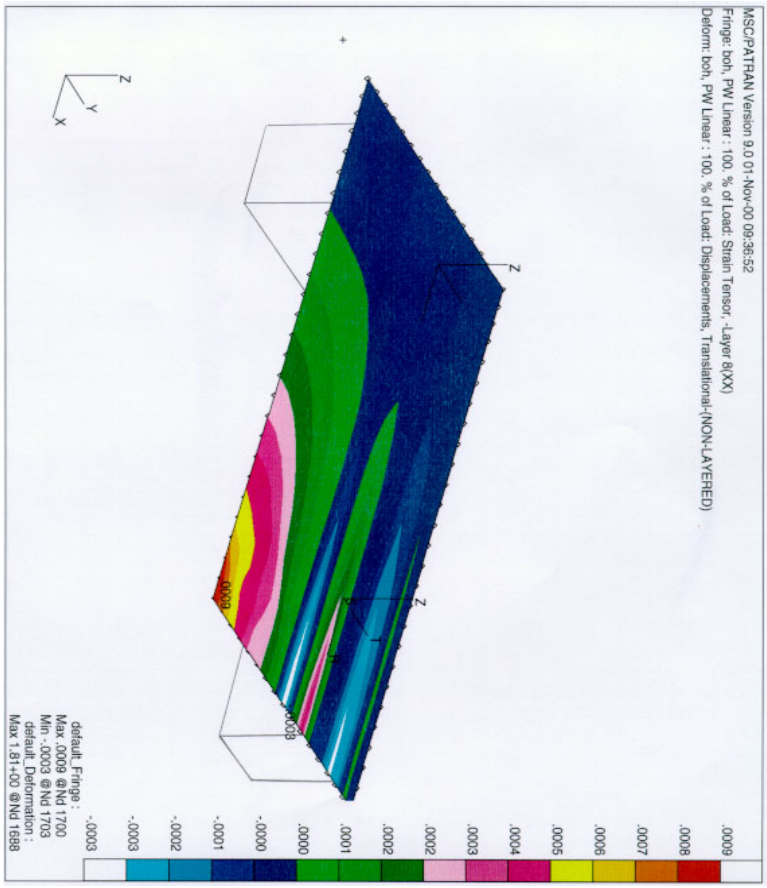

Figure C.3 Strain ε_y in the surface layer (layer 8) in the bottom face.

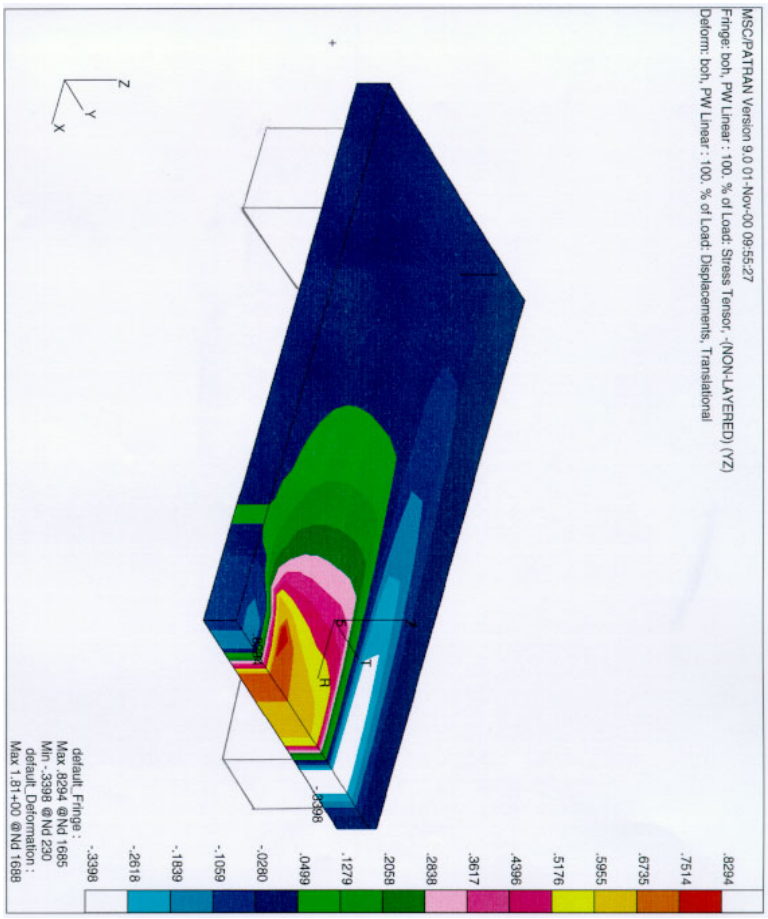

Figure C.4 Stress τ_{yz} in the core material.

D XY-PLOTS OF STRAINS AND SHEAR STRESSES ALONG THE PLATE AXES

This appendix contains the plots of the strains and shear stresses along the plate axes, i.e. the *x*- and *y*-axis in figure 5.3. All strain plots are in the CSM surface layer (layer 8) in the bottom face. All stress plots are for the core. The plots are used to decide the distances when calculating the gradients in equation (2.48)-(2.53), and to compare the experimental and simulated results. The strain values are drawn (by hand) in the figures for the positions of all strain gauges in order to compare them with the experimental values.
The plots must be as linear as possible in the area where we want to find the gradients. The gradients and distances are therefore drawn in the plots (also by hand) trying to keep them in a fairly linear area. In section 5.3 the distances are given and used in further calculations. Calculated and simulated strains and shear stresses are compared in section 5.7 and 6.3, respectively.
The shaded “column” in the figures represents the position of the frame.

All stresses have unit [MPa].

D.1 Stress and strain for load 5000 N

D.1.1 Plots along the *y*-axis of the plate (Point 1)

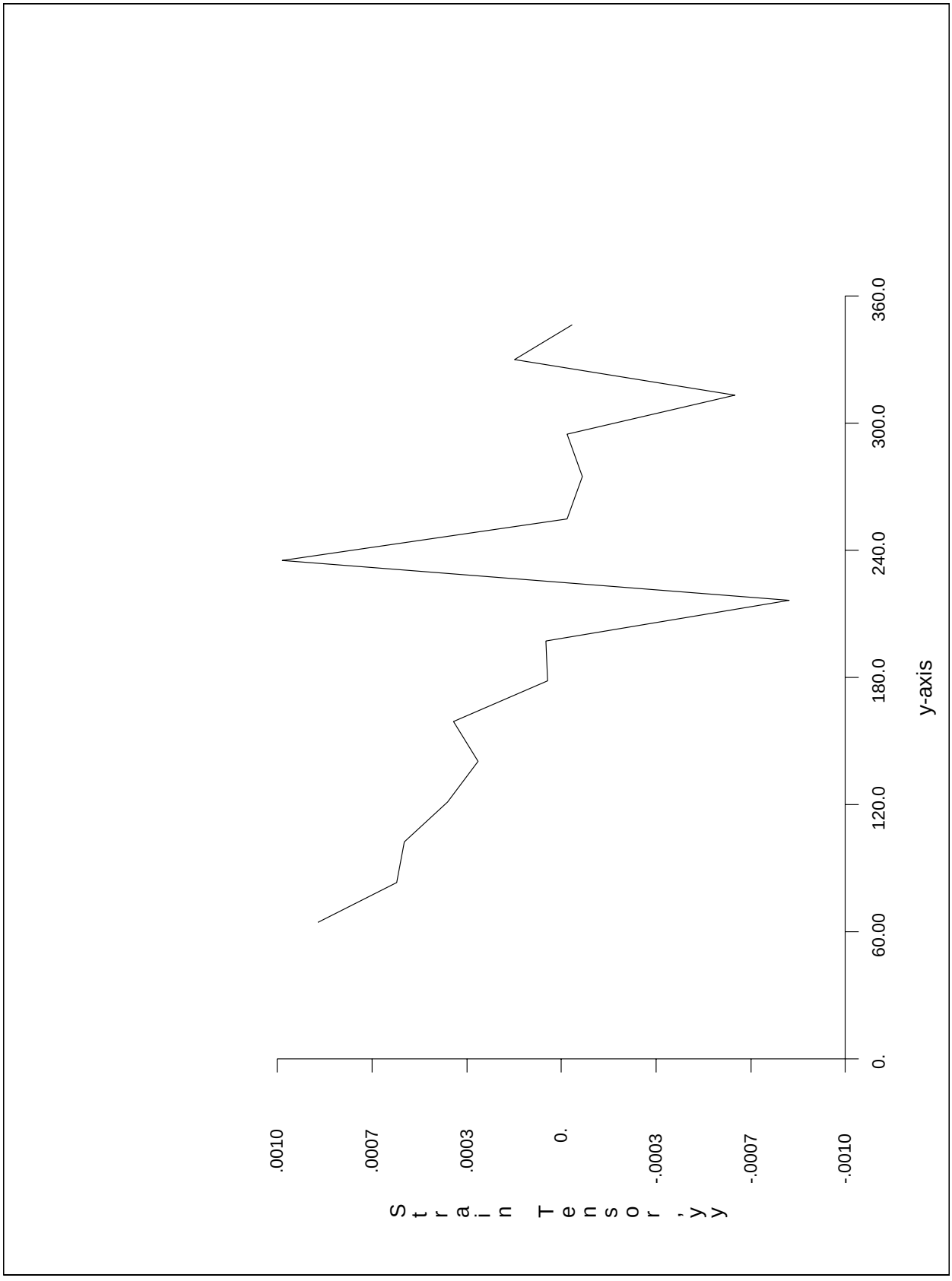

Figure D.1 Strain ε_{yy}, y-axis, 5000 N.

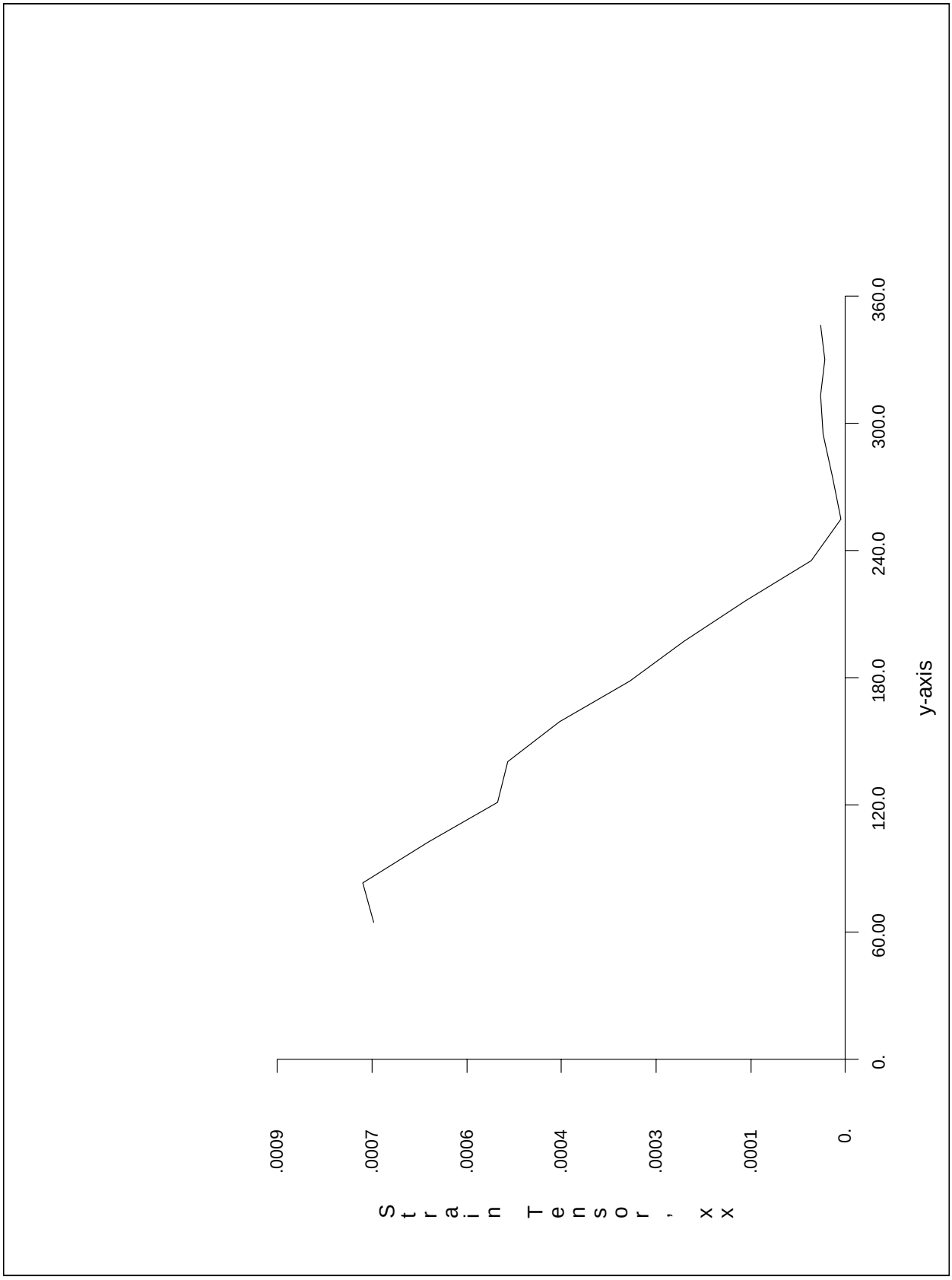

Figure D.2 Strain ε_{xx}, y-axis, 5000 N.

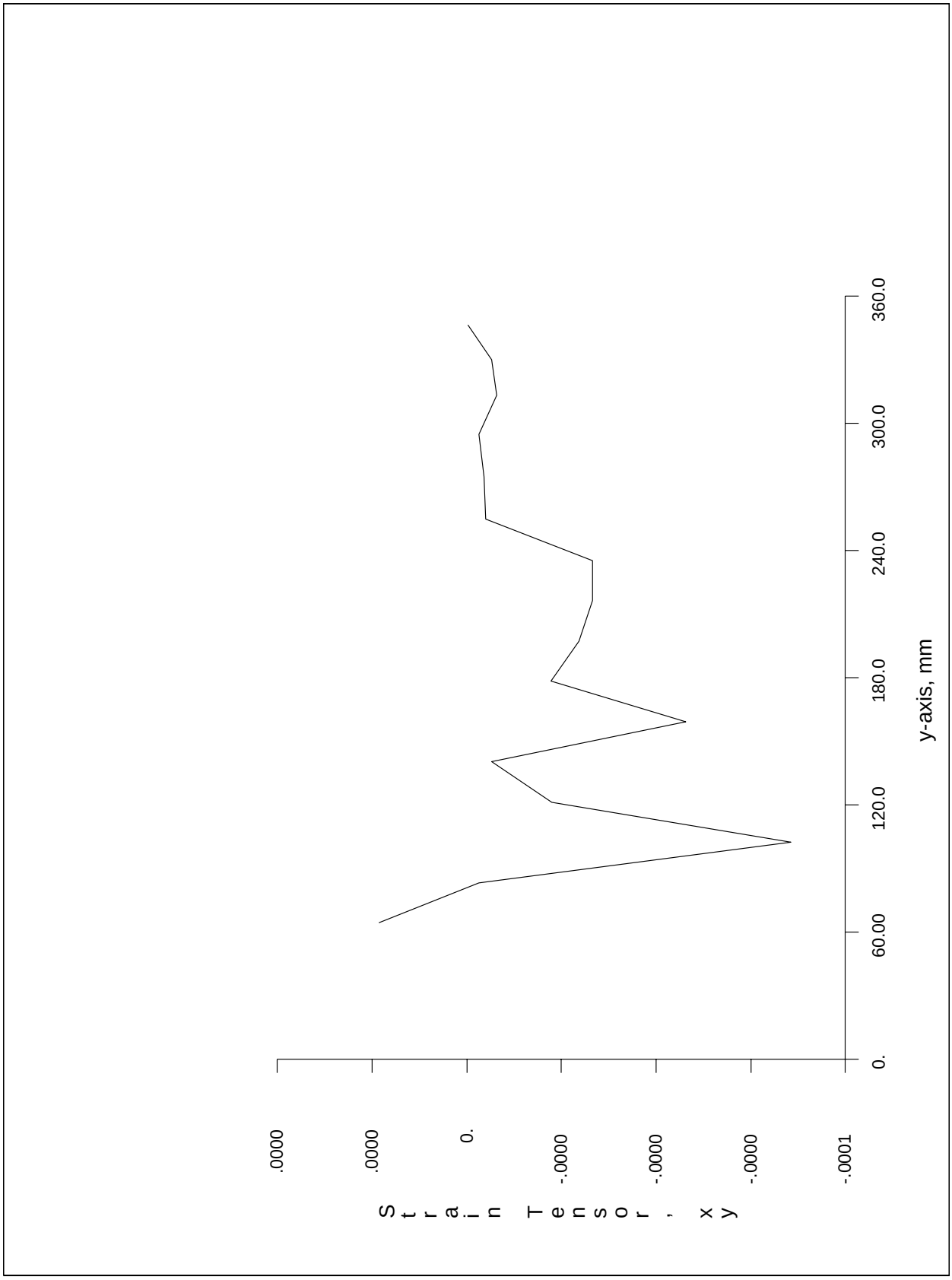

Figure D.3 Strain γ_{xy}, y-axis, 5000 N.

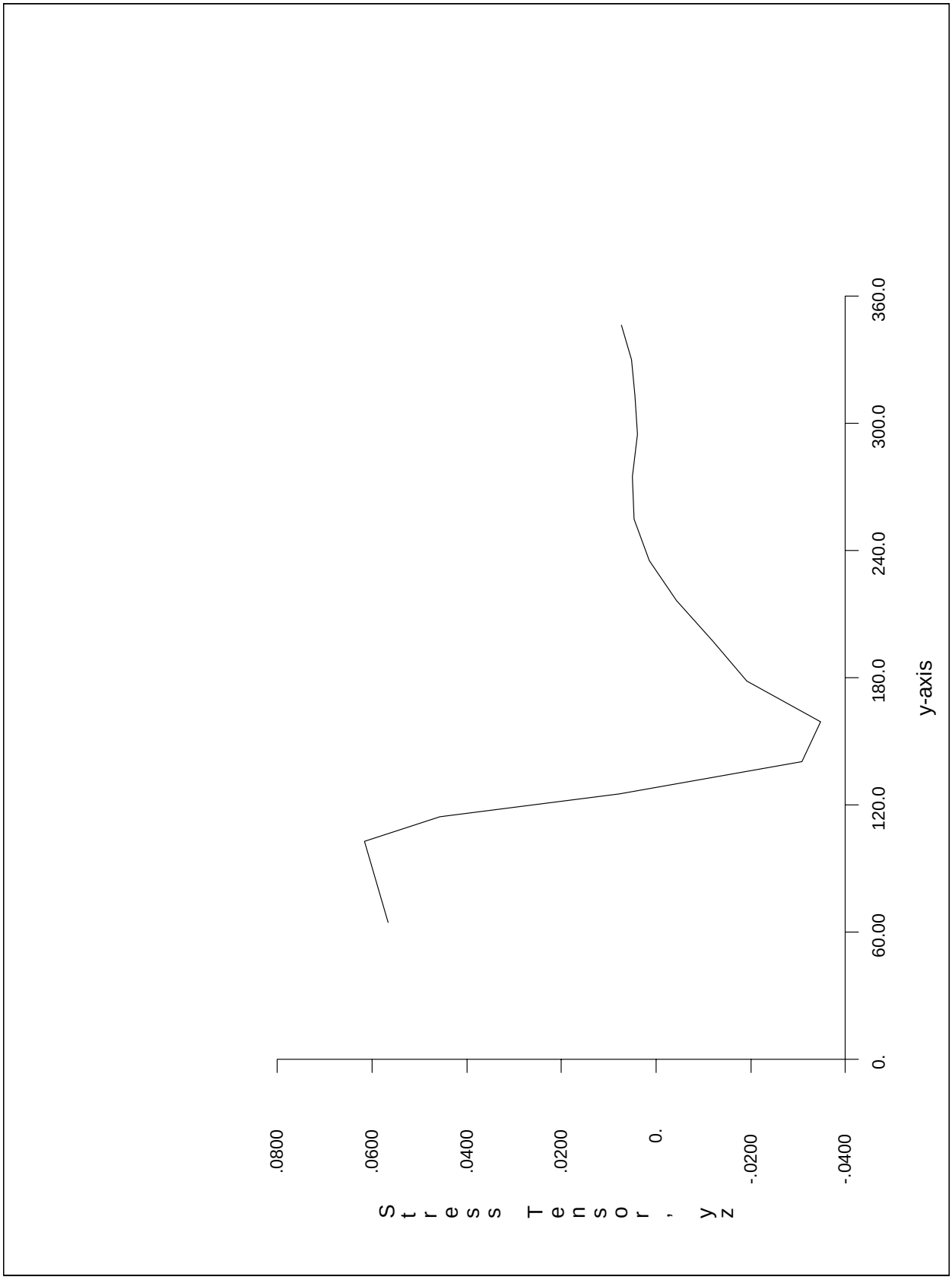

Figure D.4 Stress τ_{xz}, y-axis, 5000 N.

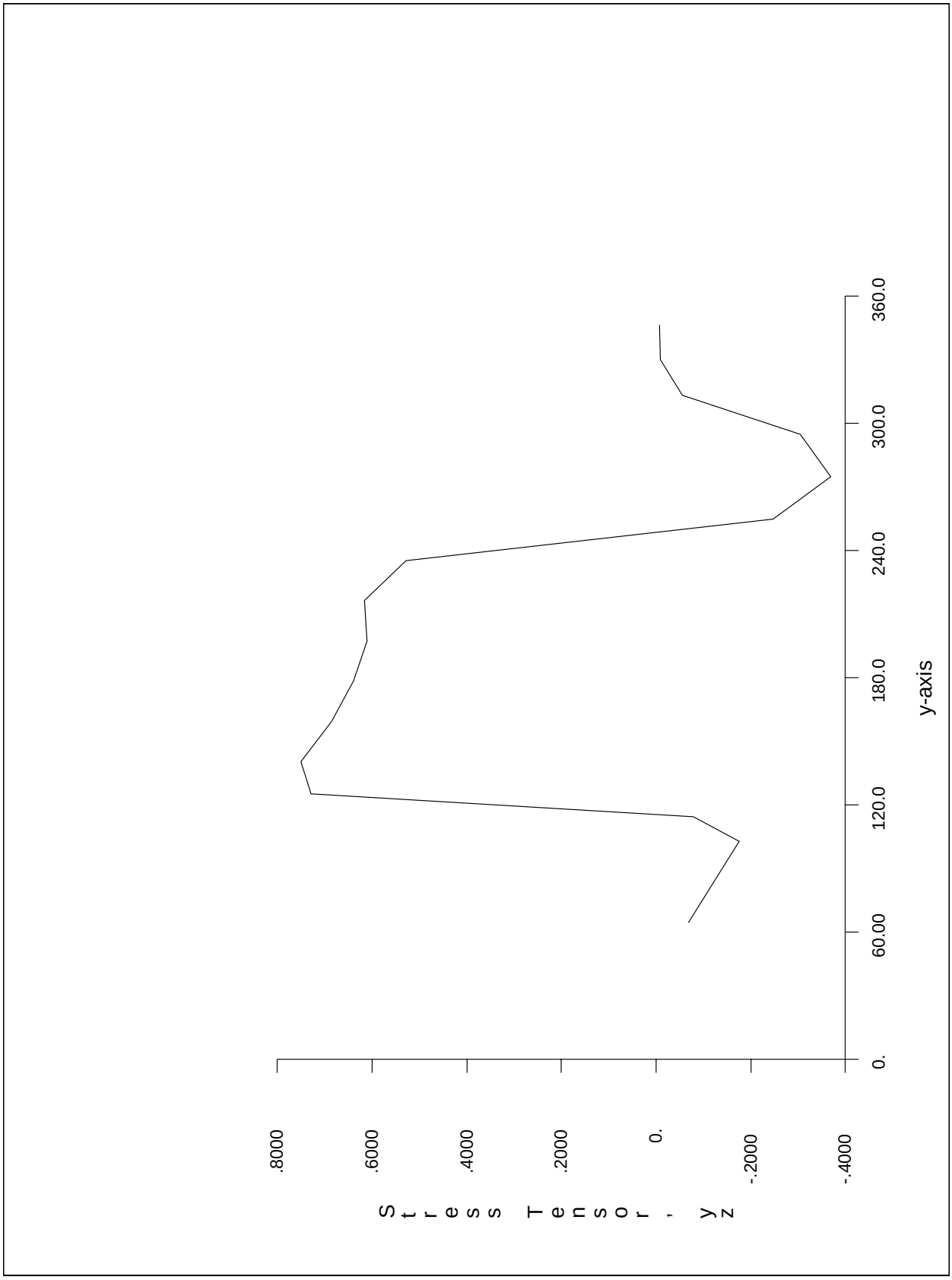

Figure D.5 Stress τ_{yz}, y-axis, 5000 N.

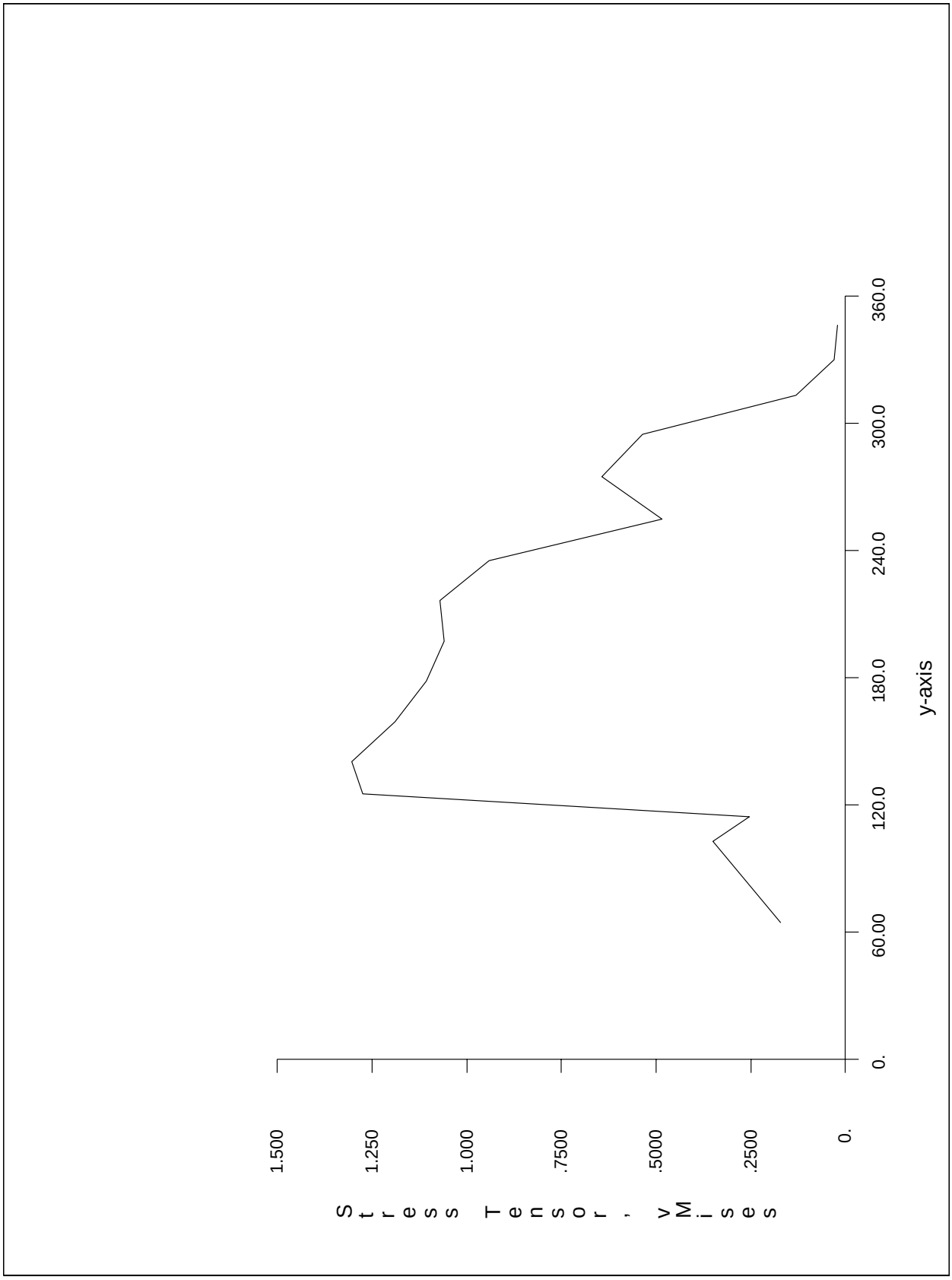

Figure D.6 Von Mises stress, y-axis, 5000 N.

D.1.2 Plots along the *x*-axis of the plate (Point 2)

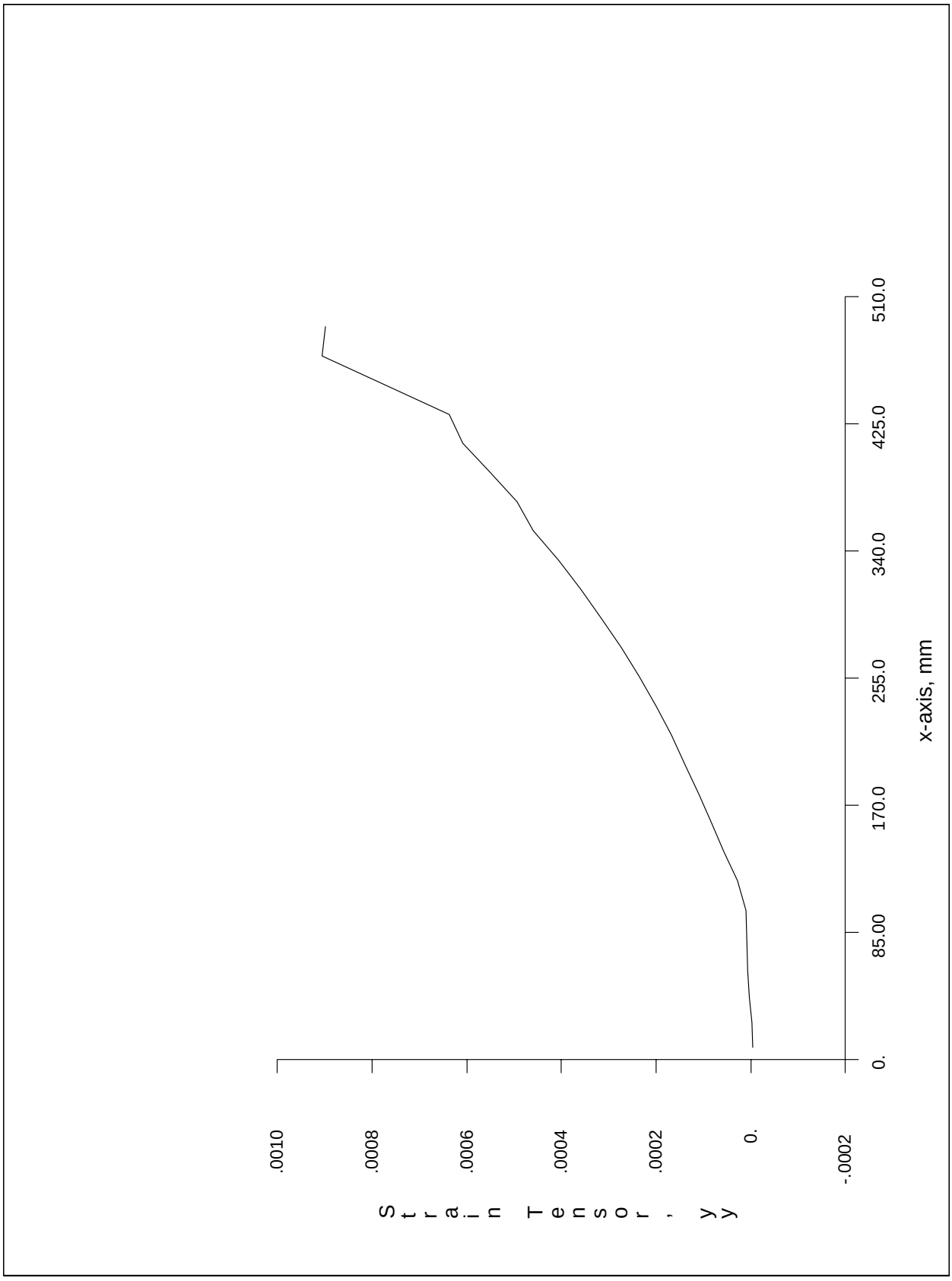

Figure D.7 Strain ε_{yy}, x-axis, 5000 N.

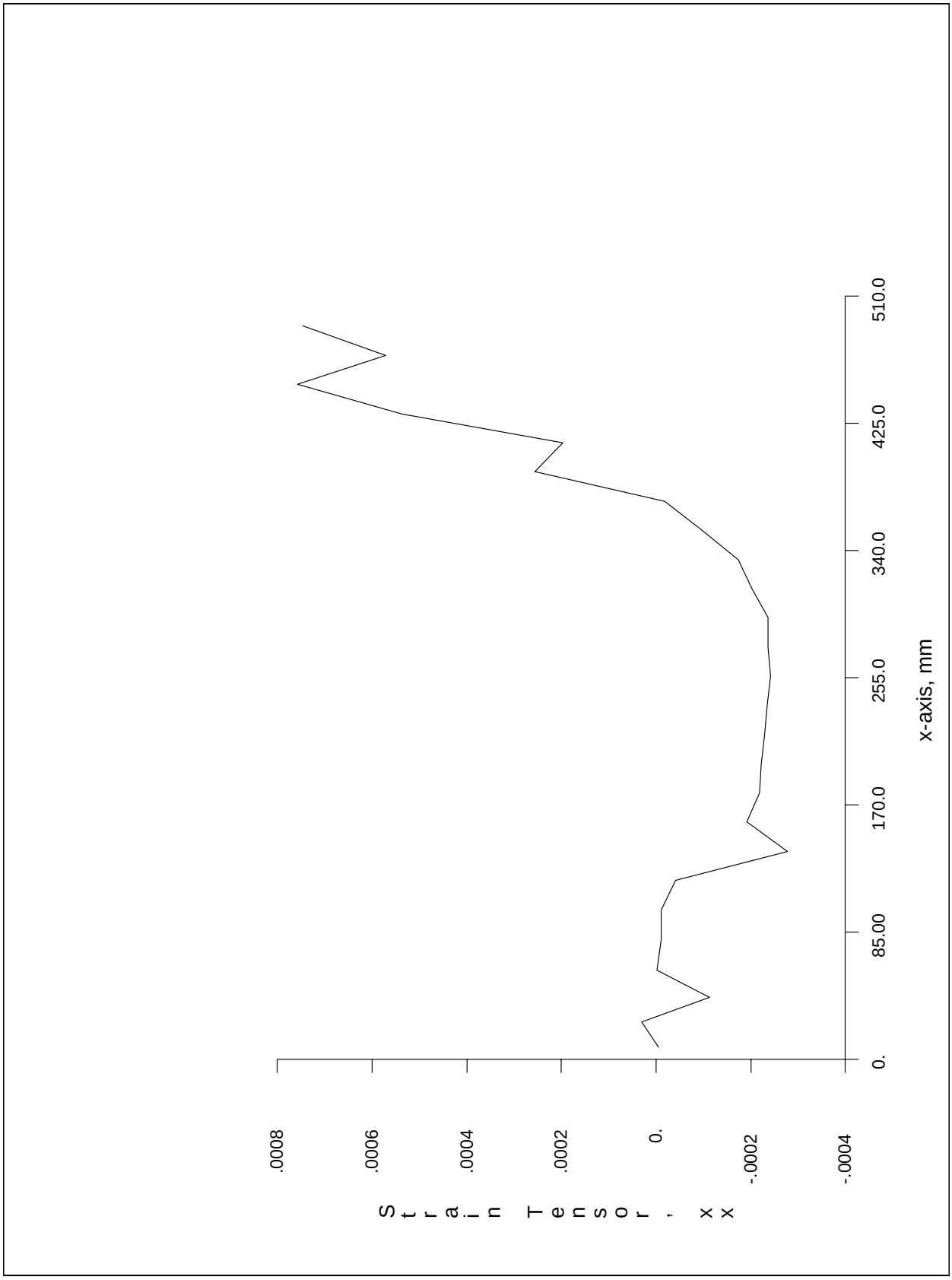

Figure D.8 Strain ε_{xx}, x-axis, 5000 N.

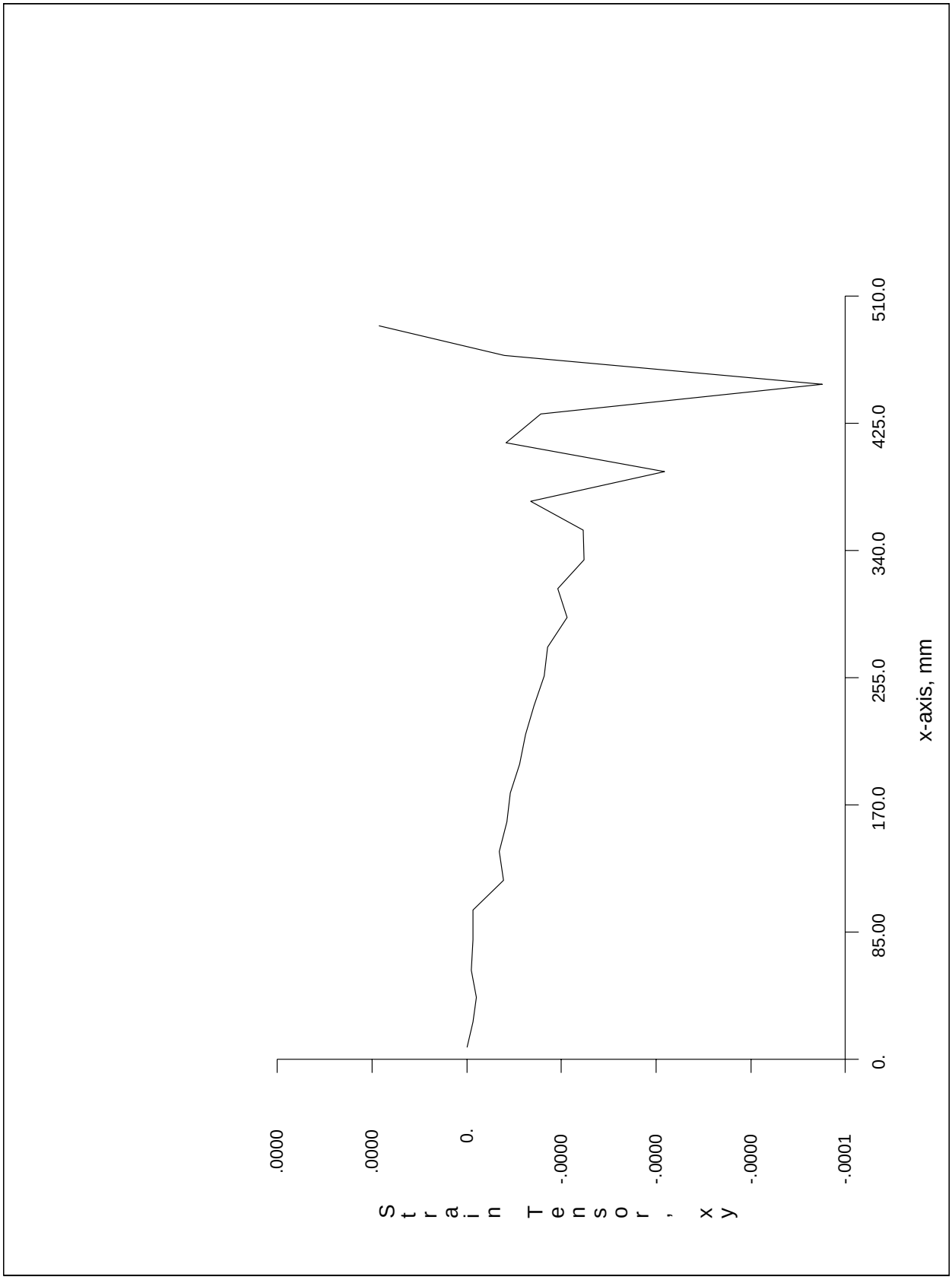

Figure D.9 Strain γ_{xy}, x-axis, 5000 N.

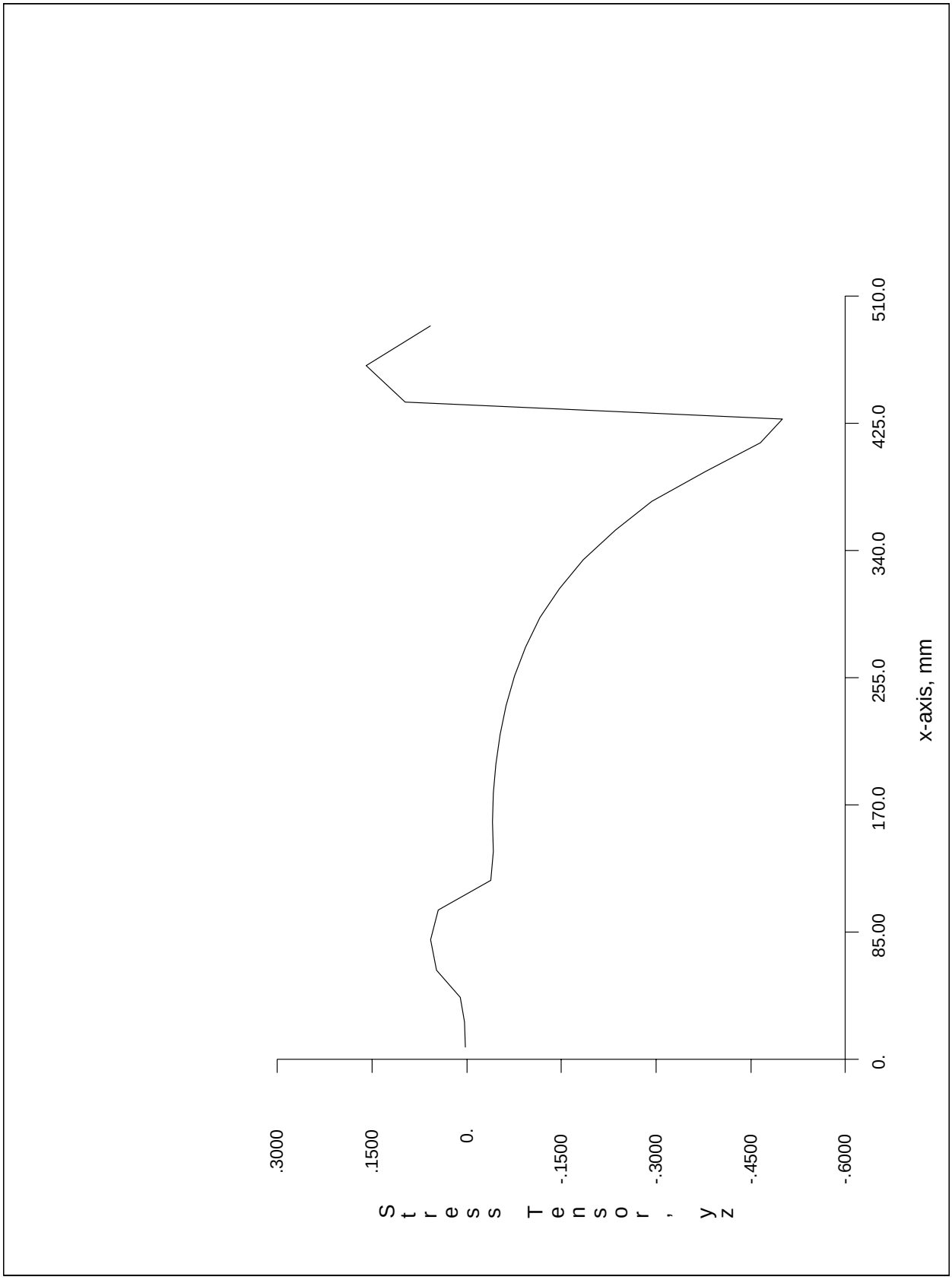

Figure D.10 Stress τ_{xz}, x-axis, 5000 N.

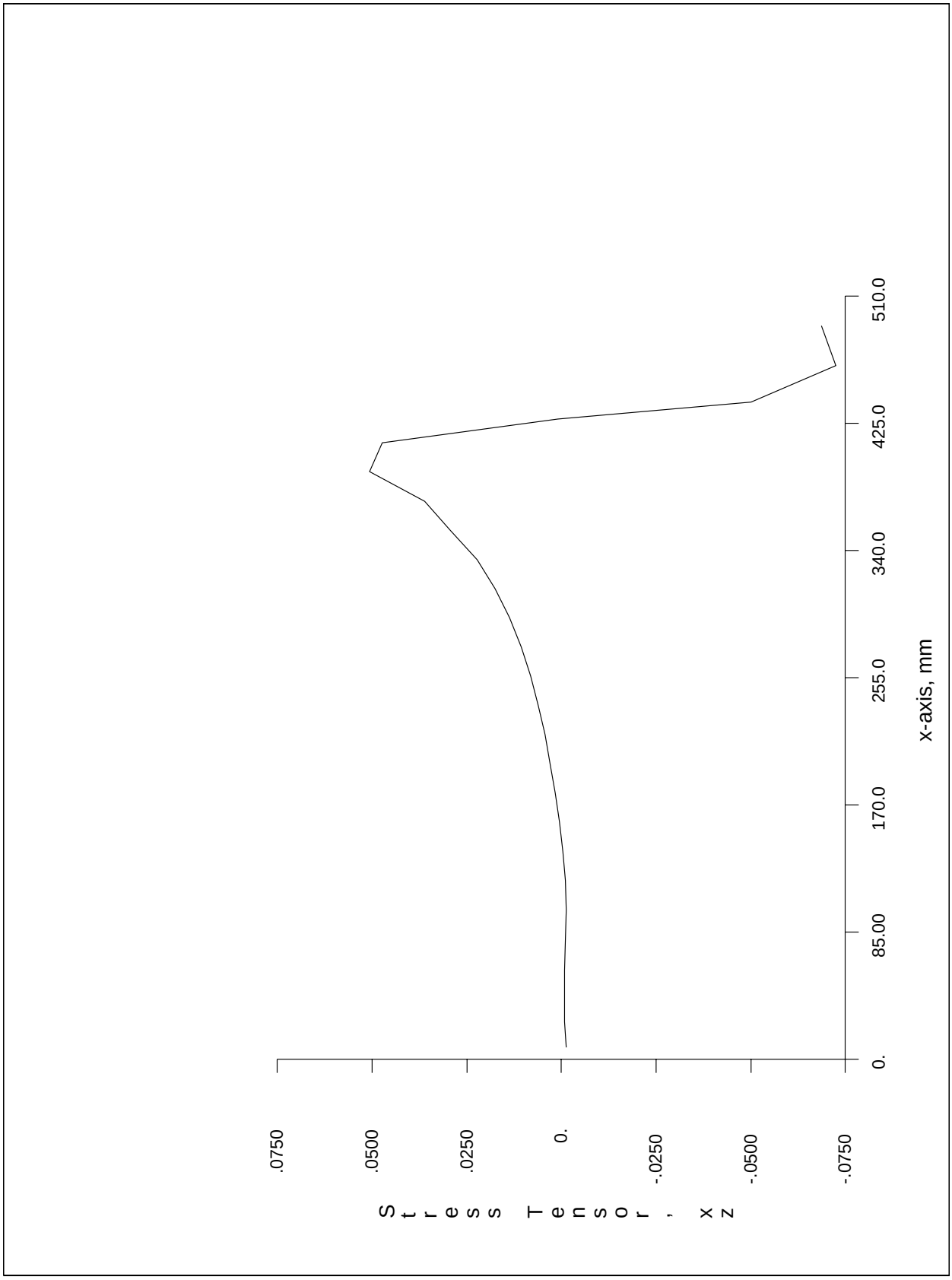

Figure D.11 Stress τ_{yz}, x-axis, 5000 N.

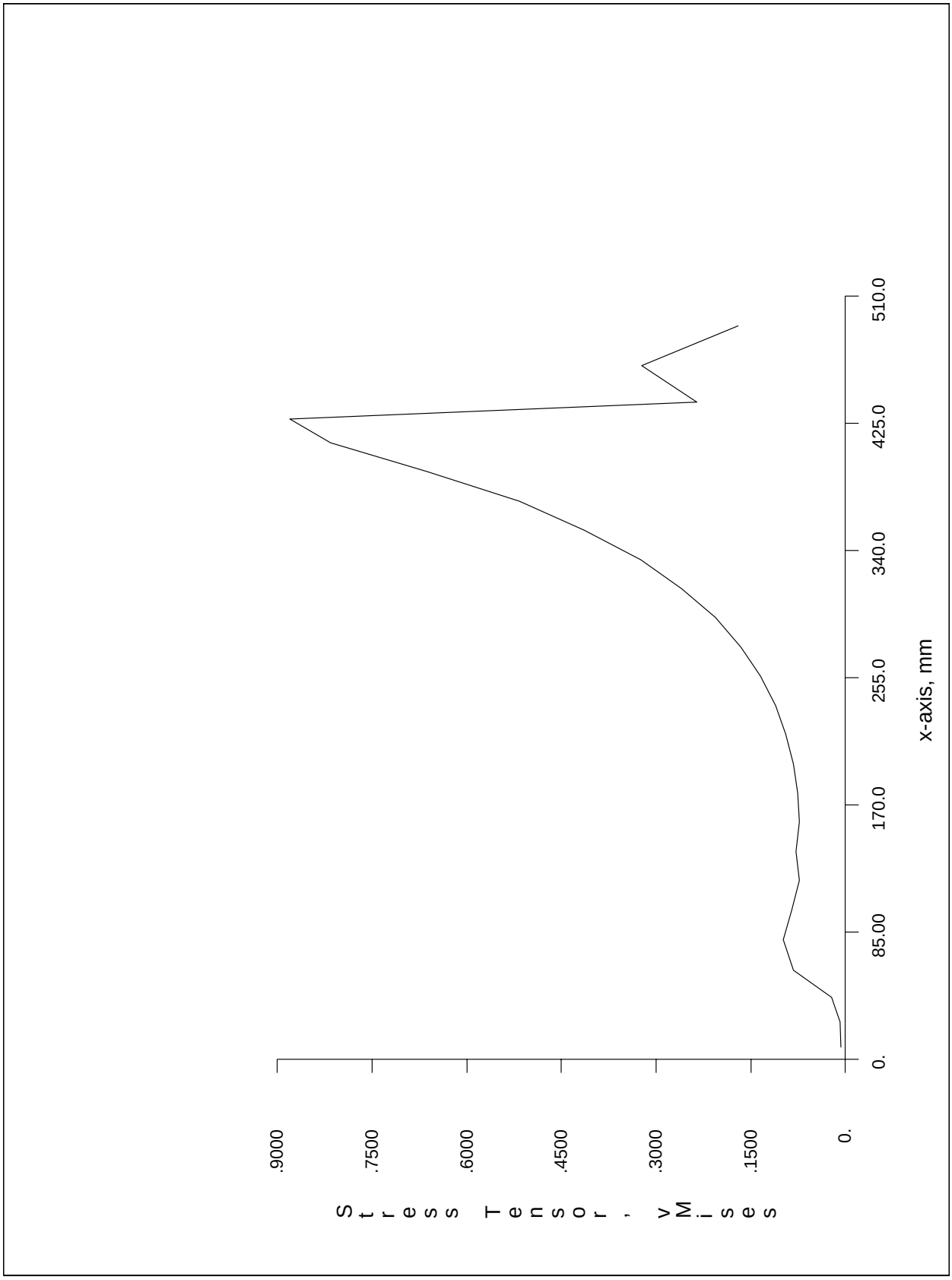

Figure D.12 Von Mises stress, y-axis, 5000 N.

D.2 Stress and strain for load 10000 N

D.2.1 Plots along the *y*-axis of the plate (Point 1)

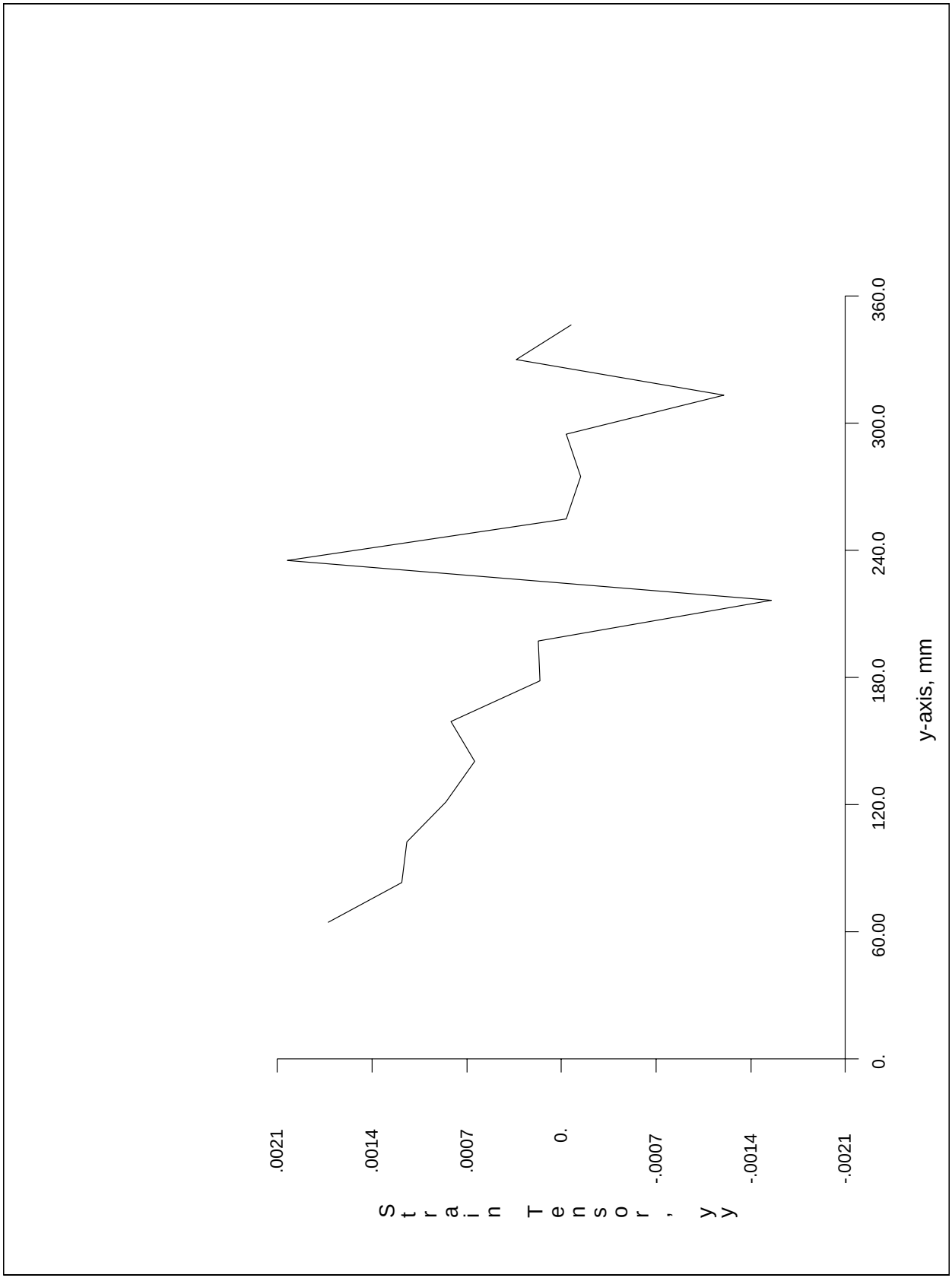

Figure D.13 Strain ε_{yy}, y-axis, 10000 N.

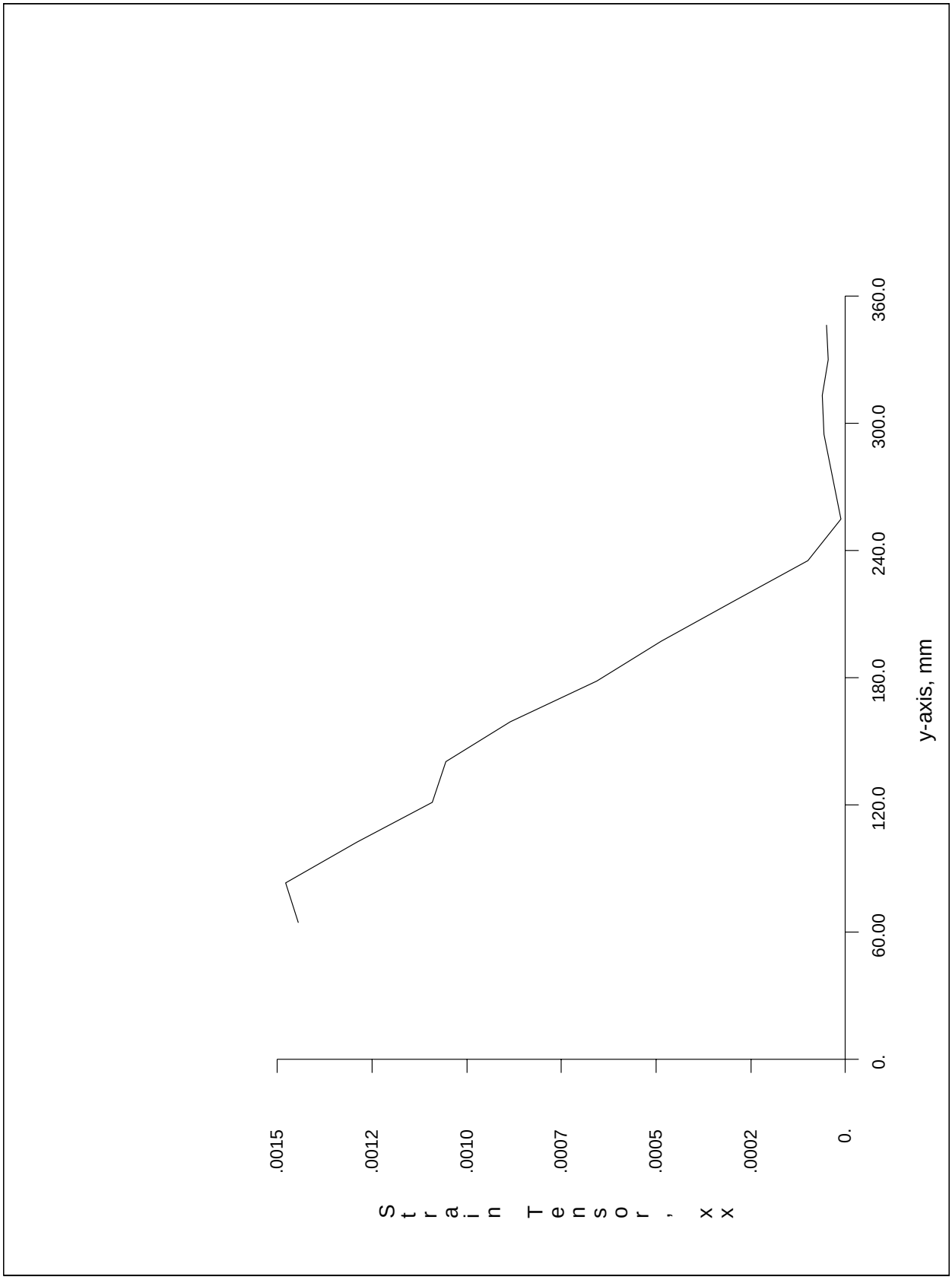

Figure D.14 Strain ε_{xx}, y-axis, 10000 N.

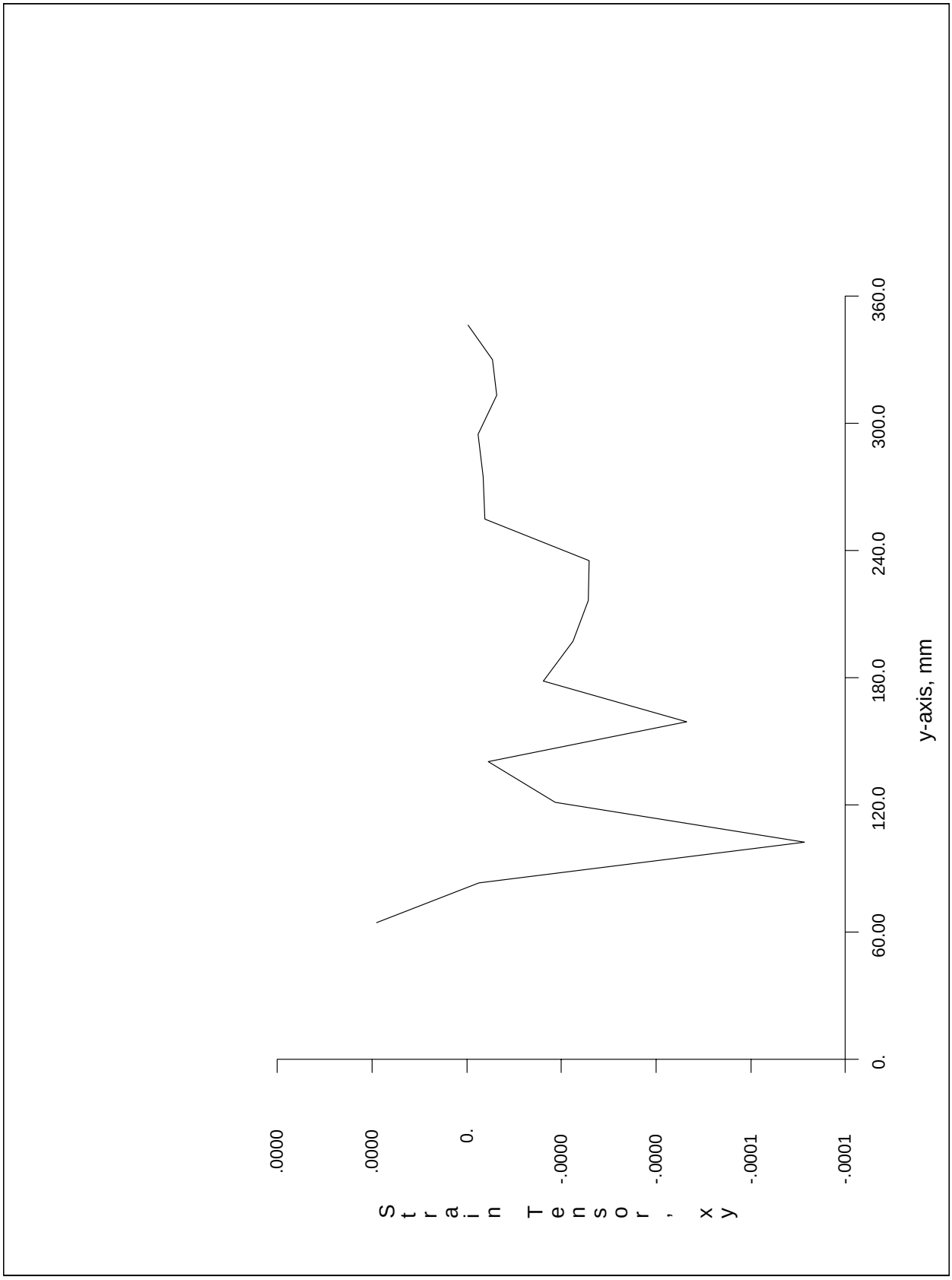

Figure D.15 Strain γ_{xy}, y-axis, 10000 N.

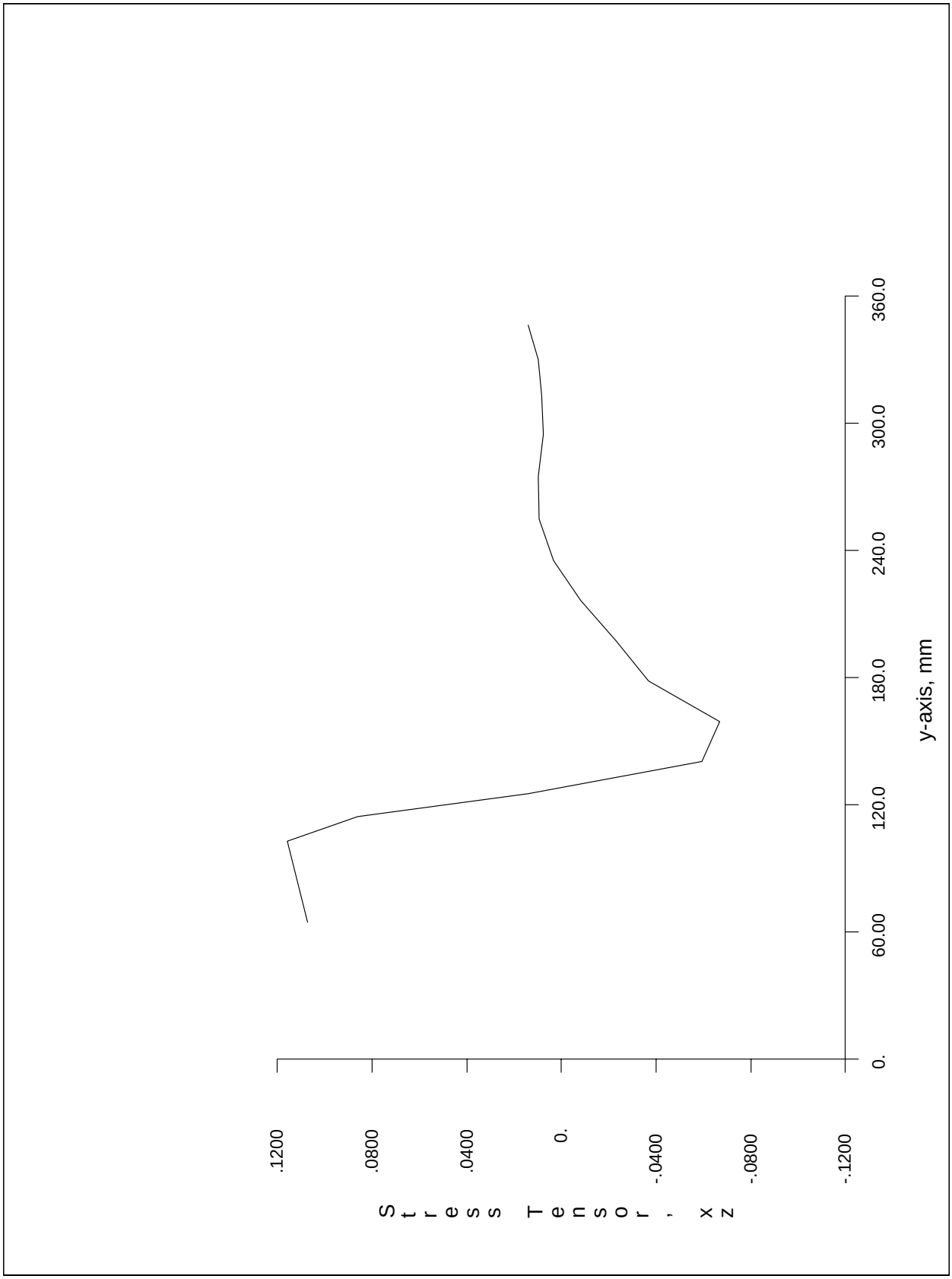

Figure D.16 Stress τ_{xz}, y-axis, 10000 N.

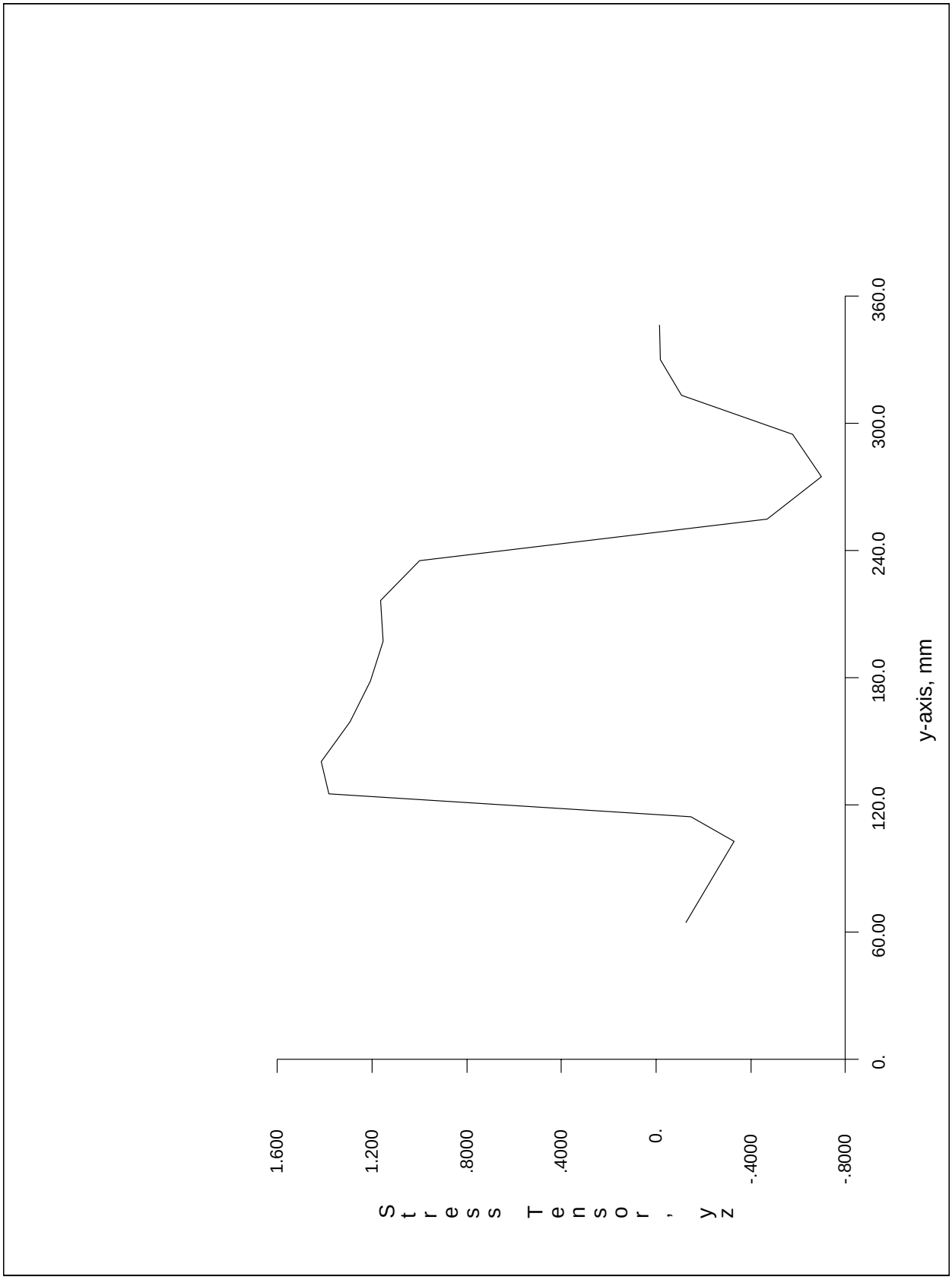

Figure D.17 Stress τ_{yz}, y-axis, 10000 N.

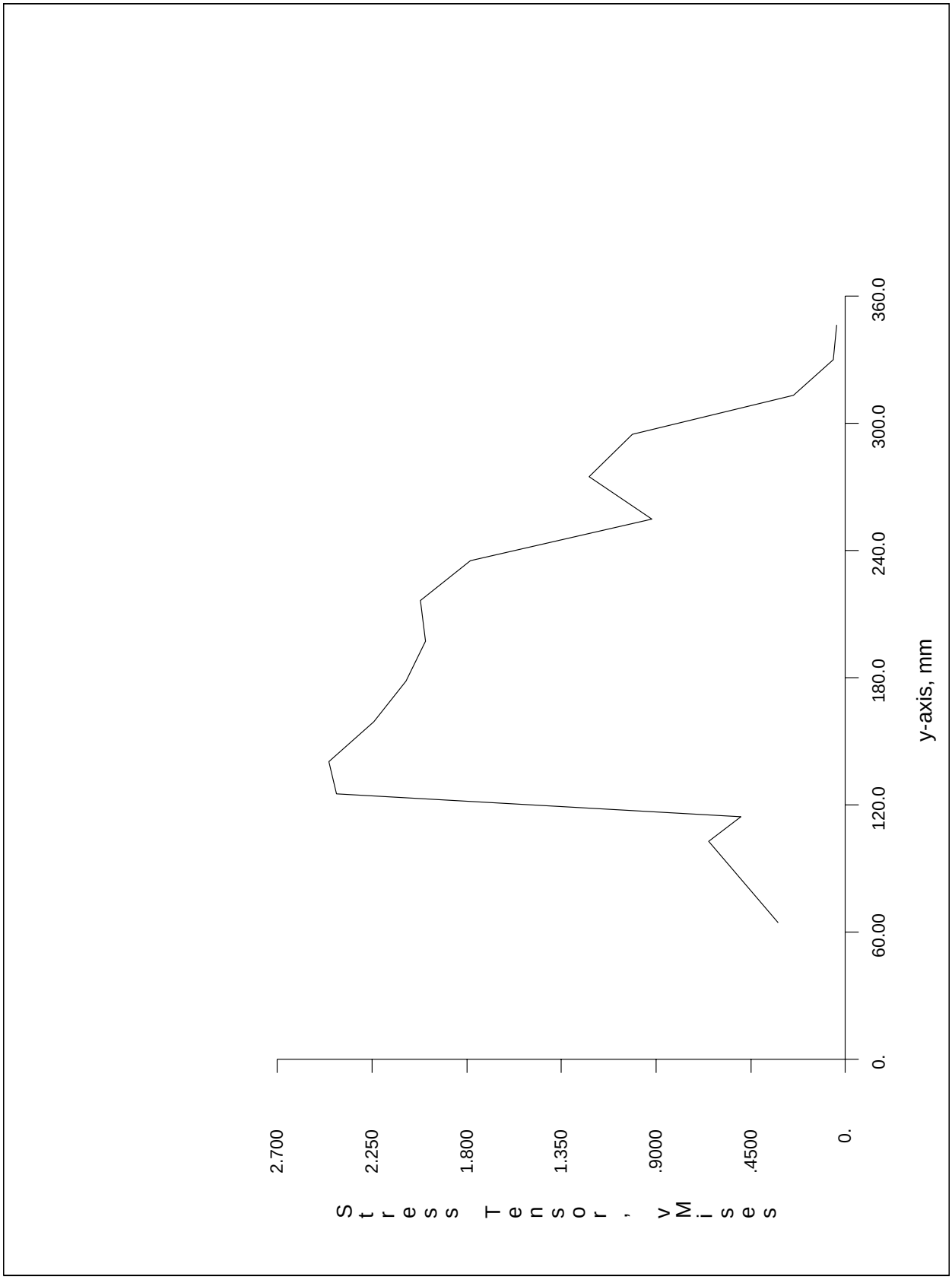

Figure D.18 Von Mises stress, y-axis, 10000 N.

D.2.2 Plots along the *x*-axis of the plate (Point 2)

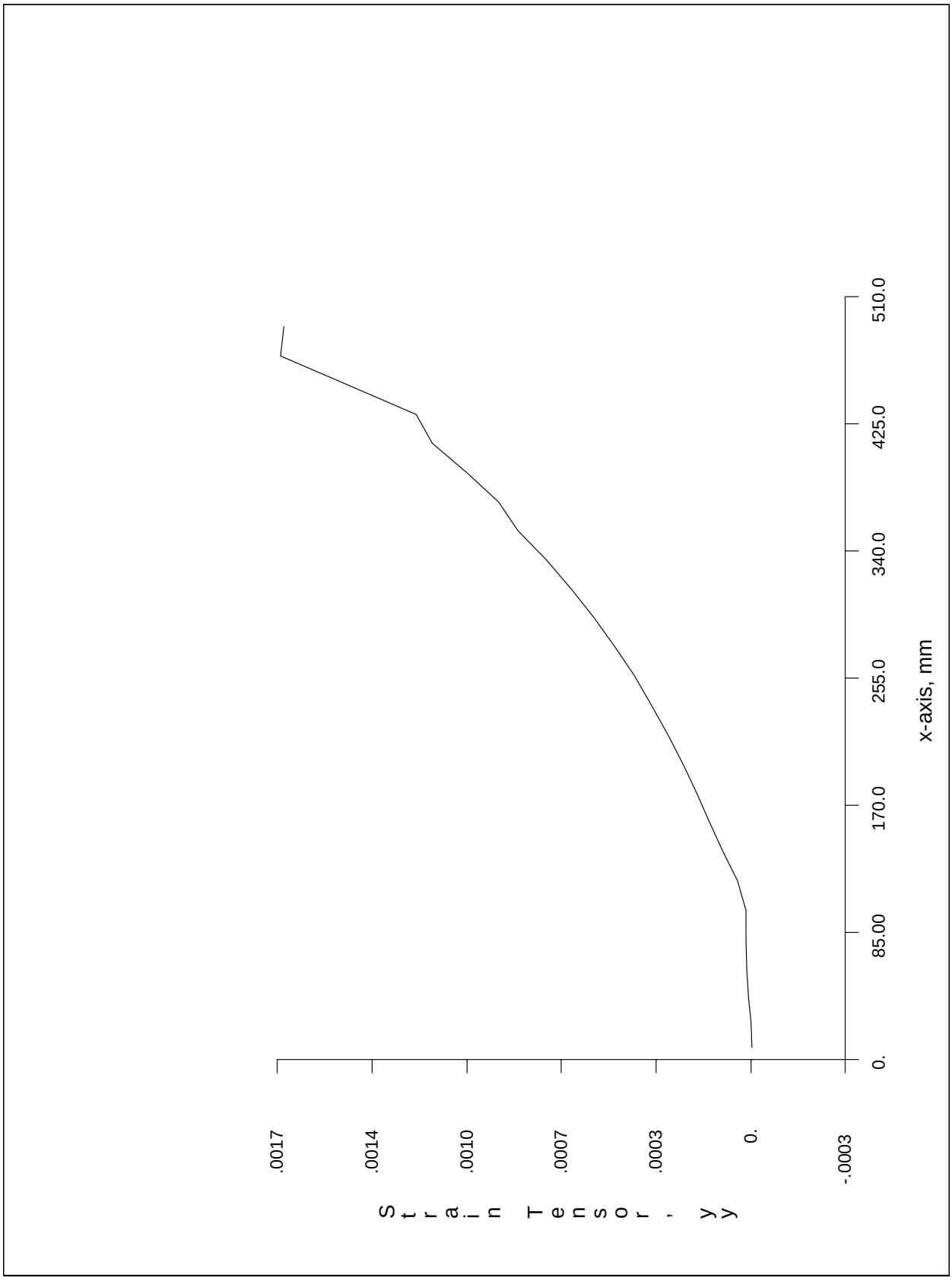

Figure D.19 Strain ε_{yy}, x-axis, 10000 N.

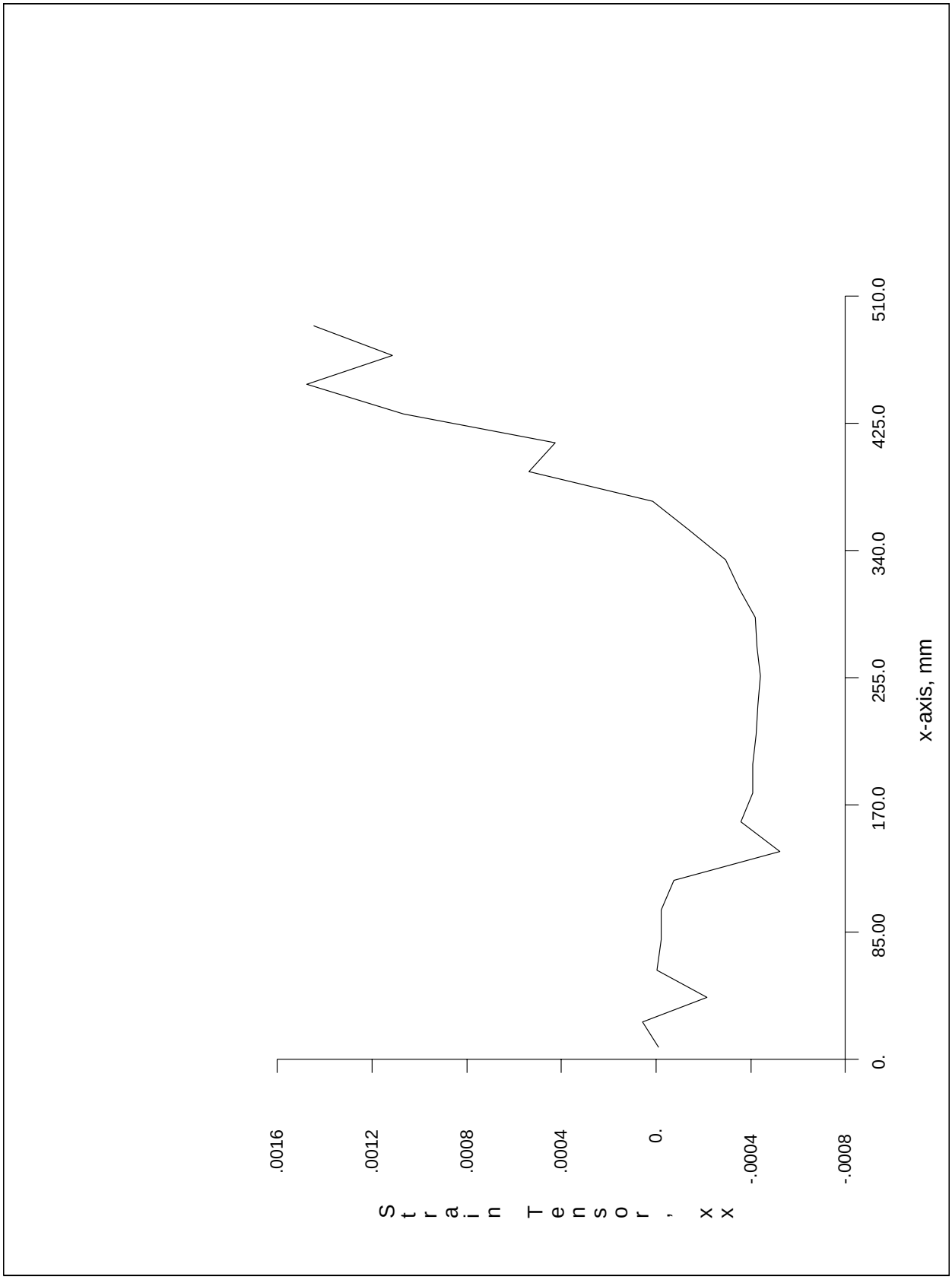

Figure D.20 Strain ε_{xx}, x-axis, 10000 N.

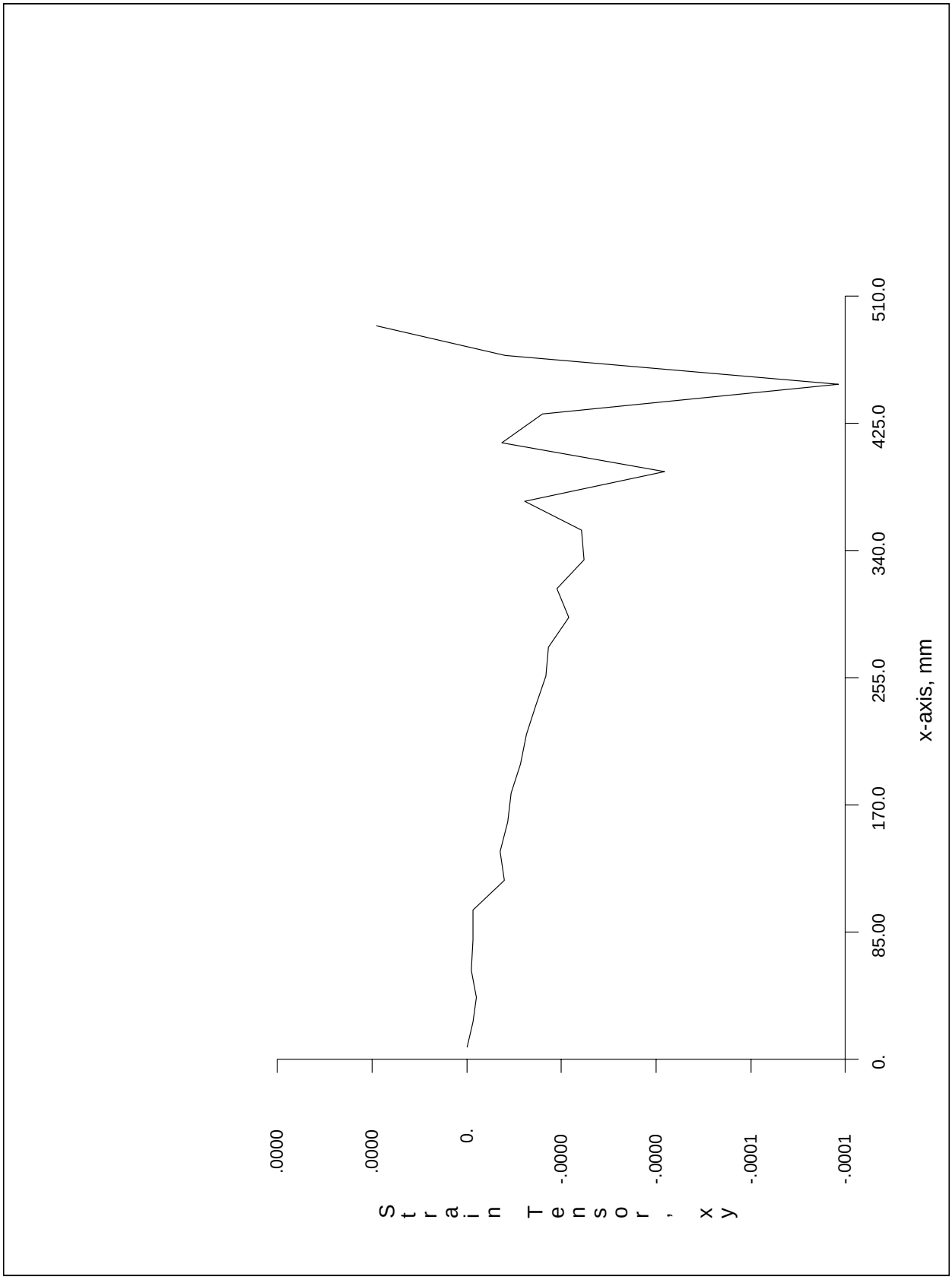

Figure D.21 Strain γ_{xy}, x-axis, 10000 N.

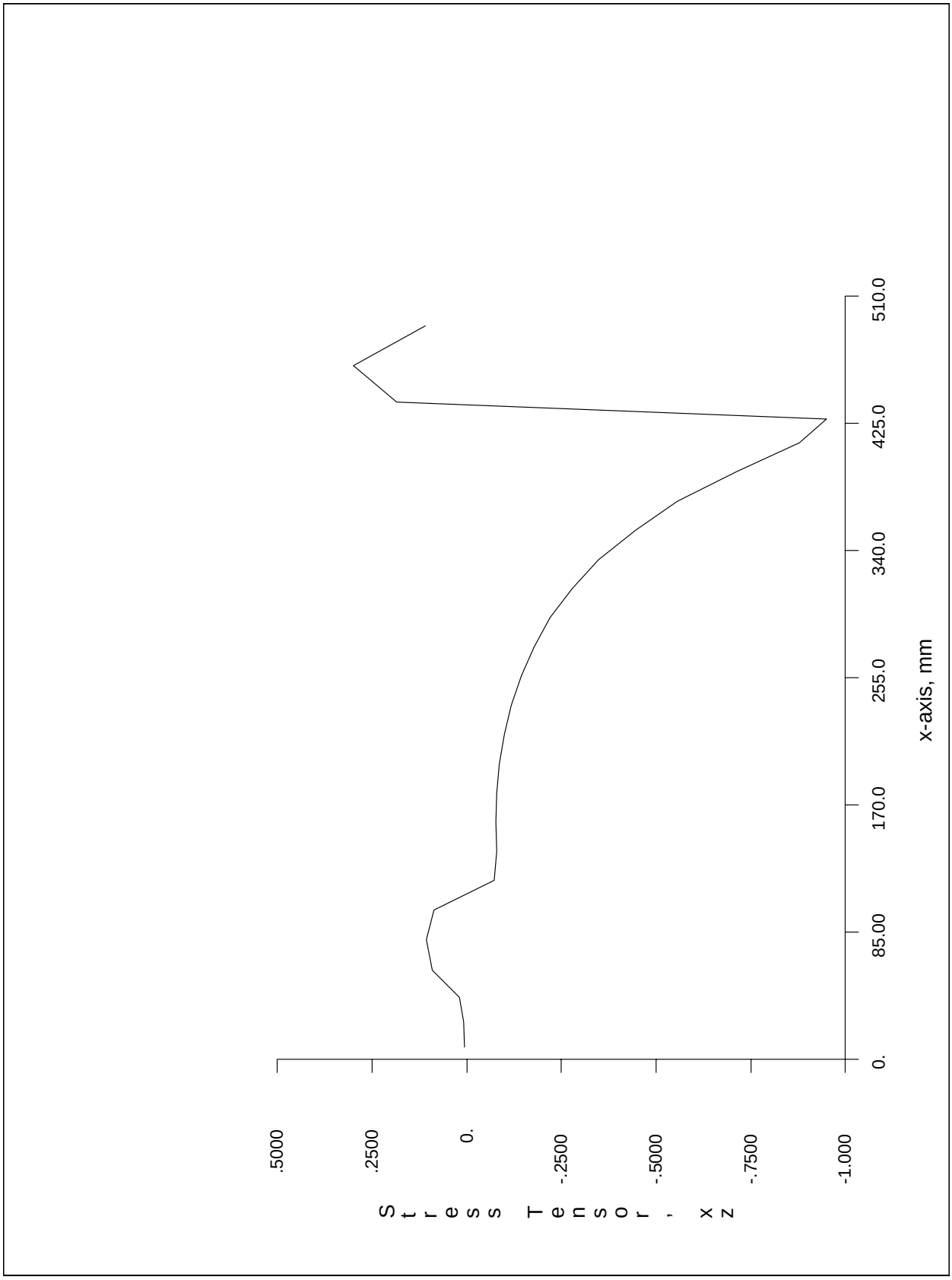

Figure D.22 Stress τ_{xz}, x-axis, 10000 N.

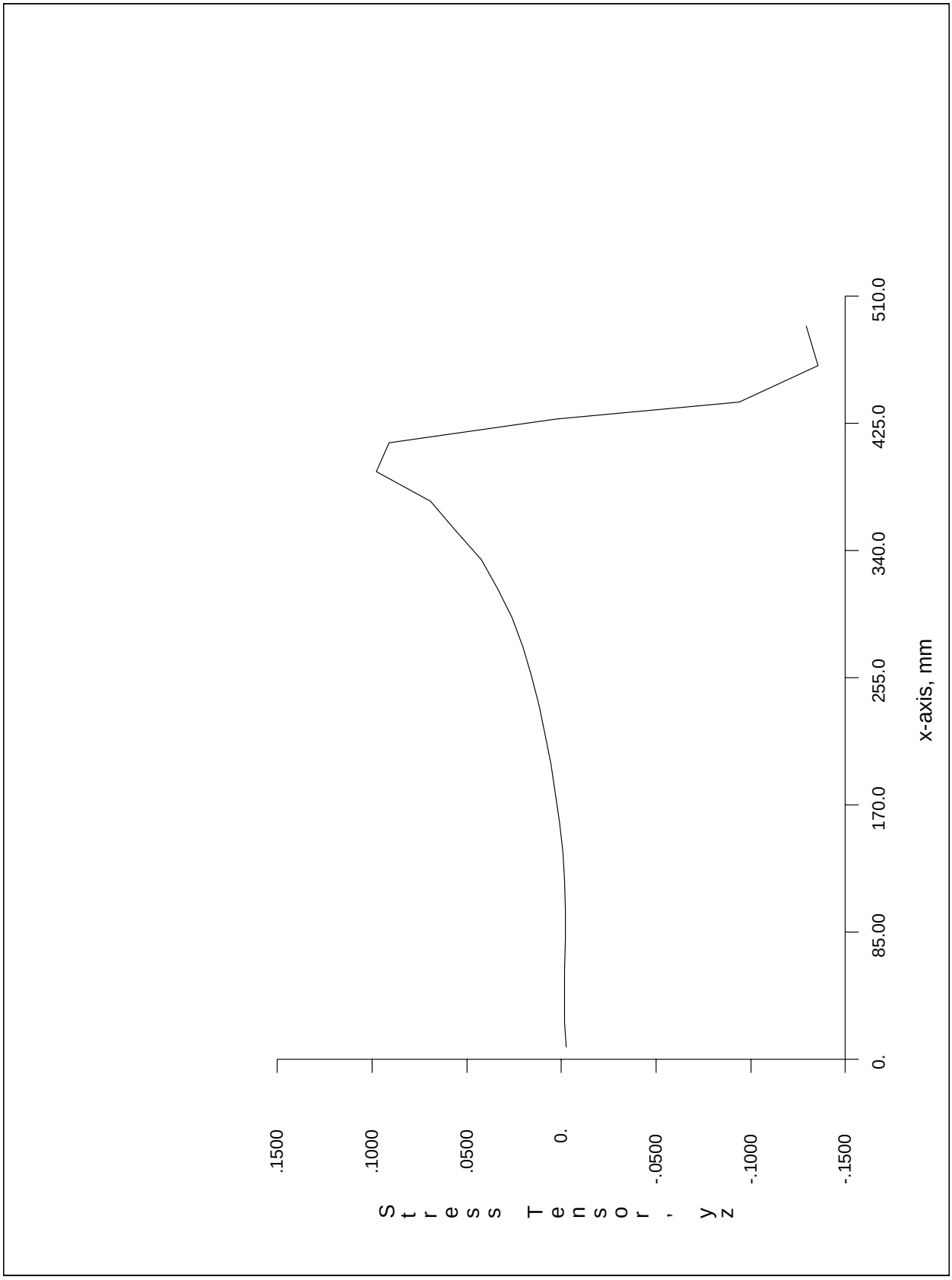

Figure D.23 Stress τ_{yz}, x-axis, 10000 N

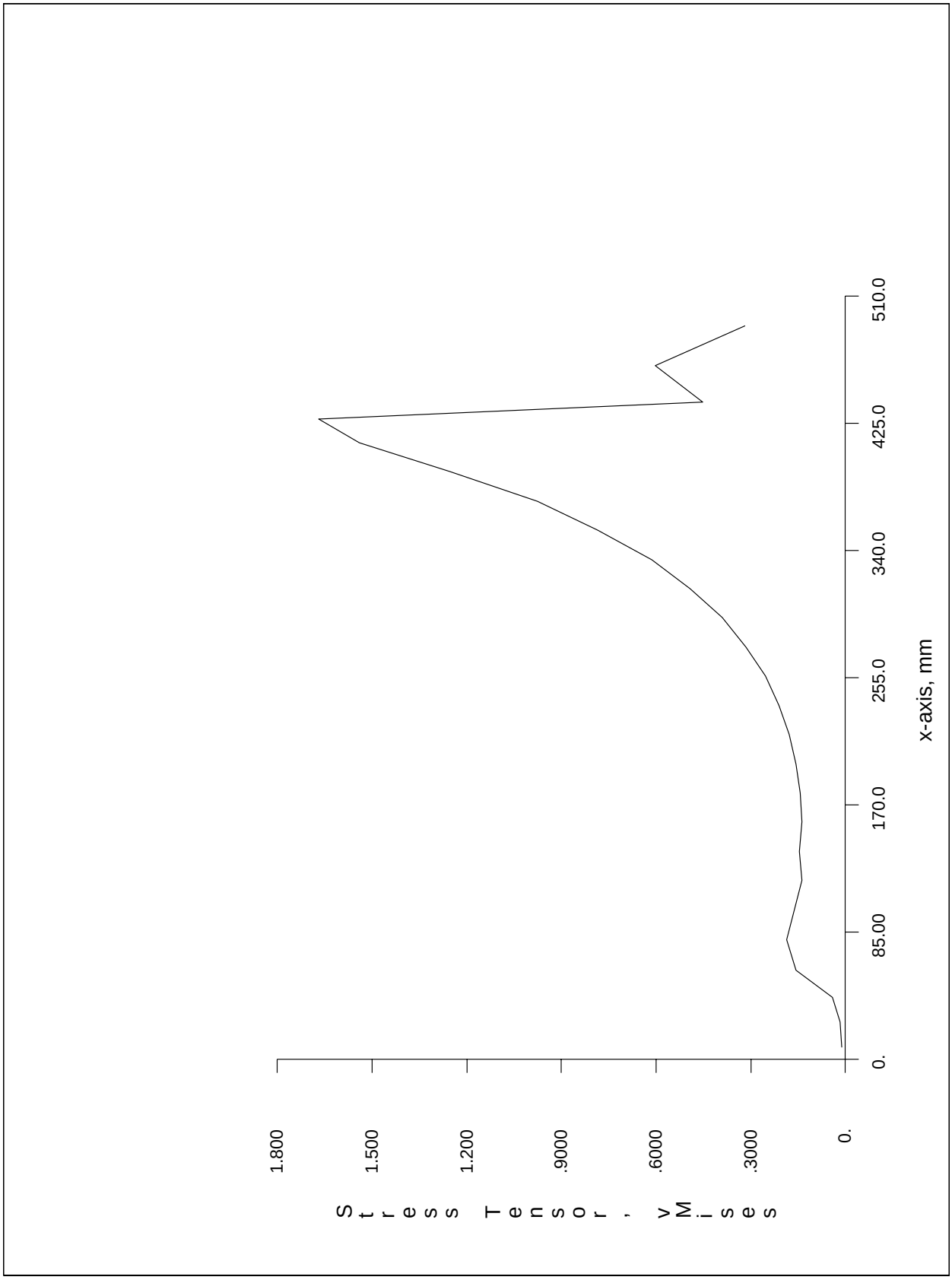

Figure D.24 Von Mises stress, x-axis, 10000 N.

DISTRIBUTION LIST

FFIE **Dato:** 18 april 2001

RAPPORTTYPE (KRYSS AV)	RAPPORT NR.	REFERANSE	RAPPORTENS DATO
X RAPP ☐ NOTAT ☐ RR	2001/02156	FFIE/793/116	18 april 2001
RAPPORTENS BESKYTTELSESGRAD		ANTALL EKS UTSTEDT	ANTALL SIDER
Unclassified		65	91
RAPPORTENS TITTEL		FORFATTER(E)	
THEORETICAL AND EXPERIMENTAL INVESTIGATION OF STRAIN GRADIENTS FOR TRANSVERSAL SHEAR STRESS DETERMINATION IN GRP SANDWICH PANELS		HAUGLAND Svein Jarle	
FORDELING GODKJENT AV FORSKNINGSSJEF:		FORDELING GODKJENT AV AVDELINGSSJEF:	

EKSTERN FORDELING

ANTALL	EKS NR	TIL
		NTNU, Fakultet for Maskinteknikk
1		Institutt for mekanikk, termo- og fluiddynamikk
1		v/ Fridtjov Irgens
		Kolbjørn Heies vei 2
		7034 TRONDHEIM
1		FiReCo a.s
1		v/ Alf Egil Jensen
1		v/ Jon Taby
		Mosseveien 39b
		1610 FREDRIKSTAD
1		Det norske Veritas
1		v/ Brian Hayman
1		v/ Ø. Lund Johansen
		Veritasveien 1
		1322 HØVIK
1		Umoe Mandal a.s
1		v/ Nere Skomedal
1		v/ Anders Hjelmseth
		Serviceboks 902
		4509 MANDAL
		Naval Research Laboratory
1		Fibre Optic Smart Structures Section
1		v/ Anthony Dandridge
1		v/ Michael D. Todd
1		v/ Gary Cogdell
		Code 5600
		4555 Overlook Ave. SW
		Washington DC 20375
		USA

INTERN FORDELING

ANTALL	EKS NR	TIL
14		FFI-Bibl
1		Adm direktør/stabssjef
1		FFIE
1		FFISYS
1		FFIBM
3		Gunnar Wang. FFIE
1		Tor Alexander Fjeldly, FFIBM
1		Jan Henning Rysjedal, FFIBM
1		Torbjørn Olsen, FFIBM
1		Øystein Farsund, FFIE
1		Karianne Pran, FFIE
1		Geir Sagvolden, FFIE
1		Lasse Vines, FFIE
3		Svein Jarle Haugland, FFIBM
6		Arkiv-FFIE
6		Arkiv-FFIBM
		FFI-veven

FFI-K1 Retningslinjer for fordeling og forsendelse er gitt i Oraklet, Bind I, Bestemmelser om publikasjoner for Forsvarets forskningsinstitutt, pkt 2 og 5. Benytt ny side om nødvendig.

EKSTERN FORDELING **INTERN FORDELING**

ANTALL	EKS NR	TIL	ANTALL	EKS NR	TIL
1		SFK, Teknisk avdeling			
1		v/ Steinar Nilsen			
1		v/ Alte Sannes			
		Postboks 3, Haakonsvern			
		5086 BERGEN			
1		MARINTEK			
1		v/ Ole Hermundstad			
		Postboks 4125			
		7450 TRONDHEIM			
1		Los Alamos National Laboratory			
1		v/ Charles R. Farrar			
		MS P946			
		Los Alamos, NM 87545			
		USA			